# PROTON RESONANCE SPECTROSCOPY IN $^{29}$P

LAWRENCE H. JAMES

*Triangle Universities Nuclear Laboratory*

*Department of Physics*

*North Carolina State University*

*1989*

**Abstract**

James, Lawrence Hoy Proton Resonance Spectroscopy in $^{29}$P (Under the direction of Gary E. Mitchell)

Proton elastic scattering on $^{28}$Si was measured with good beam energy resolution in the proton energy range $E_p$=1.4 to $E_p$=3.75 MeV, and proton inelastic scattering on $^{28}$Si was studied from $E_p$=3.0 to 3.75 MeV. A resonance not previously seen in the elastic scattering channel was observed at $E_p$=2.287 MeV; the elastic width was measured to be 80 eV. The resonance at $E_p$=3.102 MeV had been assigned $J^{\pi}=5/2^-$ from previous proton elastic and inelastic scattering data. From the present measurements the spin and parity of the resonance is $J^{\pi}=7/2^-$. The capture yields were used to locate extremely weak resonances near $E_p$=1.377 MeV and 2.630 MeV. Upper limits for the elastic widths of the resonances at $E_p$=1.377 MeV and 2.630 MeV are 2 eV; this reduced the previous upper limits for the elastic widths by 3 orders of magnitude. The resonance at $E_p$=2.630 MeV has an inelastic width of 10 eV. Spectroscopic factors for the resonances in $^{29}$P were compared with those for the levels in the parent nucleus $^{29}$Si. Large Thomas-Ehrman shifts are observed for a number of the mirror levels.

# PROTON RESONANCE SPECTROSCOPY IN $^{29}$P

by

Lawrence H. James

A thesis submitted to the Graduate Faculty of
North Carolina State University
in partial fulfillment of the
requirements for the Degree of
Doctor of Philosophy

**College of Physical and Mathematical Sciences**

Department of Physics

Raleigh

1989

**Approved By:**

_____ _____

Chairman of Advisory Committee

_____ _____

ACKNOWLEDGEMENTS

I would like to thank my research advisor, Prof. G.E. Mitchell, for his guidance and encouragement during all phases of this research project, especially during the preparation of this dissertation. I am grateful to Prof. E.G. Bilpuch for his advice and encouragement during the course of these experiments.

I would like to thank Mr. Chris Westerfeldt for his expert help in troubleshooting electronic and mechanical problems in the course of these experiments as well as many helpful discussions. I would also like to thank Dr. John Shriner, Dr. Jeff Bull, Dr. Will Brooks, and Dr. Jeff Vanhoy for their assistance and encouragement during this project.

The efforts of Stephanie Frankle, Chris Frankle, Jianying Li, Chris Coburn, and Kara Keeter are gratefully appreciated, particularly for the assistance during the data taking runs.

The assistance of Mr. Sidney Edwards, Mr. Paul Carter, and Mr. Al Lovette in maintaining the equipment and constructing new equipment. Mr Q. Shao deserves additional thanks for his assistance in the analysis of the $^{29}$P data.

I would like to thank my wife, Kay for her encouragement and belief in me during the last year of this project. I would also like to thank my step daughters Leslie and Allison for their encouragement during this time. The encouragement, help and friendship of my parents Dr. John C. James and Ann James is gratefully acknowledged as well as my brothers Mr. Clay James, Mr. Tony James and Mr. David James, and my sister Mrs Ruth Pittman.

# BIOGRAPHY

| | |
|---|---|
| Name: | Lawrence Hoy James |
| Personal: | Born March 6, 1956, Winston-Salem, North Carolina |
| Military: | Enlisted in United States Marine Corps Sept 1974 to 1978 |
| Education: | B.A. in Physics, Wake Forest University, 1982 |
| | M.S. in Physics, Wake Forest University, 1984 |
| | Ph.D. in Physics, North Carolina State University, 1989 |
| Membership: | Sigma Pi Sigma |

TABLE OF CONTENTS

LIST OF FIGURES

LIST OF TABLES

# CHAPTER I

## INTRODUCTION

Studies of nuclear resonances have provided spectroscopic information since the formulation of the compound nuclear hypothesis by Bohr [Bo36]. The High Resolution Laboratory at Triangle Universities Nuclear Laboratory has emphasized the study of compound nuclear resonances; the physical motivations have ranged from studies of reactions of astrophysical importance to statistical properties of nuclear states.

In the present study a nucleus is reexamined which had been very well studied a generation ago with the best experimental and analysis techniques available in the 1960's. The target $^{28}$Si leads to the compound nucleus $^{29}$P; comparison of the mirror nuclei $^{29}$P-$^{29}$Si (one nucleon outside the doubly semi-magic $^{28}$Si core) should be interesting and relatively simple from a shell model viewpoint. Surprisingly, the data for such detailed comparison are not available. There are a number of levels observed in one system but not the other, and the spectroscopic properties are often poorly established. Therefore the $^{28}$Si +p reactions have been reexamined both to improve the spectroscopic information and to explore whether improved energy resolution and analysis techniques have any significant impact on the spectroscopic information.

In 1959 Vorona [Vo59] and 1961 Belote [Be61] performed proton elastic and inelastic scattering experiments on $^{28}$Si. From the analysis of the resulting excitation curves spins, parities, energies, and widths were assigned to levels in $^{29}$P. In both cases a single level approximation was used to analyze the data. In the 60's and early 70's capture experiments were performed by Van Oostrum [Oo61], Ejiri [Ej63], Monohan

[Mo70], Williams [Wi70], Barnes [Ba73], Byrski [By74], and Terrasi [Te79] to study the electromagnetic decay schemes of the levels. Small resonances previously not seen by the elastic and inelastic scattering data were observed by Byrski and Ejiri. Upper limits on the proton elastic width were established. Spectroscopic information was obtained for resonances in $^{29}P$ in the 70's from $^{28}Si(\tau,d)^{29}P$ by Leleux [Le74], Peterson [Pe75], Dykoski [Dy76], and Koyama [Ko77].

In the present measurements proton elastic and inelastic scattering excitation curves were obtained from 1.4 MeV to 3.75 MeV. The data were analyzed using a multilevel analysis based on R-Matrix theory. Small resonances not observed in the elastic or inelastic excitation curves were located in the gamma-ray yields. These resonances were then studied by proton elastic and inelastic scattering with very high counting statistics. One resonance not previously seen in the elastic excitation curves was observed, and one resonance was observed in inelastic scattering which was not previously seen in the elastic or inelastic channel. Improved upper limits were set for the elastic widths of several resonances.

Chapter II gives a brief outline of R-Matrix theory. Chapter III and Chapter IV describe the equipment and experimental procedure, and the importance of energy calibration and stability. Chapter V presents the analysis and results, while Chapter VI reviews the present status of the spectroscopic information for the mirror pair $^{29}P$-$^{29}Si$.

# CHAPTER II

## SCATTERING AND R-MATRIX THEORY

### A. Notation

The scattering process may be divided into three steps; step I before the formation of the compound state--the entrance channel, II the formation of the compound system, and III the disintegration of the compound system to form two separate exiting particles--the exit channel. Only two particle processes are considered here. The process may be written schematically as a+A --> C --> B+b, where a+A is the entrance channel pair and will be denoted by $\alpha$, and B+b is the exit channel and will be denoted by a primed quantity $\alpha'$. Other labels for quantum numbers will be denoted in a similar manner, with unprimed quantities referring to the entrance channel and primed quantities to the exit channel.

### B. External Wavefunctions

R-Matrix theory as developed by Wigner and Eisenbud [Wi47] and summarized by Lane and Thomas [La58], provides a relatively model independent procedure for extraction of useful parameters from low energy experimental cross sections. The method of Lane and Thomas is described below. In R-Matrix Theory, the scattering problem is divided into an external region where only the well known Coulomb force operates and an internal region where unknown nuclear forces operate.

The equation to solve is the Schrodinger equation for the relative motion of the reaction pair, which is given by

$$HX = EX \qquad 2.1$$

The solution for X in the region where only Coulomb forces are significant is given below. X is the relative motion wavefunction, and is assumed to be in product form.

$$X = r_\alpha^{-1} u_{\alpha s \ell}(r_\alpha) \psi_{\alpha s v} i^\ell Y_m^{(\ell)}(\Omega_\alpha) \qquad 2.2$$

The differential equation governing the relative radial separation r, of the two particles is

$$\left[\frac{d^2}{dr_\alpha^{\,2}} - \frac{\ell(\ell+1)}{r_\alpha^2} - \frac{2M_\alpha}{\hbar^2}\left(V_{\alpha s \ell} - E_\alpha\right)\right] u_{\alpha s \ell}(r_\alpha) = 0. \qquad 2.3$$

The solutions to this equation are well known for the Coulomb potential, $V_{\alpha s \ell} = Z_{\alpha 1} Z_{\alpha 2} e^2 / r_\alpha^2$, and may be written in a form representing an incoming and an out-going wave; the asymptotic forms of these solutions are

$$I_c^+ \equiv I_{\alpha\ell}^+ \approx \exp\left[-i\left(\rho_\alpha - \eta_\alpha \log 2\rho_\alpha - \frac{1}{2}\ell\pi + \sigma_{\alpha,0}\right)\right]$$
$$O_c^+ \equiv O_{\alpha\ell}^+ \approx \exp\left[+i\left(\rho_\alpha - \eta_\alpha \log 2\rho_\alpha - \frac{1}{2}\ell\pi + \sigma_{\alpha,0}\right)\right] \qquad 2.4$$

These solutions may be expressed as linear combinations of the independent regular and irregular wave functions $F_{\alpha\ell}$ and $G_{\alpha\ell}$, which are tabulated and described by

Abramowitz [Ab72]. Negative energy eigenvalues of the Schrodinger Equation correspond to closed channels and are represented by a decaying wave function $O_c^-$.

$$O_c^- \equiv O_{\alpha\ell}^- \approx \exp[-(\rho_\alpha - \eta_\alpha \log 2\rho_\alpha)] \qquad 2.5$$

The complete channel wave functions including angular and spin dependence are

$$I^+_{\alpha s\ell vm} = \left(i^\ell Y_m^{(\ell)}(\Omega_\alpha)\right)\frac{I^+_{\alpha\ell}}{v_\alpha^{\frac{1}{2}} r_\alpha}\psi_{\alpha sv}$$

$$O^+_{\alpha s\ell vm} = \left(i^\ell Y_m^{(\ell)}(\Omega_\alpha)\right)\frac{O^+_{\alpha\ell}}{v_\alpha^{\frac{1}{2}} r_\alpha}\psi_{\alpha sv} \qquad 2.6$$

C. Differential Cross Section

1. Collision Matrix

The collision matrix $U_{cc'}$ represents the formation of the compound system by channel c and decay by channel c'. The total external wave function may be written as a linear combination of incoming and outgoing waves, in the form of equation 2.6, where $x_c$ and $y_c$ are appropriate expansion coefficients.

$$\Psi(\text{general}) = \sum_{cc'}(y_c I_c - x_c O_c) \qquad 2.7$$

$$x_c = U_{cc'} y_{c'}$$

The incident plane wave may also be expanded in terms of $I_c$ and $O_c$.

$$\Psi' = \sum_{cc'} \left( \delta_{cc} I_c - e^{2i\omega_c} \delta_{cc'} O_{c'} \right) y_c \qquad 2.8$$

The general wave function can be written in the form of an incident and scattered wave.

$$\Psi(\text{general}) = \Psi' + \sum_{cc'} \left( e^{2i\omega_c} \delta_{cc'} - U_{cc'} \right) O_{c'} y_c \qquad 2.9$$

The expansion coefficients $y_c$ are

$$y_c = y_{\alpha s \ell v m} = \frac{i\pi^{\frac{1}{2}}}{k_\alpha} (2\ell + 1)^{\frac{1}{2}} \qquad 2.10$$

The incident plane wave may be expanded in terms of regular Coulomb wavefunctions [Sc49]. The asymptotic form is given below.

$$\Psi'_{\alpha s v} \approx v^{-\frac{1}{2}} \psi_{\alpha s v} \left[ \left( 1 - \left( \frac{\eta_\alpha^2}{ik_\alpha (r_\alpha - z_\alpha)} \right) \right) \times \right.$$
$$\left. \exp\left[ i \left( k_\alpha z_\alpha - \eta_\alpha \log k_\alpha (r_\alpha - z_\alpha) - \sigma_{\alpha,0} \right) \right] \right. \qquad 2.11$$

$$-\frac{\pi^{\frac{1}{2}}}{r_\alpha k_\alpha} C_\alpha(\vartheta_\alpha) \exp\left[i\left(\rho_\alpha - \eta_\alpha \log 2\rho_\alpha + \sigma_{\alpha,0}\right)\right]\Bigg]$$

Where $C_\alpha(\vartheta_\alpha)$ is

$$C_\alpha(\vartheta_\alpha) = (4\pi)^{-\frac{1}{2}} \eta_\alpha \cos ec^2\left(\frac{\vartheta_\alpha}{2}\right) \exp\left\{-2i\eta_\alpha \log \sin\left(\frac{\vartheta_\alpha}{2}\right)\right\} \qquad 2.12$$

The total wave function with $O_c$ in its asymptotic form is

$$\Psi(\text{general}) \approx \Psi'_{\alpha s \nu} + i\pi^{\frac{1}{2}} \sum_{\substack{\alpha' s' \ell' \\ \ell \nu' m'}} (2\ell+1)^{\frac{1}{2}} \times$$

$$\left[e^{2i\omega_{\alpha'\ell'}} \delta_{\alpha' s' \ell' \nu' m', \alpha s \ell \nu m} - U_{\alpha' s' \ell' \nu' m', \alpha s \ell \nu m}\right] \times \qquad 2.13$$

$$\frac{1}{v_{\alpha'}^{\frac{1}{2}} r_{\alpha'}} \exp\left(i\left[\rho_{\alpha'} - \eta_{\alpha'} \log 2\rho_{\alpha'} + \sigma_{\alpha',0}\right]\right)\left(i^{\ell} Y_{m'}^{\ell'}(\Omega_{\alpha'})\right) \Psi_{\alpha' s' \nu'}$$

2. Scattering Amplitude

Equation 2.11 and 2.13 give explicitly the total external wave function. The amplitude of the radial outgoing scattered wave contains all of the information and is called the scattering amplitude. The external wave function may be written in the form

$$\Psi(\text{general}) = \Pi_{\alpha s v} + A_{\alpha s v,\alpha' s' v'}(\vartheta) \times \frac{1}{v_{\alpha'}^{\frac{1}{2}} r_{\alpha'}} \exp\left(i\left[\rho_\alpha - \eta_\alpha \log 2\rho_\alpha + \sigma_{\alpha,0}\right]\right) \qquad 2.14$$

The function $\Pi$ is the plane wave part. The equation below gives the scattering amplitude.

$$A_{\alpha' s' v',\alpha s v} = \frac{\pi}{k_\alpha}\left\{ -C_{\alpha'}(\vartheta_{\alpha'})\delta_{\alpha' s' v',\alpha s v} + i\sum_{\ell' m' \ell}(2\ell+1)^{\frac{1}{2}} \times \left[e^{2i\omega_{\alpha'\ell'}}\delta_{\alpha' s'\ell' v' m',\alpha s\ell v 0} - U_{\alpha' s\ell' v' m',\alpha s\ell v 0}\right]\right\} i^{\ell'} Y_{m'}^{(\ell')}(\Omega_{\alpha'}) \qquad 2.15$$

The differential cross section for an unpolarized incident particle on an unpolarized target is given in terms of the scattering amplitude by

$$d\sigma_{\alpha\alpha' ss} = [(2s+1)(2s'+1)]^{-1} \sum_{\alpha' v' v} \left|A_{\alpha' s' v',\alpha s v}\right|^2 d\Omega_{\alpha'} \qquad 2.16$$

To connect the cross section with physical observables a change of basis from the $\alpha s l v m$ scheme to the $\alpha s l J M$ scheme is performed. The scattering amplitude after transformation to this new basis is

$$A_{\alpha's'\nu',\alpha s\nu} = \frac{\pi}{k_\alpha}\Big[-C_\alpha(\vartheta)\delta_{\alpha's'\nu',\alpha s\nu} + i\sum_{JM\ell\,\ell'm'}(s\ell\nu 0|JM)(s'\ell'\nu'm'|JM)\times T_{\alpha's'\nu',\alpha s\nu}{}^{J}Y_{m'}^{(\ell')}(\Omega_{\alpha'})\Big] \qquad 2.17$$

Where

$$T_{\alpha's'\nu',\alpha s\nu}{}^{J} = e^{2i\omega_{\alpha'\ell'}}\delta_{\alpha's'\nu',\alpha s\nu}{}^{J} - U_{\alpha's'\nu',\alpha s\nu}{}^{J}$$

In the absolute summing procedure indicated in equation 2.16 two sets of summing integers are introduced. The equation below gives the absolute square in terms of sums of Clebsch-Gordan coefficients.

$$\left|A_{\alpha's'\nu',\alpha s\nu}\right|^2 = \Bigg\{\frac{\pi^{\frac{1}{2}}}{k_\alpha}\Big[-C_\alpha(\vartheta_\alpha)\delta_{\alpha's'\nu',\alpha s\nu} + i\sum_{J_1M_1\ell_1'\ell_1m_1'}(2\ell+1)^{\frac{1}{2}}(s_1\ell_1\nu_1 0|J_1M_1)$$

$$\times(s_1'\ell_1'\nu_1'm_1'|J_1M_1)T_{\alpha s_1'\ell_1',\alpha s_1\ell_1}{}^{J_1}Y_{m_1'}^{(\ell_1')}(\Omega_{\alpha'})\Big] \qquad 2.18$$

$$\times\frac{\pi^{\frac{1}{2}}}{k_\alpha}\Big[-C_\alpha(\vartheta_\alpha)\delta_{\alpha's'\nu',\alpha s\nu} + i\sum_{J_2M_2\ell_2'\ell_2m_2'}(2\ell+1)^{\frac{1}{2}}(s_2\ell_2\nu_2 0|J_2M_2)$$

$$\times(s_2'\ell_2'\nu_2'm_2'|J_2M_2)T_{\alpha s_2'\ell_2',\alpha s_2\ell_2}{}^{J_2}Y_{m_2'}^{(\ell_2')}(\Omega_{\alpha'})\Big]\Bigg\}$$

The sums over the magnetic quantum states may be eliminated and the equation written

in terms of the Z-bar coefficients of Biedenharn [Bi52] with the phase convention of Huby [Hu54] and is given below in equation 2.19. The $P_\ell(\cos\vartheta)$ are Legendre polynomials with the phase convention of Condon and Shortley [Co51] and Condon and Obabasi [Co80]. The total differential cross section as used in the analysis program MULTI6 is given below in equation 2.19. An explicit form of the collision matrix will be given after the internal wavefunctions have been connected to the external wave functions.

$$d\sigma_{\alpha s,\alpha' s'} = \left|C_\alpha(\vartheta_\alpha)\right|^2 \delta_{\alpha' s',\alpha s} + \frac{(2s+1)^{-1}}{k_\alpha^{\,2}} \sum_L B_L(\alpha' s', \alpha s) P_L(\cos\vartheta_{\alpha'})$$

$$+ (4\pi)^{\frac{1}{2}} \pi \frac{(2s+1)^{-1}}{k_\alpha} \sum_{J\ell} (2J+1) 2\,\mathrm{Re}\left[ iT_{\alpha' s' \ell', \alpha s \ell}{}^{J} C_{\alpha'}(\vartheta_{\alpha'}) P_\ell(\cos\vartheta_{\alpha'}) \right] \qquad 2.19$$

$$B_L = \frac{1}{4}(-)^{s-s'} \sum_{J_1 J_2 \ell_1 \ell_2 \ell_1' \ell_2'} \bar{Z}(\ell_1 J_1 \ell_2 J_2, sL)\, \bar{Z}(\ell_1' J_1 \ell_2' J_2, sL)$$

$$\times \left( T_{\alpha' s' \ell_1', \alpha s \ell_1}^{J_1} \right) \left( T_{\alpha' s' \ell_2', \alpha s \ell_2}^{J_2} \right)^* \qquad 2.20$$

D. Internal Wave Function

The wave function in the internal region satisfies a Schrodinger equation with $\Psi$ the total wave function and $X_\lambda$ a complete set of states which represent the resonanes. Both wave functions satisfy the same Schrodinger equation Vo[62].

$$H\Psi = E\Psi \qquad 2.21a$$

$$HX_\lambda = E_\lambda X_\lambda \qquad 2.21b$$

The total wave function may be expanded in terms of the states $X_\lambda$; these states are assumed complete and satisfy the conditions below.

$$\Psi = \sum_\lambda A_\lambda X_\lambda \qquad 2.22$$

$$\int_\tau X_{\lambda'} X_\lambda^* \, d\tau = \delta_{\lambda\lambda'} \qquad A_\lambda = \int_\tau X_\lambda^* \Psi \, d\tau$$

Multiplying equation 2.21a by $X_\lambda^*$, multiplying the complex conjugate of equation 2.21b by $\Psi$, and subtracting 2.21a from 2.21b gives

$$(E_\lambda - E)\int_\tau X_\lambda^* \Psi \, d\tau = \int_\tau \left[ X_\lambda^* H\Psi - \Psi (HX_\lambda)^* \right] d\tau \qquad 2.23$$

The potentials are assumed self-adjoint; the volume integral on the right hand side is reduced to a surface integral by using Green's theorem.

$$(E_\lambda - E)\int_\tau X_\lambda^* \Psi \, d\tau = \left( \frac{\hbar^2}{2M_c} \right) \int_s \left[ X_\lambda^* \, \mathrm{grad}_n \Psi - \Psi \, \mathrm{grad}_n X_\lambda^* \right] ds \qquad 2.24$$

The right hand side of equation 2.24 is integrated by parts. Several useful quantities are defined in equation 2.25 a, b, c, and d.

$$V_{\lambda c} = \left(\frac{\hbar^2}{2M_c}\right)^{\frac{1}{2}} X_\lambda \Big|_s \qquad 2.25\,a$$

$$D_{\lambda c} = \left(\frac{\hbar^2}{2M_c}\right)^{\frac{1}{2}} \text{grad}_n X_\lambda \Big|_s \qquad 2.25\,b$$

$$V_c = \left(\frac{\hbar^2}{2M_c}\right)^{\frac{1}{2}} \Psi \Big|_s \qquad 2.25\,c$$

$$D_c = \left(\frac{\hbar^2}{2M_c}\right)^{\frac{1}{2}} \text{grad}_n \Psi \Big|_s \qquad 2.25\,d$$

Equation 2.24 takes the simple form below after substitution.

$$(E_\lambda - E) A_\lambda = \sum_c \left( V_{\lambda c}{}^* D_c - V_c D_{\lambda c}{}^* \right) \qquad 2.26$$

The boundary condition for equation 2.26 is given by

$$\frac{D_{\lambda c}}{V_{\lambda c}} = \left(\frac{\delta_{\lambda c}}{\gamma_{\lambda c}}\right) = B_c \qquad 2.27$$

Therefore equation 2.26 may be rewritten

$$(E_\lambda - E) A_\lambda = \sum_c \gamma_{\lambda c} (D_c - B_c V_c) \qquad 2.28$$

The quantity $\gamma_{\lambda c}$ is called the reduced width amplitude. Substituting for $A_\lambda$ yields the total wave function

$$\Psi = \sum_c \left( \sum_\lambda \frac{\gamma_{\lambda c} X_\lambda}{(E_\lambda - E)} \right) D_c^0 \qquad ; D_c^0 = D_c - B_c V_c \qquad 2.29$$

This equation relates the value of $\Psi$ at any point r to its derivatives $D_c^0$ on the surface S. Integrating over the surface wavefunctions gives the fundamental R-Matrix relation

$$V_{c'} = \sum_c R_{cc'} D_c^0$$

$$R_{cc'} = \sum_\lambda \frac{\gamma_{\lambda c} \gamma_{\lambda c'}}{(E_\lambda - E)} \qquad 2.30$$

Now it remains to connect the R-Matrix with the collision matrix at the surface and to write the collision matrix in terms of the R-Matrix.

E. Connection of R-Matrix and Collision Matrix

Using the R-Matrix relation equation 2.30 and 2.7 for the external wave function 2.30 and defining $\rho_c = ka_c$, gives

$$\left( \frac{\hbar^2}{2M_c a_c} \right)^{\frac{1}{2}} \left( v_c^{-\frac{1}{2}} O_c x_c + v_c^{-\frac{1}{2}} I_c y_c \right) =$$

$$= \sum_{c'} R_{cc} \left[ \left( \frac{\hbar^2}{2M_c a_c} \right)^{\frac{1}{2}} \rho_c \left( v_c^{-\frac{1}{2}} O_c x_c + v_c^{-\frac{1}{2}} I_c y_c \right) + \right. \qquad 2.31$$

$$\left. B_c \left( \frac{\hbar^2}{2M_c a_c} \right)^{\frac{1}{2}} \left( v_c^{-\frac{1}{2}} O_c x_c + v_c^{-\frac{1}{2}} I_c y_c \right) \right]$$

The relation between $x_c$ and $y_c$ is given in equation 2.7. The collision matrix may now be expressed in terms of the R-Matrix in matrix notation.

$$\left(\rho^{-\frac{1}{2}}\mathbf{I}+\rho^{-\frac{1}{2}}\mathbf{UO}\right)=\mathbf{R}\left[\left(\rho^{\frac{1}{2}}\mathbf{UO'}+\rho^{\frac{1}{2}}\mathbf{I'}\right)-\mathbf{B}\left(\rho^{-\frac{1}{2}}\mathbf{UO}+\rho^{-\frac{1}{2}}\mathbf{I}\right)\right] \qquad 2.32$$

After algebraic manipulation of equation 2.32 a solution is obtained for the collision matrix U in terms of the R-Matrix.

$$\mathbf{U}=\frac{\mathbf{I}}{\mathbf{O}}\rho^{-\frac{1}{2}}\left(1-\mathbf{R}\left(\rho\frac{\mathbf{O'}}{\mathbf{O}}-\mathbf{B}\right)\right)\left(1+\mathbf{R}\left(\rho\frac{\mathbf{I'}}{\mathbf{I}}-\mathbf{B}\right)\right)^{-1}\rho^{-\frac{1}{2}} \qquad 2.33$$

It is convenient to redefine combinations of **I**, **O**, and ρ.

$$\Omega_\ell=e^{i\phi_\ell}=\left(\frac{I_\ell}{O_\ell}\right)^{\frac{1}{2}}_{r=a_c} \qquad 2.34a$$

$$L_\ell=\left(\rho\frac{O'_\ell}{O_\ell}\right)_{r=a_c}=S_\ell(\rho)+iP_\ell(\rho) \qquad 2.34b$$

$S_\ell(\rho)$ is called the shift function and $P_\ell(\rho)$ is the penetrability. The latter factor contains the kinematical factors which relate the total laboratory width to the reduced width. With these definitions equation 2.34 takes the form given below.

$$\mathbf{U}=\Omega\mathbf{P}^{\frac{1}{2}}[1-\mathbf{R}(\mathbf{L}-\mathbf{B})]^{-1}[1-\mathbf{R}(\mathbf{L}^*-\mathbf{B})]\mathbf{P}^{\frac{1}{2}}\Omega \qquad 2.35$$

The matrices Ω, **P**, **L**, and **B** are all diagonal. A more explicit form for the collision matrix is

$$U_{cc'} = e^{2i(\omega-\phi)}\left[1 - \frac{2iP\gamma^2}{E_\lambda - E - \gamma^2(S-B) - iP\gamma^2}\right] \qquad 2.36$$

By defining the laboratory width $\Gamma=2P\gamma^2$, and the energy shift $\Delta_\lambda \equiv \gamma^2(S-B)$, the expression takes the form of the well known Breit-Wigner formula

$$U_{cc'} = e^{2i(\omega-\phi)}\left[1 - \frac{2iP\gamma^2}{(E_\lambda - E - \Delta_\lambda) + \frac{i\Gamma}{2}}\right] \qquad 2.37$$

The general expression for the collision matrix does not contain any explicit reference to the form of the nuclear potential. Quantities dealing with the nuclear interior have been written in terms of the value and derivative of the wave function at the boundary. These quantities are expressed in terms of the exterior Coulomb functions at the surface. Information about the nuclear potential is contained in the intermediate state energies $E_\lambda$, the reduced width amplitudes $\gamma_{\lambda c}$, the boundary condition $B_c$, and the matching radius $a_c$.

# CHAPTER III

# EXPERIMENTAL EQUIPMENT AND PROCEDURES

## A. High Resolution Laboratory and Control Systems

The experiments performed in this study used a High Voltage Engineering Corporation Van de Graaff accelerator. With the corona feedback and the homogenizer circuitry in operation this accelerator is capable of an overall resolution of 300 to 400 eV with thin solid targets (approximately 1 $\mu g/cm^2$). This system provides high resolution beams from $E_p$=0.7 MeV to 4.1 MeV.

The RF ion source [We87] produces two species of hydrogen beams, $H^+$ and $HH^+$. These two beams are bent through angles of 25 degrees and 17 degrees by the analyzing magnet, as shown in figure 3.1. The $H^+$ beam is used to perform the experiment, while the $HH^+$ beam is a control beam.

A current difference is measured by the corona slits in front of the electrostatic analyzer when the beam passes through the slits. This difference signal is applied to the corona control to increase or decrease the terminal voltage as necessary by increasing or reducing the charge. The drift time for charge carriers from the terminal to the corona needles limits the frequency that voltage corrections may be applied to the terminal. The drift time for this system is about 50 ms and allows for the correction of signals on the terminal less than or equal to 20 Hz.

The analyzer plates are biased at equal and opposite potentials, producing zero potential halfway between the plates. The geometrical properties of the plates govern the

Figure 3.1 High Resolution Laboratory and Control Systems.

# High Resolution Laboratory and Control Systems

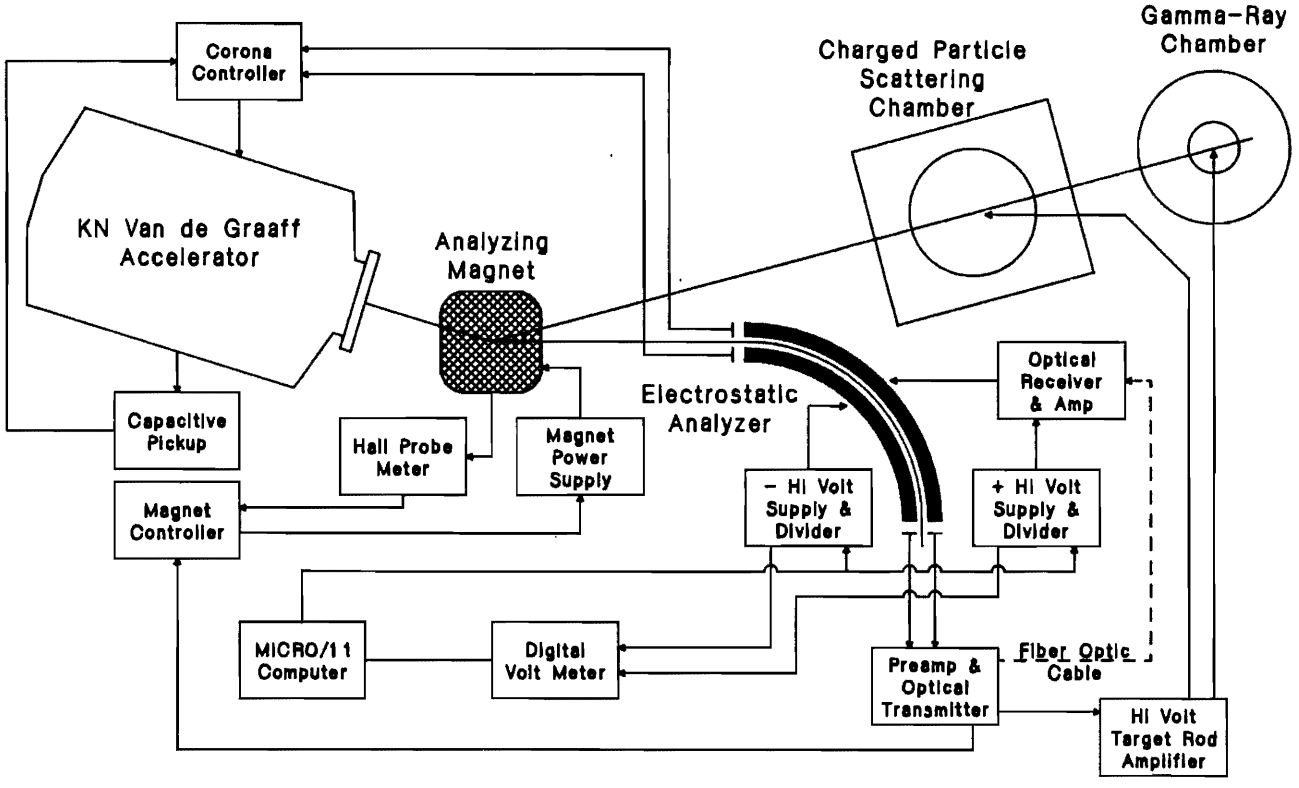

transport of the beam through the analyzer system [To54]. The necessary condition for this transport is given by

$$VT = eV_A 2 \ln\left(\frac{R_1}{R_2}\right)\left[\frac{\frac{eV_A}{2mc^2}+1}{\frac{eV_A}{mc^2}+1}\right] \qquad 3.1$$

Here VT is the total voltage between the plates, $R_1$ and $R_2$ are the outer and inner radii of the analyzing plates, $V_A$ is the terminal voltage and m is the relativistic mass of $HH^+$. For this analyzer the potential between the two plates is equal to the energy of the $HH^+$ beam divided by 111.37. A Fluke digital voltmeter (DVM) is set up to display the voltage between the plates. A voltage divider system is used; the division ratio of each of the voltage dividers is adjusted by precision decade dividers to 1/8979. At this ratio the voltage displayed by the DVM is equal to the terminal voltage on the accelerator.

Once the beam is transported through the electrostatic analyzer, a difference signal is measured on the exit slits. This difference signal is used for fast corrections to the beam energy by applying the amplified signal directly to the target rod. This signal is also used to keep the beam in the electrostatic analyzer, as well as stabilizing the analyzing magnet. The difference signal is amplified by the homogenizer circuitry [Wa86], which is an open loop gain circuit for the target rod; the gain for this circuit must be adjusted periodically. The correction signals fluctuate around a 3 kV bias on the target rod. The energy of the $HH^+$ beam transported through the analyzer is 3 keV higher than the $H^+$ beam transported to the target. The Fluke digital voltmeter used in

measuring the $HH^+$ beam supplies an offset of -3 kV to the actual DVM reading to compensate for this difference.

A correction signal cannot be applied directly to the outer plate, since the plate is biased at a high potential. A fiber optic link transmits the slit difference signal to the outer plate electronics used to keep the beam centered in the analyzing plates. The gain of the slit difference signal is set just below the oscillation point in order to insure a strong response. The transmitter is at ground potential and the receiver is floated to the potential of the outer plate. Power for the outer plate electronics is supplied by an isolation transformer.

A PDP/11 microcomputer automatically steps the electrostatic analyzer plate voltage by sending an analog signal to the Bertan model 205A-20P/N power supplies. The Fluke digital voltmeter and the PDP/11 communicate by RS-232 serial port interfaces. The DVM may be programmed by the microcomputer. When the plate voltage is changed, the path of the beam through the analyzer is changed, causing a difference signal on the exit slits. This difference signal changes the analyzing magnet and the corona slit difference signal which adjusts the terminal voltage by the corona feedback system. Although the exit slits measure fast signals, the signals sent to the analyzing magnet must be filtered to allow only slow changes in the analyzing magnet. It is the interplay of the corona slits, exit slits, and analyzing magnet which adjusts the voltage at the terminal to achieve the final equilibrium energy.

B. Charged Particle Scattering Chamber

The charged particle scattering chamber is shown in figure 3.2. The chamber has a diffusion pump, refrigerated baffle and liquid nitrogen trap to maintain a vacuum of $10^{-6}$ torr during experiments. Collimators ranging from 1/16" to 1/8" are housed in front of the scattering chamber, with the last collimator extending to about 4.5 inches from the center of the chamber. There are usually three collimators in the housing during an experimental run. The collimation housing is constructed so that it may be easily removed and the collimators changed when the elastic chamber is open. The collimators reduce scattering from the target rod and other objects. Since the beam is well defined after the collimation a quantitative determination of the solid angle subtended by the detectors is possible.

The total charge is collected in a Faraday cup behind the chamber. This Faraday cup may be removed from the beam line pneumatically to allow beam to the rear chamber. In front of the Faraday cup is a quartz crystal with which the beam profile may be observed. This Faraday cup is 1.5" long by 1" diameter nickel plated copper with a tantalum lining and is water cooled. A secondary electron suppressor biased at 90 volts is in front of the Faraday cup.

Five 300 micron charged particle detectors obtained from EG&G Ortec and Paul Downey & Co. were used in this experiment. Protons from the $(p,p_0)$ and $(p,p_1)$ reaction were detected. The detectors were positioned at 90, 108, 135, 150, and 165 degrees. The solid angles of the five surface barrier detectors were adjusted such that the number of counts due to Rutherford scattering was approximately the same at all angles. This guarantees that the count rate from any one detector does not overwhelm that from the other detectors. The detectors subtend a region approximately 1.2 mm in diameter at the target.

Figure 3.2 Top View of the Charged Particle Scattering Chamber.

# Charged Particle Scattering Chamber

(Top View)

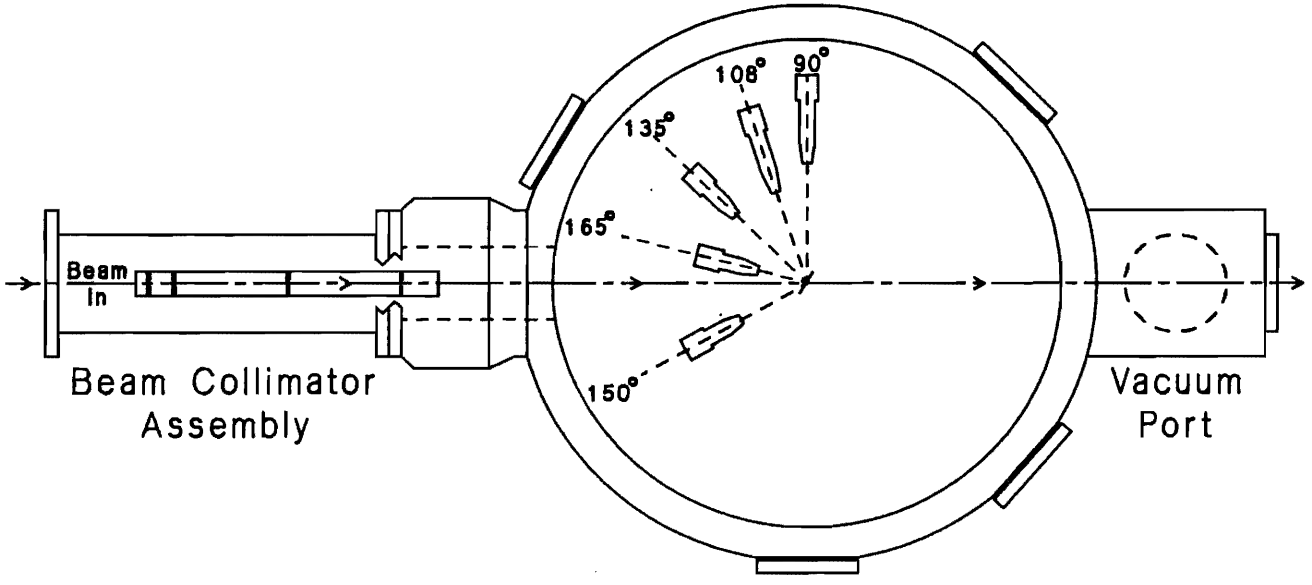

C. Gamma-Ray Chamber

The rear chamber shown in figure 3.3 is used primarily for gamma-ray detection. A diffusion pump, refrigerated baffle and liquid nitrogen trap are used to maintain a vacuum of about $10^{-6}$ torr. A water-cooled collimation assembly precedes the target chamber and is used to maintain a good beam spot on the target of about 1-2 mm in diameter. Behind the target is a water-cooled Faraday cup and suppressor system which collects the total charge.

Harshaw Chemical Co. Model 12SHA12/2-X NaI(Tl) detectors are used to detect the gamma rays. The detectors are 3 inches in length by 3 inches in diameter and are hermetically sealed units which include a photomultiplier tube. Extensive lead shielding is used to reduce gamma-ray background. A charged particle detector is placed at 135 degrees to monitor the elastic scattering and to allow for coincidence experiments.

This system can measure the charged particle cross sections as well as the gamma-ray excitation functions. Three NaI detectors at 90, 30, and 55 degrees were used in this experiment. The primary purpose of the gamma-ray yield curves was to detect resonances which were extremely weak in the elastic channel. The gamma-ray excitation function is an extremely sensitive tool for detecting weak resonances since the yield from background gamma rays is small. The solid angles of the detectors were set equal.

D. Data Acquisition for Charged Particles

As shown in figure 3.4 a pulse from a charged particle detector is first amplified

Figure 3.3 Top View of the Gamma-Ray Chamber.

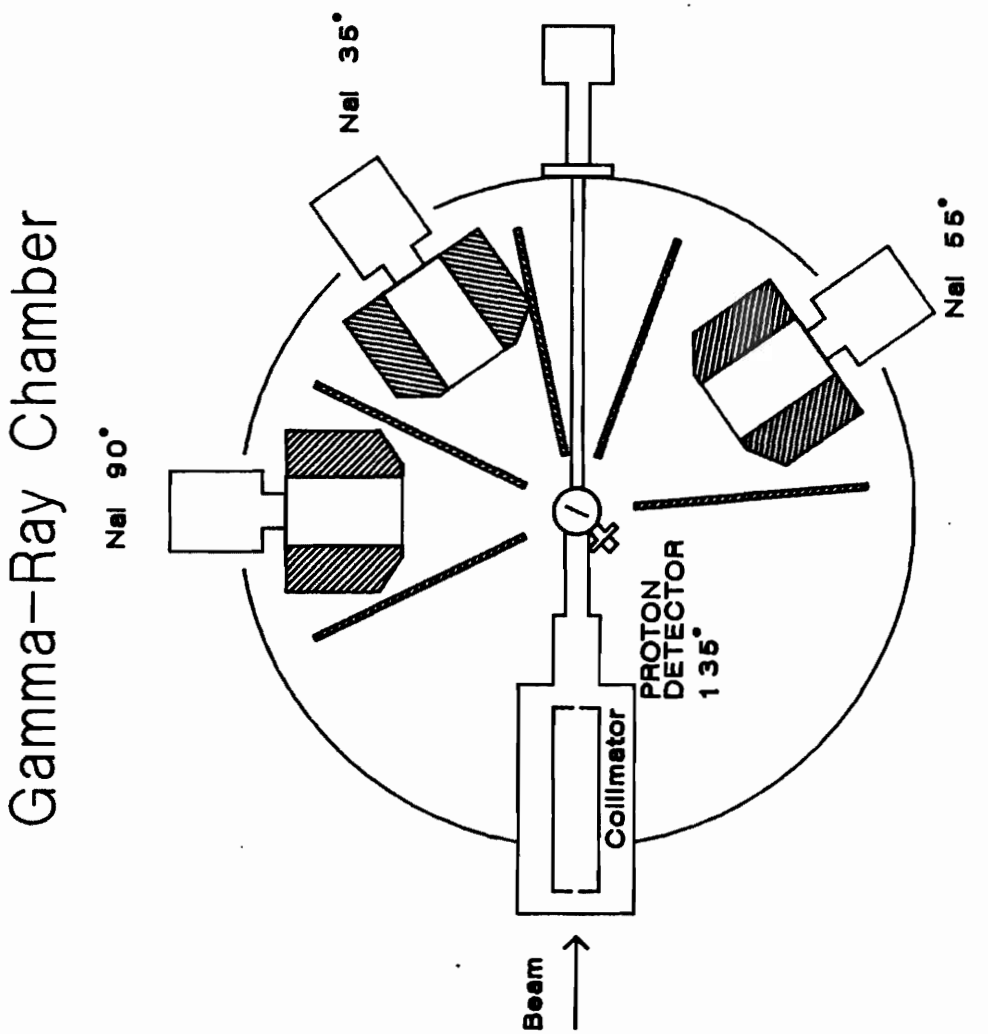
Gamma-Ray Chamber
NaI 90°
NaI 35°
NaI 55°
PROTON
DETECTOR
135°
Collimator
Beam

Figure 3.4 Data Acquisition Electronics. The same electronic set up is used for charged particle and gamma-ray detection.

## Data Acquisition Electronics Setup

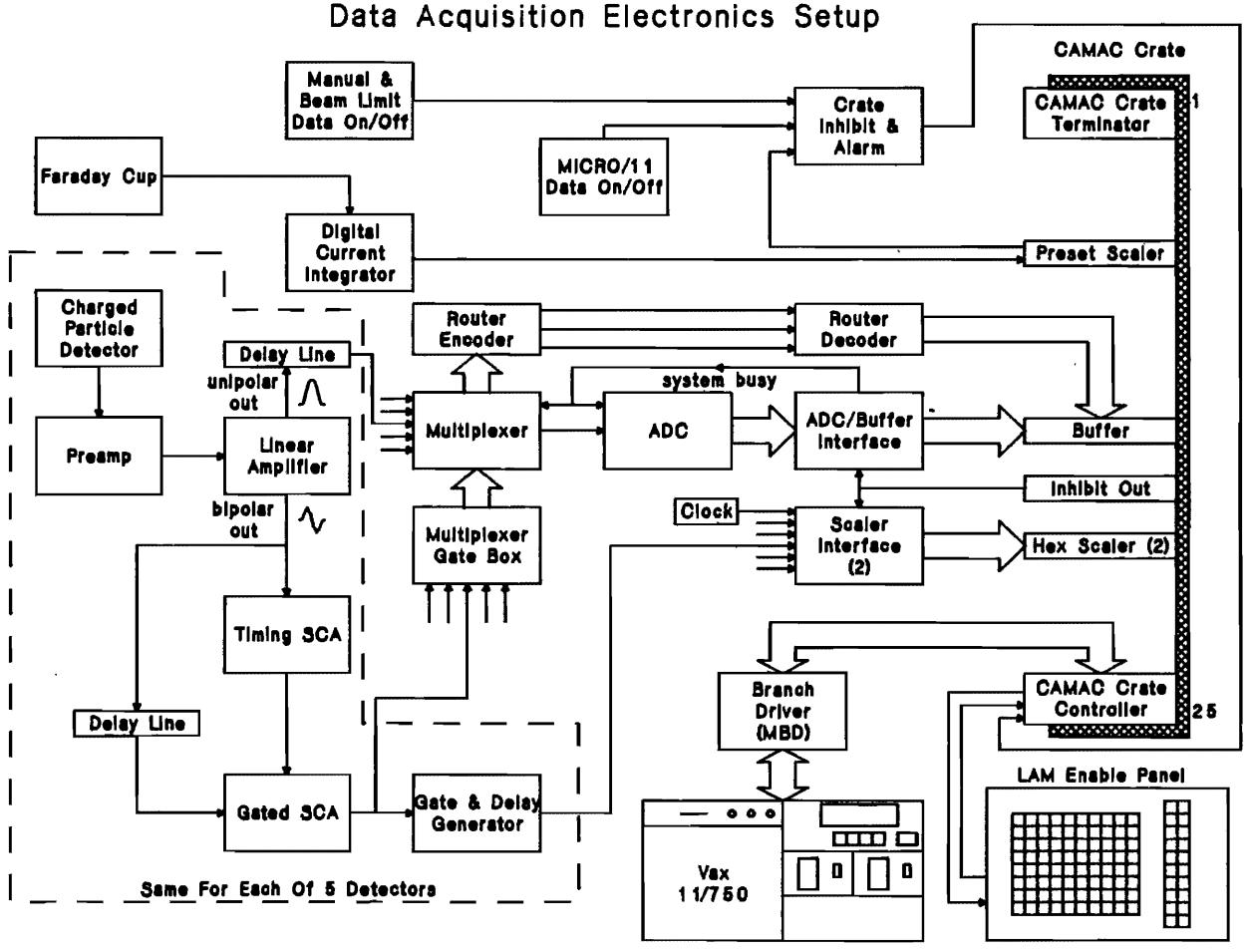

by an Ortec model 142A preamplifier. This pulse is sent to an Ortec model 572 spectroscopy amplifier where it is amplified and shaped. The gain of the amplifier is usually set so that the largest output signal amplitude is approximately 8.5 volts. Two signals are supplied from the amplifier, a unipolar and a bipolar pulse approximately 1.4 μs in width, both proportional to the energy deposited in the detector. The unipolar signal is digitized and stored (or rejected), while the bipolar signal is used to determine whether the signal is stored or not. A Tektronix oscilloscope is used to monitor the signals sent to the ADC from the multiplexer.

An Ortec model 551 timing single channel analyzer (TSCA) is used to discriminate the amplitude of a bipolar signal for gating purposes. An electronic window may be set on a certain amplitude range which corresponds to a specific energy range of the scattered particle. If the bipolar signal amplitude is in that specific amplitude range, then the output of the TSCA is a variable delay positive 5V, 500 ns wide digital pulse. In addition to the pulse from the TSCA, the bipolar signal is routed around the TSCA through a 900 ns delay line.

The bipolar signal from the delay line is input into a Hewlett Packard 5583A single channel analyzer (HPSCA). The output from the TSCA is input to the gate of the HPSCA. The HPSCA has discriminator ranges for a minimum signal amplitude of 0.05V and maximum of 10.05V. With no input from the TSCA to the gate of the HPSCA a 5V, 100 ns wide output from the single channel output of the HPSCA is triggered on the input of the bipolar signal. If the TSCA outputs a logic signal to the gate the logic signal from the HPSCA is inhibited.

The logic output of the HPSCA is routed to two different inputs. One input is an Ortec model 415A gate and delay generator whose output is a variable width 5 volt

logic pulse and is sent to a Kinitec Systems model 3610 hex scaler. This scaler counts the number of pulses actually sent to the Northern analog to digital converter (NADC). The digital signal from the HPSCA is also sent to a multiplexer gate (local design). This gate requires a signal from the HPSCA in order to inform the Ortec model 476-8 multiplexer to transmit the unipolar pulse to be digitized. With this signal the multiplexer also sends 3 bits which indicate from which detector the signal orginated. Both the digitized signal (bits 5-16) and the router bits (bits 1-3) which identify the angle are stored in a buffer in the CAMAC crate.

Signals from the preamplifier which are too close together to be distinguished cause the spectroscopy amplifier to output a pulse larger than normal. The amplifier provides a pile up rejection pulse, which may be used to gate the multiplexer and inhibit the passing of a signal to the NADC. Another signal is input at the multiplexer from the NADC to indicate that the NADC is busy digitizing a signal when another signal is sent to it. This input must be rejected while the NADC finishes digitizing the last signal. This signal is counted by the scaler. The number of counts recorded by the scaler will be greater than or equal to the total number of counts that have been digitized. The dead time is the ratio of the difference between the scaler count and the total number digitized to the scaler count. A typical dead time is 5 to 10 percent.

It is important that the total beam striking the target be monitored. The total charge striking the target is collected by a Faraday cup and secondary electron suppressor system. The current produced by beam collection is monitored by an Ortec Model 439 digital current integrator. This integrator can be set to output a number of digital pulses corresponding to the amount of charge collected. These output signals are sent to a Borer type 1008 preset scaler. The preset scaler will interrupt the data taking

when the correct number of pulses have been received.

The NADC accepts analog signals up to 8.5 volts in amplitude. The amplitude of the incoming signal is then converted to a digital number; the resolution of a typical spectrum for elastic scattering is 512 channels. The spectrum consists of the number of counts in each channel after a specific amount of charge has been deposited in the Faraday cup. An example of the spectrum obtained from proton scattering from the target is shown in figure 3.5. The three important peaks are labeled in this figure: the peak with the lowest channel number is inelastic proton scattering from the nuclide of interest $^{28}$Si, the second peak is elastic scattering from $^{16}$O, and the third is elastic scattering of protons from $^{28}$Si. A window may be set on any or all of the peaks shown in the figure. In pratice a window is set on the $^{28}$Si(p,p) and the $^{28}$Si(p,p')$^{28}$Si$^{*}$ peaks. After a predetermined amount of charge is deposited in the Faraday cup, the total number of counts under that peak is summed. This sum forms one point of a yield curve. The energy is changed and the process repeated to obtain additional points as a function of proton bombarding energy.

Data processing for both protons and gamma rays is accomplished by CAMAC interfacing and Microprogrammed Branch Driver (MBD). The data are stored in the computer with the procedure supported by the XSYS software package. XSYS is a data acquisition and analysis system for VAX computers created at TUNL. Overviews of XSYS are given by Gould [Go85]. The data flow and linkage between CAMAC and computer are shown in figure 3.4.

## E. Data Acquisition for Gamma Rays

Figure 3.5 Typical $^{28}$Si Spectrum. The gate is set on the peak corresponding to $^{28}$Si(p,p).

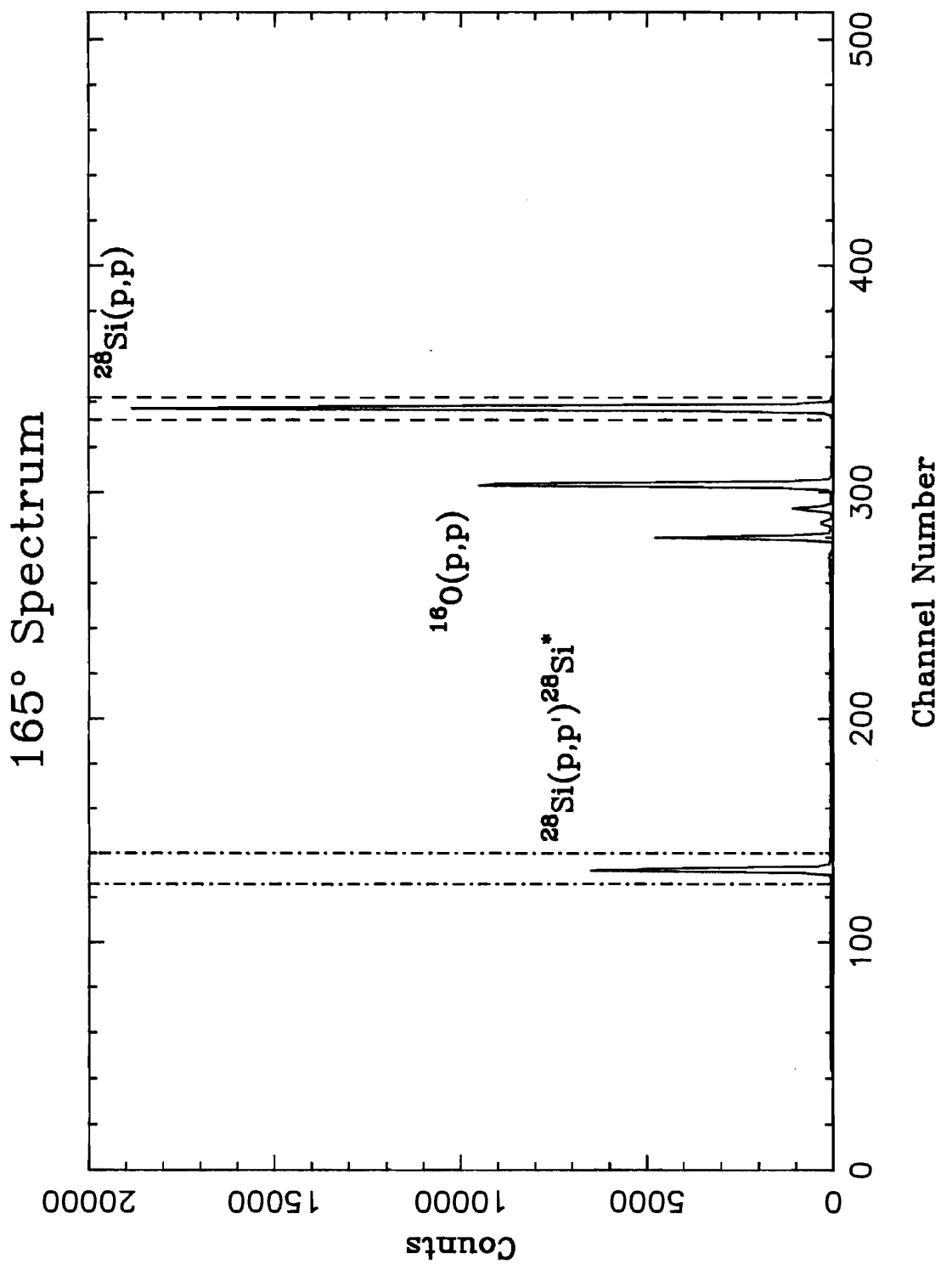
165° Spectrum
$^{28}$Si(p,p)
$^{16}$O(p,p)
$^{28}$Si(p,p')$^{28}$Si*
Counts
0
5000
10000
15000
20000
Channel Number
0
100
200
300
400
500

NaI detectors are used to detect gamma rays from the decay of the target nuclei. Each gamma-ray detector consists of a NaI crystal and photomultiplier tube hermetically sealed. The photomultiplier tube is biased at +1300 volts and connected to a Ortec Model 113 scintillation preamplifier.

A gamma ray entering the crystal causes a light pulse which is amplified by the photomultiplier. The pulse from the tube then goes to the Model 113 scintillation preamplifier. After the preamplifier the pulse is amplified by an Ortec Model 572 spectroscopy amplifier. The electronics from this point on duplicates that of the charged particle detection except in one aspect. The Ortec Model 551 timing single channel analyzer is not used. No part of the spectrum is gated.

Typical spectra for gamma rays on and off resonances are shown in figure 3.6 for $^{28}$Si. The same number of channels (512) as for the charged particle spectrum proved convenient. Windows are set to sum the number of counts in the entire spectrum. In this example the windows are set to cover an energy range of 1.00 MeV to 6.00 MeV. This range includes all capture gamma rays from $^{29}$P for an incident proton energy up to 3.25 MeV.

F. Target Preparation

Samples of silicon isotopically enriched to 98.6% $^{28}$Si were obtained from Oak Ridge National Laboratory in the form of $SiO_2$. An evaporation procedure was used to prepare the targets. Glass slides with 5 to 10 $\mu g/cm^2$ of carbon evaporated onto a salt layer were cut into 12 to 14 sections. The slides were slowly immersed in distilled water to allow the cut sections to float on the surface of the water. Each section was lifted out

Figure 3.6 Typical Gamma-Ray Spectra. The gates are set to sum over a particular energy range.

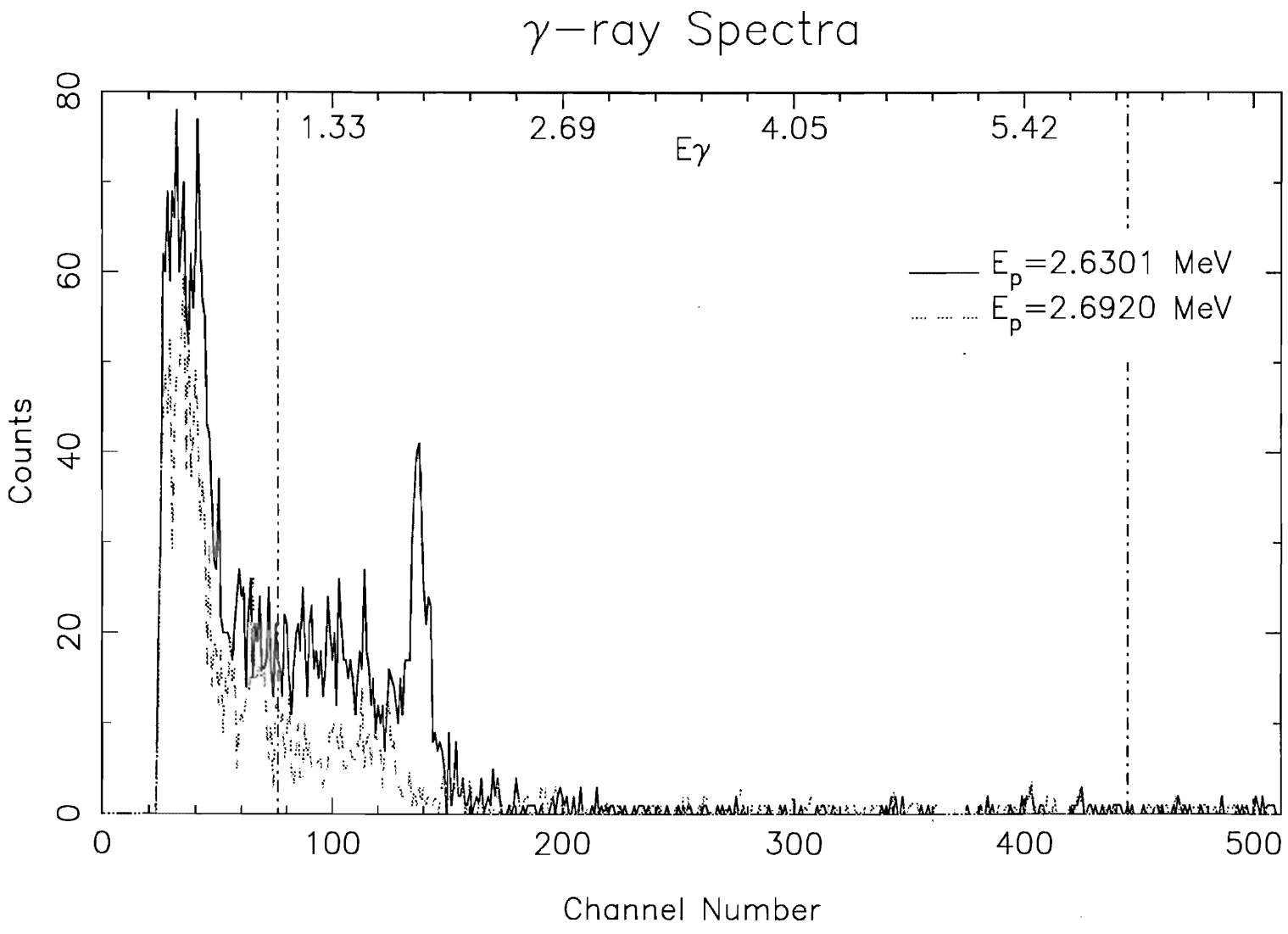
γ−ray Spectra
1.33
2.69
Eγ
4.05
5.42
E_p=2.6301 MeV
E_p=2.6920 MeV
Counts
0
20
40
60
80
0
100
200
300
400
500
Channel Number

of the water by a target ring. The target rings with the carbon backing were placed into a evaporation chamber.

$^{28}SiO_2$ was deposited in a tantalum closed boat with tantalum powder placed in the boat to serve as a reducing agent. The tantalum boat was placed in a high current source which could supply a maximum of 500 A. Two types of tantalum boats were used, with wall thicknesses of .005 in. and .010 in. The boat with the thinner wall thickness warped under the heat and deformed the opening, which may have caused some nonuniformity in the target. The boat with the .010 in. wall remained intact. The target thickness was determined by a Maxtek,Inc. Model TM-100R thickness monitor. This monitor used a crystal oscillator; as material is deposited on the crystal the frequency of oscillation changes. The thickness could be calculated by knowing the density of the material, the acoustic impedance and the change in frequency. The thickness monitor was usually accurate within 50%.

Although preparing targets of $^{28}Si$ was not difficult, obtaining the very uniform targets needed for the gamma-ray measurement was difficult. Deformities in the boat opening may have caused target nonuniformity, as well as factors such as speed of evaporation and the geometrical arrangement of the targets in the evaporator.

# CHAPTER IV

# CALIBRATION AND STABILITY

## A. Stability Measurements

The experiments performed in this study required a search for extremely weak resonances. Once the resonances were found in the gamma-ray yield curves it was necessary to measure the elastic scattering with extremely high counting statistics. A large number of counts is needed to determine or to set lower limits on the weak elastic resonance widths. This required large amounts of beam time when using thin targets and also required extremely good stability. The measurements are accomplished using thick target gamma-ray yields over the resonance region.

$^{27}$Al was chosen as the target for the stability measurements because of two convenient resonances with large strengths in the gamma-ray channel, one at $E_p$=998 keV and the other at $E_p$=2.045 MeV [Me75]. $^{27}$Al is also an abundant and easy material from which to manufacture targets. First a layer of NaCl is evaporated onto a microscope slide and then aluminum is evaporated onto the salt. Typical thicknesses were 50 to 100 $\mu g/cm^2$. Since the salt is water soluble the aluminum foils may be floated onto target rings.

The resonances at 998 keV and 2.045 MeV are easily located and appear as large increases in the gamma-ray yield. The resonance yield is taken in 50 eV steps to obtain a good thick target yield curve. Figure 4.1 shows a typical thick target yield curve for

Figure 4.1 Typical Thick Target Yield Curve for $^{27}Al(p,\gamma)^{28}Si$. The cross marks the energy at which the stability tests are performed; the region where the yield increases approximately linearly is also shown.

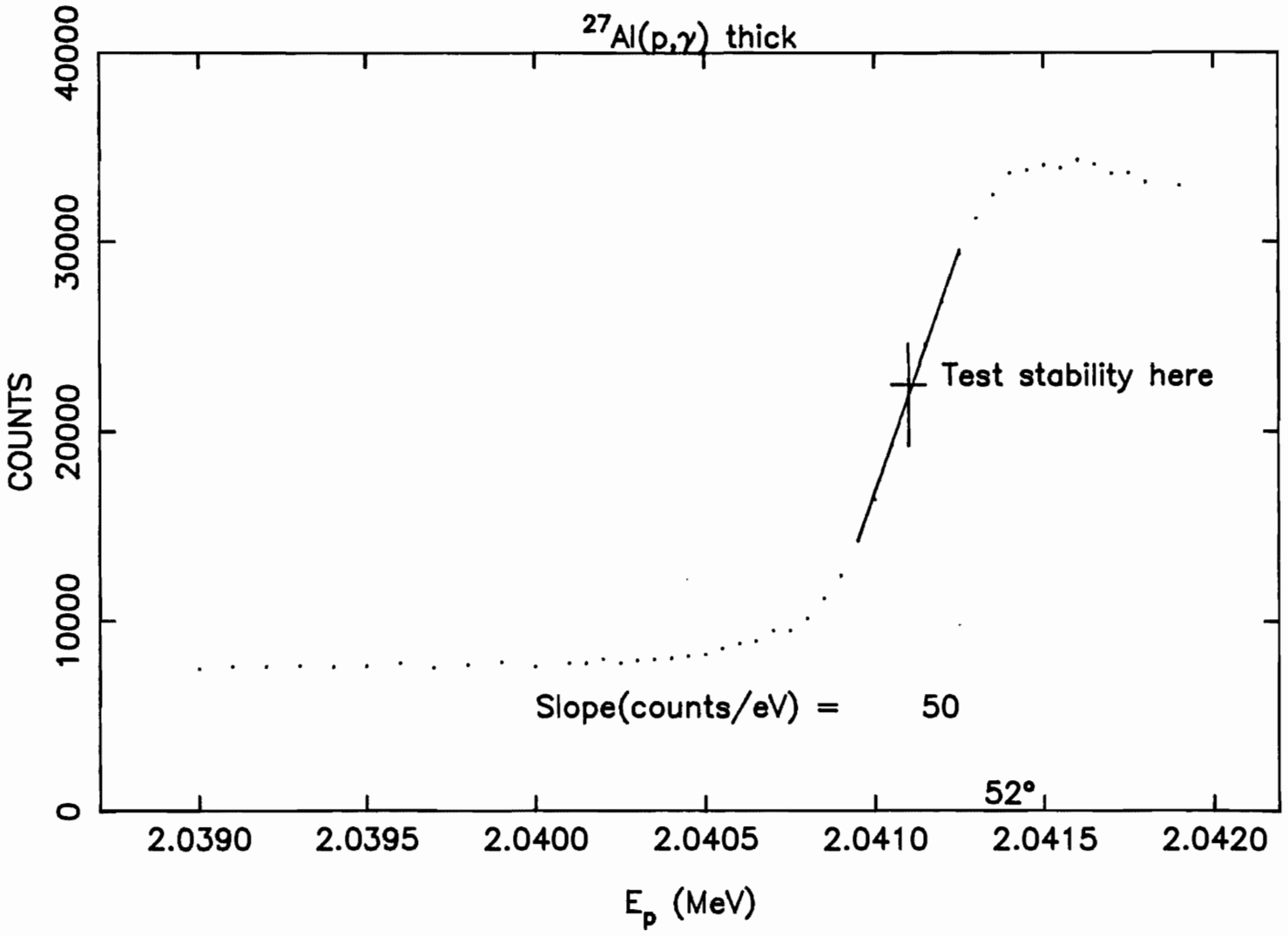
$^{27}$Al(p,γ) thick
COUNTS
0
10000
20000
30000
40000
Test stability here
Slope(counts/eV) = 50
52°
2.0390
2.0395
2.0400
2.0405
2.0410
2.0415
2.0420
$E_p$ (MeV)

$^{27}Al(p,\gamma)$ at $E_p$=2.045 MeV. The (p,p) cross section for $^{27}Al$ was measured thoroughly by Nelson et al. [Ne83]

The energy at which stability tests are performed is chosen as the midpoint between the yield below resonance and the yield above resonance: this is marked by a cross in figure 4.1. The yield at this energy is the most sensitive to any change in the energy. The yield is collected for approximately 1 to 3 hours; this length of time allows for observation of long term drift, which is usually visible to the eye.

B. Stability Analysis

After the data are measured the analysis proceeds through the following steps: first the rate of change of counts with energy is determined, second the results from the first phase are used to determine any long term drift, third the results from the first and second phases are used to determine the short term fluctuations.

A least squares analysis is used to find the best straight line through the linear portion of the yield curve in the resonance region, as shown in figure 4.1. This determines how fast the yield changes as a function of energy. The linear portion was taken ±300 eV away from the energy of the yield midpoint on the yield curve. From this least square analysis a slope is determined in counts per unit energy.

The long term drift is examined by performing a linear least squares fit to the yield versus time data, as shown in figure 4.2. The slope from this fit is in counts per unit time; this slope is multiplied by the inverse of the slope determined in the first part to obtain the energy shift per unit time.

The long term drift is affected by several factors. Tuning is crucial to the stability

Figure 4.2 Linear Least Squares Fit to the Yield vs Time Curve.

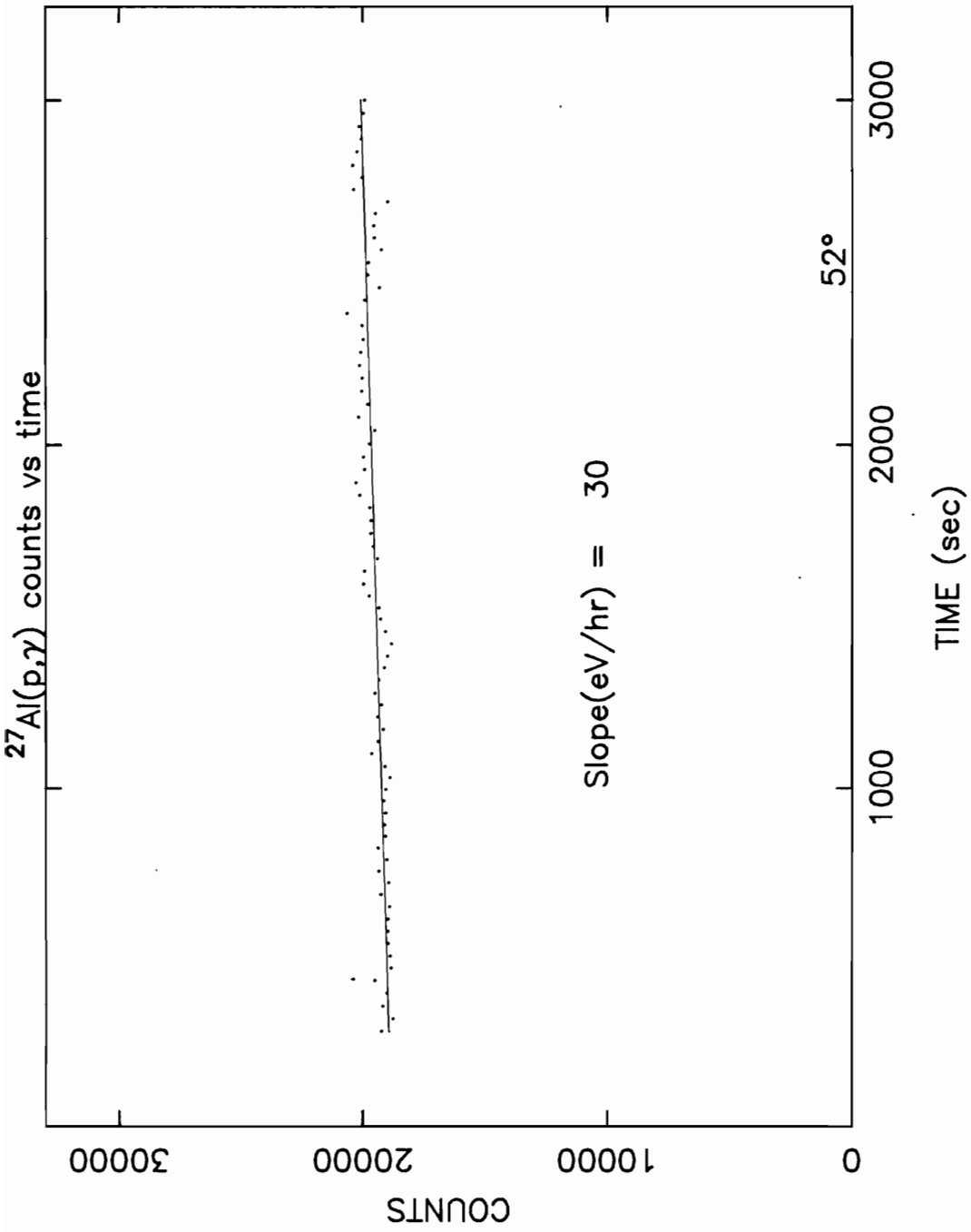
$^{27}$Al(p,γ) counts vs time
Slope(eV/hr) = 30
52°
COUNTS
TIME (sec)
0
1000
2000
3000
1000
2000
3000

of the accelerator; a poorly tuned accelerator will show large energy drifts in a short amount of time. Other causes may include, but are not limited to, dirty power supplies, failing electronic components, or a detuned homogenizer system.

Once the analysis of the long term drift is completed, then the short term fluctuations may be studied by plotting a frequency histogram of the magnitude of the fluctuations about the average yield given by the linear fit. This gives a reasonably accurate picture of the short term fluctuations. As shown in figure 4.3 these fluctuations are usually small, with a typical standard deviation $\sigma$ of approximately 5 to 7 eV.

## C. Calibration Measurements

It is important to determine the precision of the absolute energy; the precision may be examined by using reactions whose energetics are well known. Two neutron threshold reactions are used for this purpose. For the lower end of the accelerator energies it is convenient to use the $^{7}Li(p,n)^{7}Be$ reaction; sample data are shown in figure 4.4. The threshold of this reaction has been measured by several independent investigators using absolute methods; a list of results is compiled by Marion [Ma66]. The compilation gives the weighted average for the threshold as 1.8806 MeV. At higher energies it is convenient to use the $^{13}C(p,n)^{13}N$ reaction. This threshold has also been measured by several independent investigators; the weighted mean for the threshold energy is given by Marion as 3.2357 MeV.

Thick targets were used for the neutron threshold measurements. The material was evaporated onto thin (approximately .01 in.) tantalum backings. Evaporation of lithium proved simple. However, the carbon evaporation required the use of an electron gun

Figure 4.3 Histogram of Short Term Energy Fluctuations from the Linear Fit of the Yield vs Time Data.

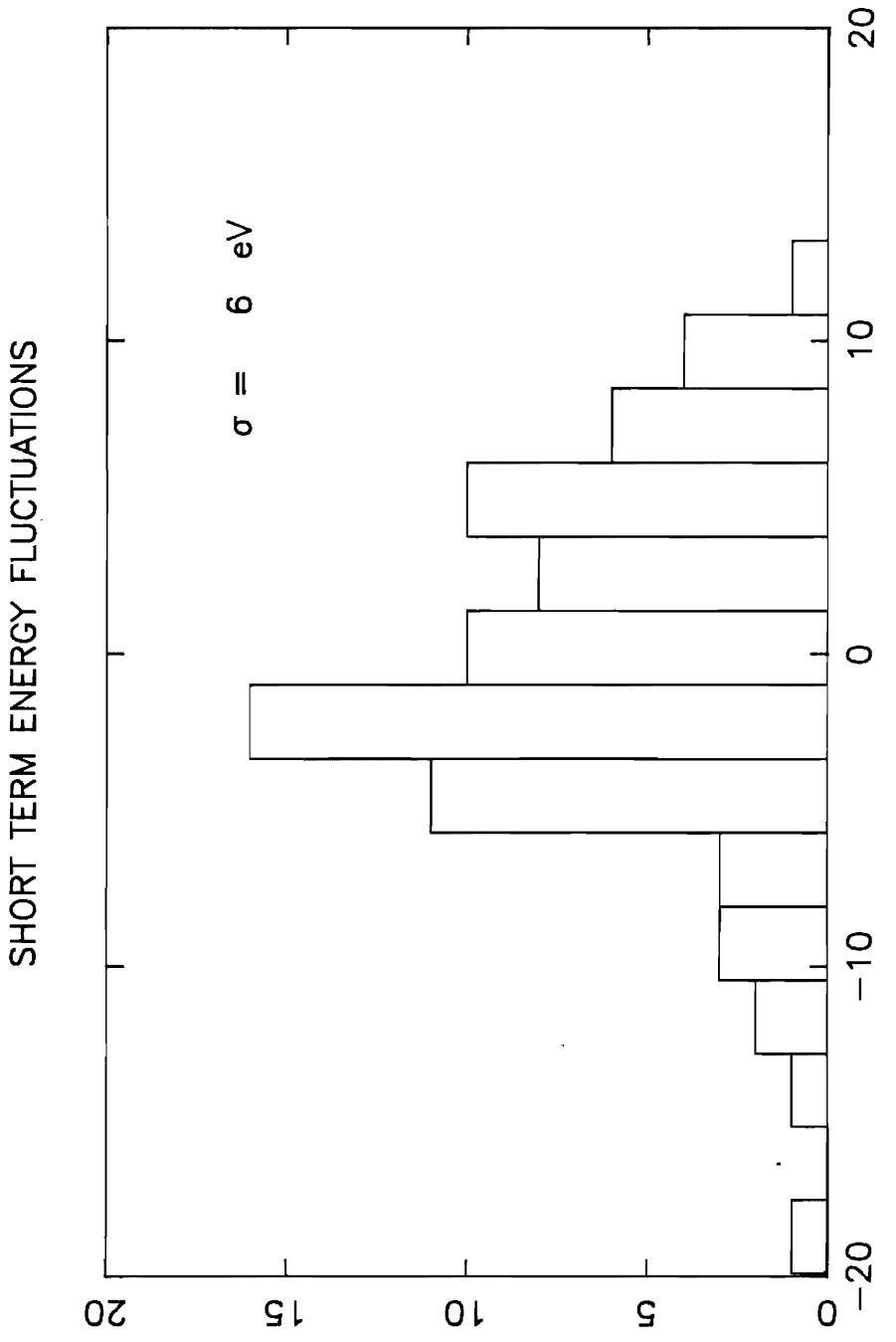
SHORT TERM ENERGY FLUCTUATIONS
σ = 6 eV
0
5
10
15
20
−20
−10
0
10
20
$E_{exp} - E_{cal}$

Figure 4.4 Fit to the $^{7}$Li(p,n) Neutron Threshold. The background and the threshold region are analyzed separately.

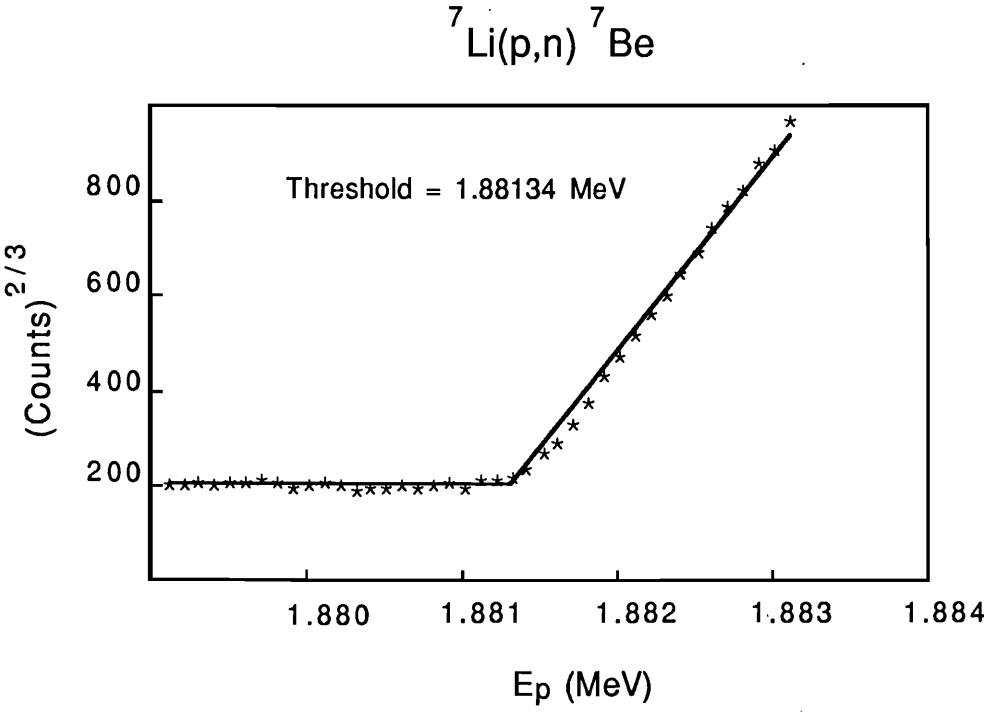
$^{7}$Li(p,n) $^{7}$Be
Threshold = 1.88134 MeV
(Counts)$^{2/3}$
800
600
400
200
1.880
1.881
1.882
1.883
1.884
Ep (MeV)

and long evaporation periods.

To monitor the current striking the target a scanner was placed between the elastic chamber and the Faraday cup assembly as shown in figure 4.5. The Faraday cup was used to perform periodic calibrations of the scanner to ensure accurate charge measurement. A $BaF_3$ neutron detector was placed directly behind the target at 0°.

Figure 4.5 shows the experimental setup. The neutron detector is a flux counter and has no energy resolving capability. The neutron counter is biased at +1300 volts; the signal is sent to a Hamner Model NB-14 preamplifier. This signal is amplified by a Hammner Model NA-12 amplifier and then sent to an Ortec Model 142A spectroscopy amplifier. After this point the electronics are the same as for the detection of gamma rays.

It is conventional to calibrate each time an experiment is performed. Appreciable time and effort is expended if the neutron threshold method is used. An alternative is to use the neutron thresholds to determine the absolute energy and then to find a resonance in elastic scattering close to the threshold; this resonance serves as a secondary calibration point which may be used to conveniently calibrate the accelerator energy. Two secondary calibration resonances chosen are the $1/2^+$ 65 eV wide resonance at 1.8839 MeV in $^{44}$Ca(p,p), and the $3/2^+$ 38 eV resonance at 3.2373 MeV in $^{56}$Fe(p,p). The $^{44}$Ca(p,p) resonance and the $^{56}$Fe(p,p) resonance is shown at 4 angles in figure 4.6. The preparation of the $^{44}$Ca and $^{56}$Fe target are described by Wilson [Wi73] and Watson [Wa80], respectively. Both targets are relatively easy to prepare. The preparation method for the $^{56}$Fe targets was changed to use an open tungsten boat.

Figure 4.5 Experimental Setup for Neutron Detection. The target is in the endcap.

# Neutron Detection Set Up

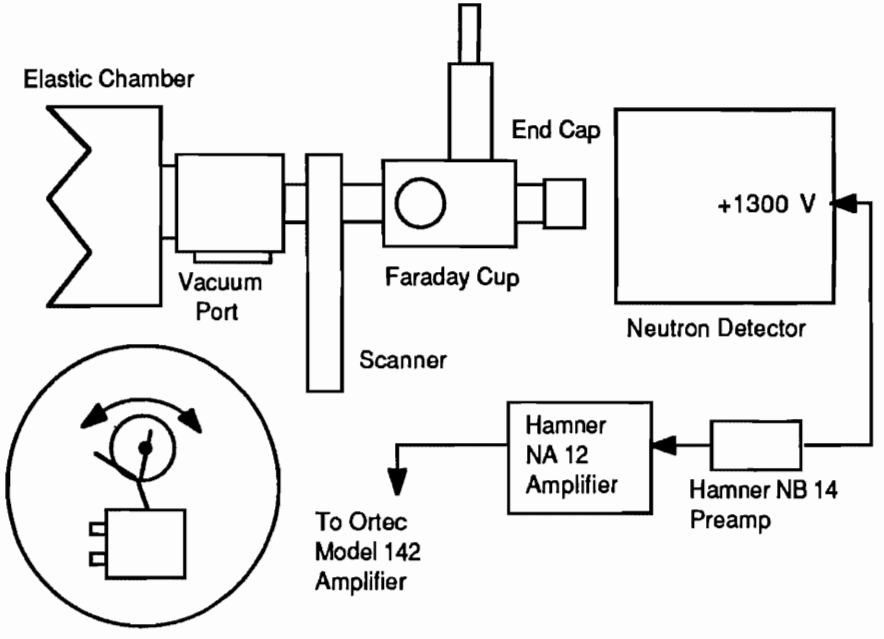

Figure 4.6 $^{44}Ca(p,p)$ and $^{56}Fe(p,p)$ Yield Curves Showing the Secondary Standard Resonances.

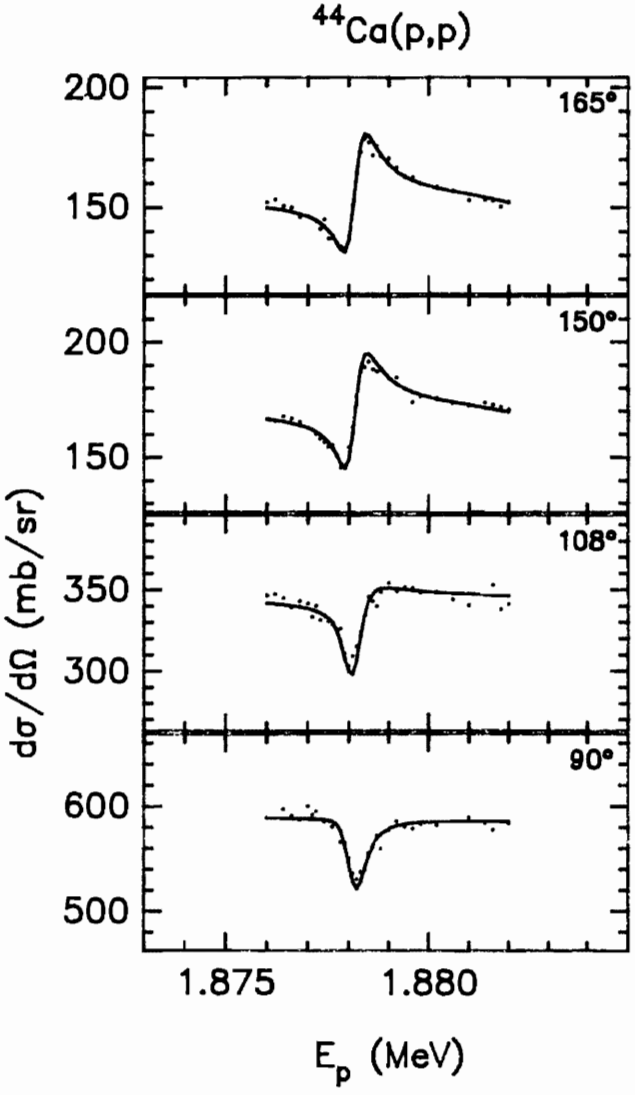
$^{44}$Ca(p,p)
165°
150°
108°
90°
200
150
350
300
600
500
dσ/dΩ (mb/sr)
1.875
1.880
E$_p$ (MeV)

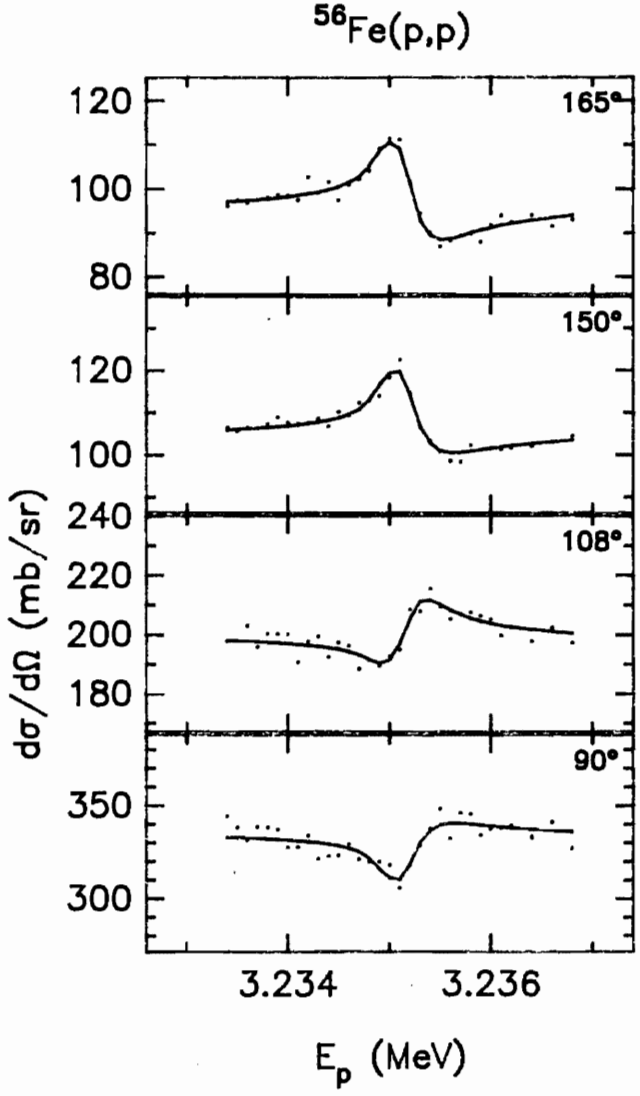
$^{56}$Fe(p,p)
165°
150°
108°
90°
120
100
80
240
220
200
180
350
300
dσ/dΩ (mb/sr)
3.234
3.236
E$_p$ (MeV)

# CHAPTER V

# DATA AND ANALYSIS

## A. Shape Analysis

The elastic data are analyzed using the program MULTI6. The basis of this analysis is equation 2.19. In this equation the cross section is proportional to the sum of the amplitudes squared. The squaring gives cross (interference) terms which contribute constructively or destructively to the cross section. The interference may be between the Coulomb scattering amplitude and a resonance amplitude, between different resonance amplitudes, or both.

The incident particle spin is i=1/2 and target spin I=0, which gives total entrance channel spin s=**i**+**I**=1/2. The channel spin adds vectorially with the orbital angular momentum to form $J=\ell+1/2$ or $J=\ell-1/2$. For elastic scattering the exit channel may form the same combinations for $J=\ell'+1/2$ or $J=\ell'-1/2$.

In the case of inelastic scattering the $^{28}$Si core is left in the first excited state with spin I'=2 and the exiting proton has a spin of i'=1/2. These two angular momenta add vectorially to form the channel spin $s_1'= 3/2$ or $s_2'= 5/2$. The decay of the compound state by the inelastic channel may occur through several different channels. The possible ways to form a state with total spin and parity of $J^{\pi}$ in the exit channel are determined by satisfying the triangle inequality, $|\ell'-s_{1,2}'| \leq J \leq |\ell'+s_{1,2}'|$ with $\ell$ having the correct parity given by $(-)^{\ell}$.

The decay of the compound state may occur by channels which have the same

orbital angular momentum $\ell$' but different channel spins. This is called channel spin or s-mixing. For that case the total inelastic width will be the sum of the partial widths for decay with the various channel spins. The decay of the compound state also may occur by exiting through the same channel spin but different $\ell$ values; this is called $\ell$-mixing. In general s-mixing and $\ell$-mixing can occur simultaneously. The possible s and $\ell$ values for entrance and exit channels with total $J^{\pi}$ are summarized in table 5.1. In practice exit orbital angular momenta $\ell$'=5 and 6 may be neglected.

Figure 5.1 shows several different elastic resonances with the same laboratory width but different J and $\ell$ values. For the resonance on the left $J^{\pi}=3/2^{-}$, $\ell=1$ and $J^{\pi}=1/2^{-}$, $\ell=1$ resonance shapes are shown. Although the resonances have approximately the same shape the $J^{\pi}=3/2^{-}$ resonance shows a larger amplitude than the $J^{\pi}=1/2^{-}$ resonance. The shapes are typical for a p-wave ($\ell=1$) resonance. The constructive interference in the 90° yield is typical of a negative parity resonance.

The resonances on the right hand side have $J^{\pi}=5/2^{+}$, $\ell=2$ and $J^{\pi}=3/2^{+}$, $\ell=2$. The shapes of these resonances are clearly different from the resonances with $J^{\pi}=3/2^{-}$ and $J^{\pi}=1/2^{-}$. These shapes are typical for a d-wave ($\ell=2$) resonance. The amplitude is determined by $J^{\pi}$ as is shown at 165°. The resonance at 90° shows the destructive interference typical of positive parity resonances.

## B. Resonances Observed In $^{28}$Si(p,p) and $^{28}$Si(p,p') Reactions

### 1. $E_p$= 1.6494 MeV Resonance

Table 5.1

| | Possible s and $\ell$ combinations | | | |
|---|---|---|---|---|
| | Elastic ($I^{\pi}=0^{+}$) | | Inelastic ($I^{\pi}=2^{+}$) | |
| $J^{\pi}$ | s | $\ell$ | s' | $\ell$' |
| 1/2+ | 1/2 | 0 | 3/2 | 2 |
| | | | 5/2 | 2 |
| 1/2- | 1/2 | 1 | 3/2 | 1 |
| | | | 5/2 | 3 |
| 3/2+ | 1/2 | 2 | 3/2 | 0 |
| | | | | 2 |
| | | | 5/2 | 2 |
| | | | | 4 |
| 3/2- | 1/2 | 1 | 3/2 | 1 |
| | | | | 3 |
| | | | 5/2 | 1 |
| | | | | 3 |
| 5/2+ | 1/2 | 2 | 3/2 | 2 |
| | | | | 4 |
| | | | 5/2 | 0 |
| | | | | 2 |
| | | | | 4 |
| 5/2- | 1/2 | 3 | 3/2 | 1 |
| | | | | 3 |
| | | | 5/2 | 1 |
| | | | | 3 |
| | | | | 5 |
| 7/2+ | 1/2 | 4 | 3/2 | 2 |
| | | | | 4 |
| | | | 5/2 | 2 |
| | | | | 4 |
| | | | | 6 |
| 7/2- | 1/2 | 3 | 3/2 | 3 |
| | | | | 5 |
| | | | 5/2 | 1 |
| | | | | 3 |
| | | | | 5 |

Figure 5.1 Shapes for p-wave ($\ell$=1) and d-wave ($\ell$=2) Resonances.

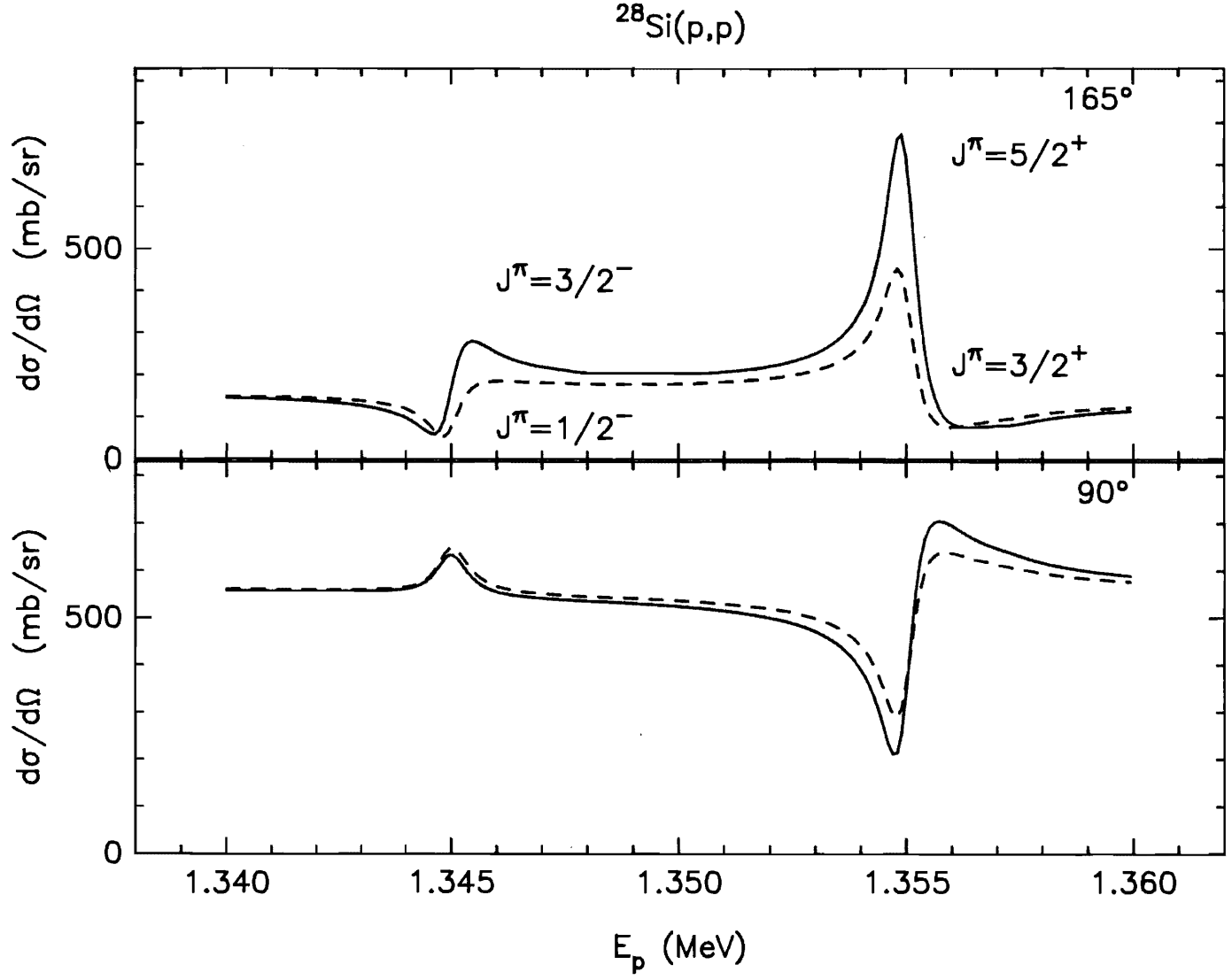
$^{28}$Si(p,p)
165°
$J^\pi=5/2^+$
$J^\pi=3/2^-$
$J^\pi=3/2^+$
$J^\pi=1/2^-$
90°
dσ/dΩ (mb/sr)
500
0
1.340
1.345
1.350
1.355
1.360
$E_p$ (MeV)

Vorona [Vo59] obtained a spin and parity of $J^{\pi}=3/2^-$ and an elastic width of $\Gamma_p=55\pm6$ keV from analysis of elastic scattering data. Klucharev [Kl72] obtained $3/2^-$ and an elastic width $\Gamma_p=46\pm2$ keV from a polarization study of elastically scattered protons from $^{28}$Si. Ejiri [Ej64] measured the gamma-ray yield and obtained a total width $\Gamma=56\pm6$ keV. The anisotropy of the 4.35 MeV gamma rays emitted from the decay of this level to the ground state were measured and found consistent with the $J^{\pi}=3/2^-$ assignment.

Byrski [By74] obtained a width of $\Gamma= 52.0\pm0.8$ keV from the gamma-ray yield. The anisotropy between 0° and 90° was measured for the $E_\gamma= 4.34$ MeV gamma ray from the decay of this level to the ground state and was determined to be consistent with a negative parity assignment.

Van Oostrum [Oo61] obtained a total width $\Gamma=44\pm4$ keV for this level from the gamma-ray yield, while Barnes [Ba73] confirmed the $J^{\pi}=3/2^-$ assignment for the resonance by measuring the angular distributions of the cascade gamma rays from this level to the first excited state at $E_x=1.38$ MeV to the ground state, which emit gamma rays with energies of 2.96 and 1.38 MeV, respectively.

The data and multilevel analysis from this experiment are shown in figure 5.2. The assignment for the spin and parity from this fit is $J^{\pi}=3/2^-$. The width that gave the best fit is $\Gamma_p=45\pm5$ keV, in agreement with the above references.

2. $E_p= 2.0855$ MeV Resonance

Klucharev [Kl72] assigned a spin and parity to the $E_x=4.76$ MeV level of $J^{\pi}=1/2^+$ using polarization measurements of elastically scattered protons on $^{28}$Si. No

Figure 5.2 Multilevel Fit to the $^{28}$Si(p,p) Data in the Energy Range $E_p$=1.4 MeV to 2.6 MeV.

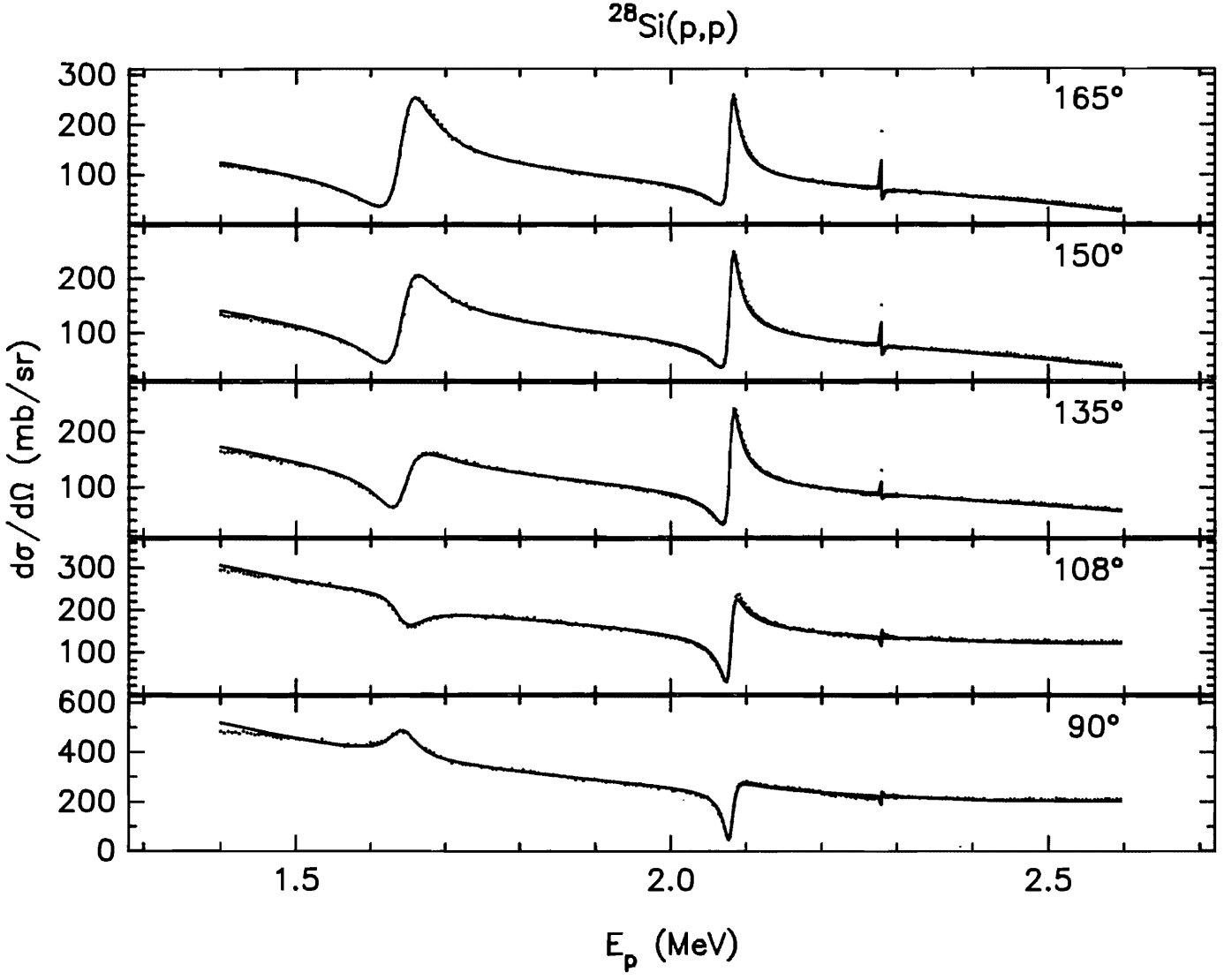
$^{28}$Si(p,p)
165°
150°
135°
108°
90°
dσ/dΩ (mb/sr)
300
200
100
600
400
0
1.5
2.0
2.5
$E_p$ (MeV)

value for the width was given.

Vorona [Vo59] and Belote [Be61] assigned spin and parity of $J^{\pi}=1/2^{+}$ using a single level approximation analysis. The widths from both authors agreed and were $\Gamma_p$=18±5 keV and $\Gamma_p$=18.6 keV, respectively.

Barnes [Ba73] concurs with the spin and parity assignment of $J^{\pi}=1/2^{+}$ and the total width of $\Gamma$=16±3 keV.

Byrski [By74] and Ejiri [Ej64] determined from the gamma-ray yield that the width of this resonance is $\Gamma$=15.6±0.6 keV and $\Gamma$=18.0±5.0 keV, respectively. No spin and parity was assigned by either author.

Van Oostrum [Oo61] measured the $E_x$=4.76 MeV gamma-ray angular distribution from the decay of this state to the ground state and found it consistent with a spin of J=1/2. From the gamma-ray yield Van Oostrum determined the width as $\Gamma_p$=15±3 keV.

The results from this experiment agree with the above values. The data and a multilevel fit are shown in figure 5.2. The spin and parity assigned was $J^{\pi}=1/2^{+}$. The width was measured to be $\Gamma_p$=14±2 keV. This value for the width agrees with Van Oostrum [Oo61] and Barnes [Ba73].

3. $E_p$= 2.28661 MeV Resonance

Byrski [By74] concluded from $\gamma-\gamma$ correlations that $J^{\pi}=5/2^{+}$ for this resonance. An estimate of the upper limit on the elastic width was placed at $\Gamma_p < 2$ keV. Karadzhev [Ka74] agreed with $J^{\pi}=5/2^{+}$ from a measurement of the $^{28}$Si(p,p) and $^{28}$Si(p,p'$\gamma$) reactions; he placed an upper limit of $\Gamma_p = 1$ keV on the width of the resonance.

The extremely good experimental beam energy resolution in this experiment per-

mitted an accurate determination of the location and width of this resonance. The data and multilevel fit are shown in figure 5.3. From the dip in the cross section at the 90° angle the resonance has positive parity. The spin and parity was assigned $J^{\pi}=5/2^{+}$. The width was determined to be $\Gamma_p$= 80±10 eV.

4. $E_p$= 2.8955 MeV Resonance

Klucharev [Kl72] determined from polarization measurements that the width for the $E_p$= 2.880 MeV level is $\Gamma_p$= 360±10 keV. His assignment for the spin and parity was $J^{\pi}= 1/2^{-}$.

Vorona [Vo59] and Belote [Be61] assigned $J^{\pi}=1/2^{-}$ for this resonance. Vorona lists the elastic width as $\Gamma_p$=500±100 keV and Belote as $\Gamma_p$=400±60 keV.

Ejiri [Ej64] determined from the gamma-ray yield that the width was $\Gamma_p$= 425±50 keV. No spin assignment was given.

This experiment determined an elastic width of $\Gamma_p$=475±50 keV with $J^{\pi}=1/2^{-}$. This agreed with Vorona and Belote. No inelastically scattered protons were observed at this resonance. A multilevel fit to the elastic data is shown in figure 5.4.

5. $E_p$= 3.1024 MeV Resonance

The analysis of this level led to an assignment of $J^{\pi}=7/2^{-}$. This is in contrast with Vorona [Vo59], Belote [Be61], and Gearhart [Ge74], who assigned the level a spin of J=5/2. Vorona and Belote assigned a negative parity to this level. Both used shape anal-

Figure 5.3 Multilevel Fit to the $^{28}Si(p,p)$ Data near the $E_p$= 2.2867 MeV Resonance. For this resonance $J^{\pi}=5/2^{+}$ and $\Gamma_p$= 80 eV.

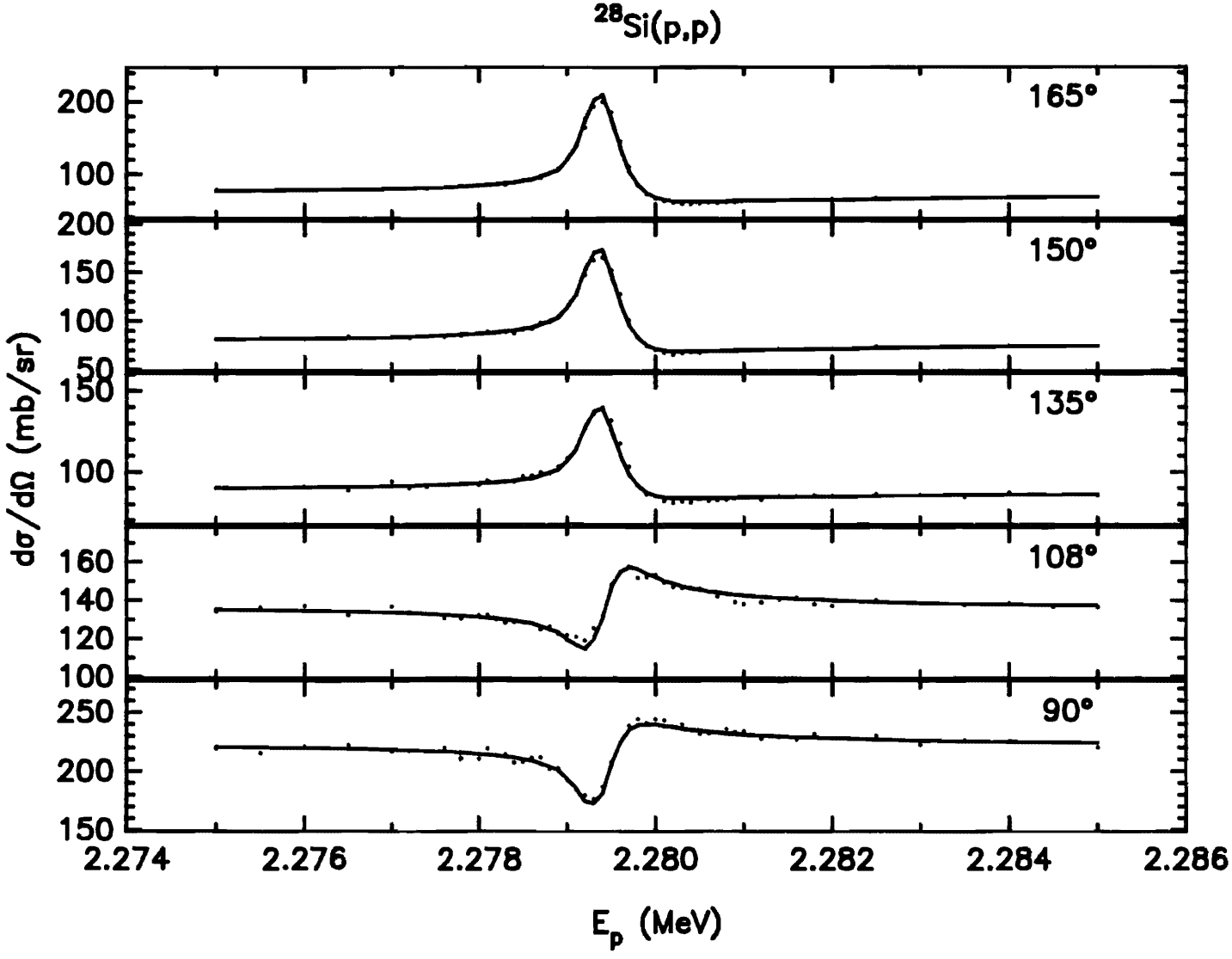
$^{28}$Si(p,p)
165°
150°
135°
108°
90°
dσ/dΩ (mb/sr)
E$_p$ (MeV)
200
100
200
150
100
50
150
100
160
140
120
100
250
200
150
2.274
2.276
2.278
2.280
2.282
2.284
2.286

Figure 5.4 Multilevel Fit to the $^{28}Si(p,p)^{28}Si$ Data from $E_p$= 2.6 MeV to 3.8 MeV.

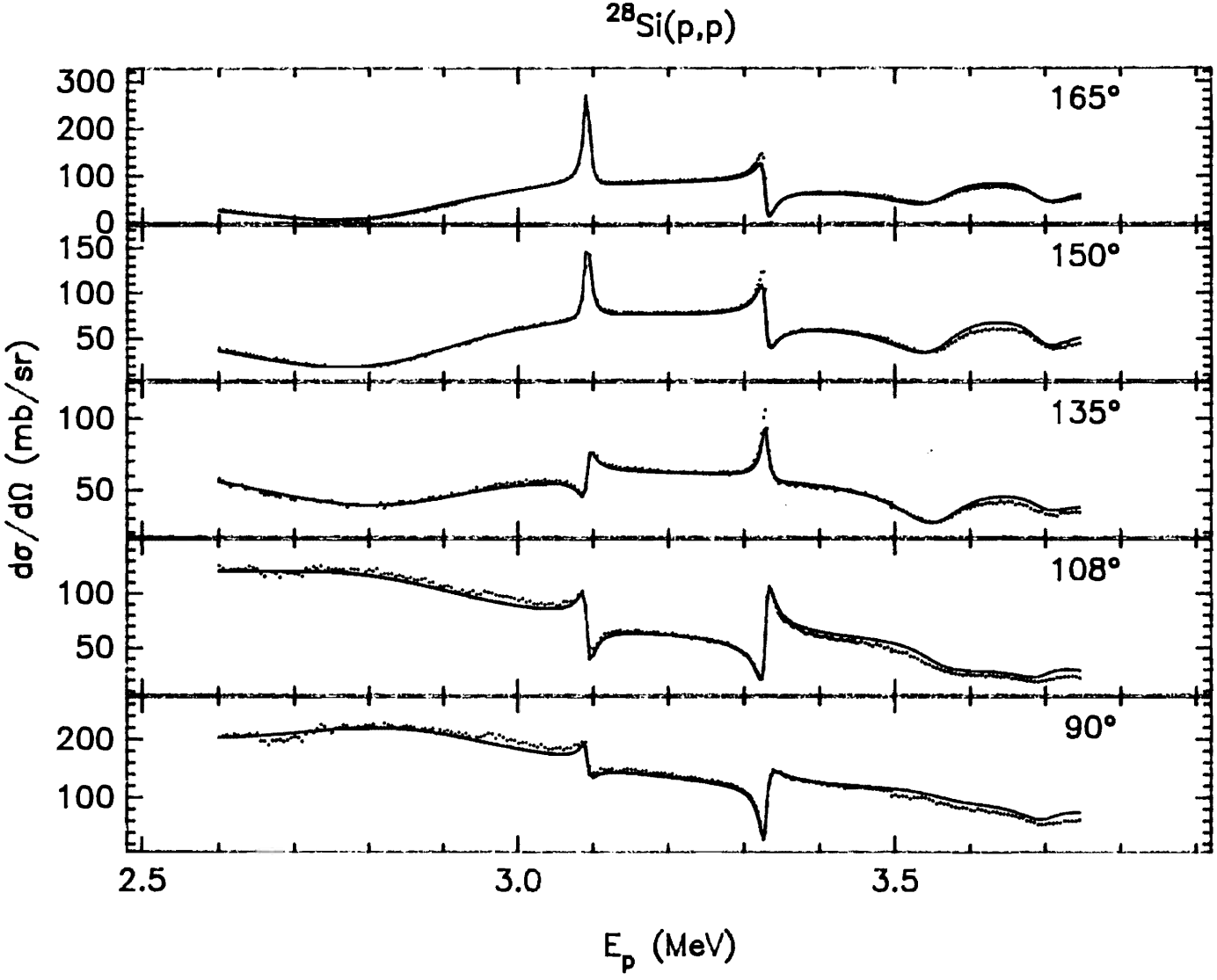
$^{28}$Si(p,p)
165°
150°
135°
108°
90°
dσ/dΩ (mb/sr)
E$_p$ (MeV)
2.5
3.0
3.5

ysis with a single level approximation. This assignment seemed to be confirmed by the angular distribution analysis of the inelastic data.

Ejiri investigated this resonance by measuring the gamma-ray yield. The width was given by Ejiri as $\Gamma_p$= 13±3.5 keV, agreeing with Vorona and Belote. However, no spin assignment was given.

The program MULTI6 included interference effects from all levels in the energy range 1.4 to 4.0 MeV. These interfering resonances were very important in determining the spin and parity of the level. The level at $E_p$=2.8661 MeV was especially important for its interference effects on the $E_p$=3.1024 MeV resonance. Figure 5.5 shows six different fits to the data from this experiment using a multilevel fit, a two level approximation, and a single level approximation.

The single level approximation shows a possible fit for $7/2^-$ and $5/2^-$ at 90° and 165°. However, at 135° neither $7/2^-$ or $5/2^-$ qualitatively fits the data. Vorona and Belote did not measure data at 135°.

The two level approximation changed the results dramatically, as shown in figure 5.5. The large $1/2^-$ 475 keV resonance at 2.8661 MeV was included with a $7/2^-$ assignment and a $5/2^-$ assignment for the level at 3.10 MeV. A possible fit is obtained at 165° for $5/2^-$, although the 135° and 90° data and fit do not agree. With $7/2^-$ for the spin and parity a good fit is obtained at all angles.

For the multilevel fit the results follow that of the two level approximation: the $7/2^-$ assignment gives an extremely good fit while the $5/2^-$ fit is qualitatively wrong.

The present widths of these levels are in good qualitative agreement with previous results. Vorona gave an elastic width of 4.3 keV and total width 14±3 keV. For the inelastic channel Vorona assigned p-wave ($\ell'$=1) decay with a channel spin mixing

Figure 5.5 A Single Level Approximation, a Two Level Approximation, and a Multilevel Fit to the $^{28}Si(p,p)$ Data near the $E_p$=3.1008 MeV Resonance. $J^{\pi}=5/2^-$ and $7/2^-$ are considered.

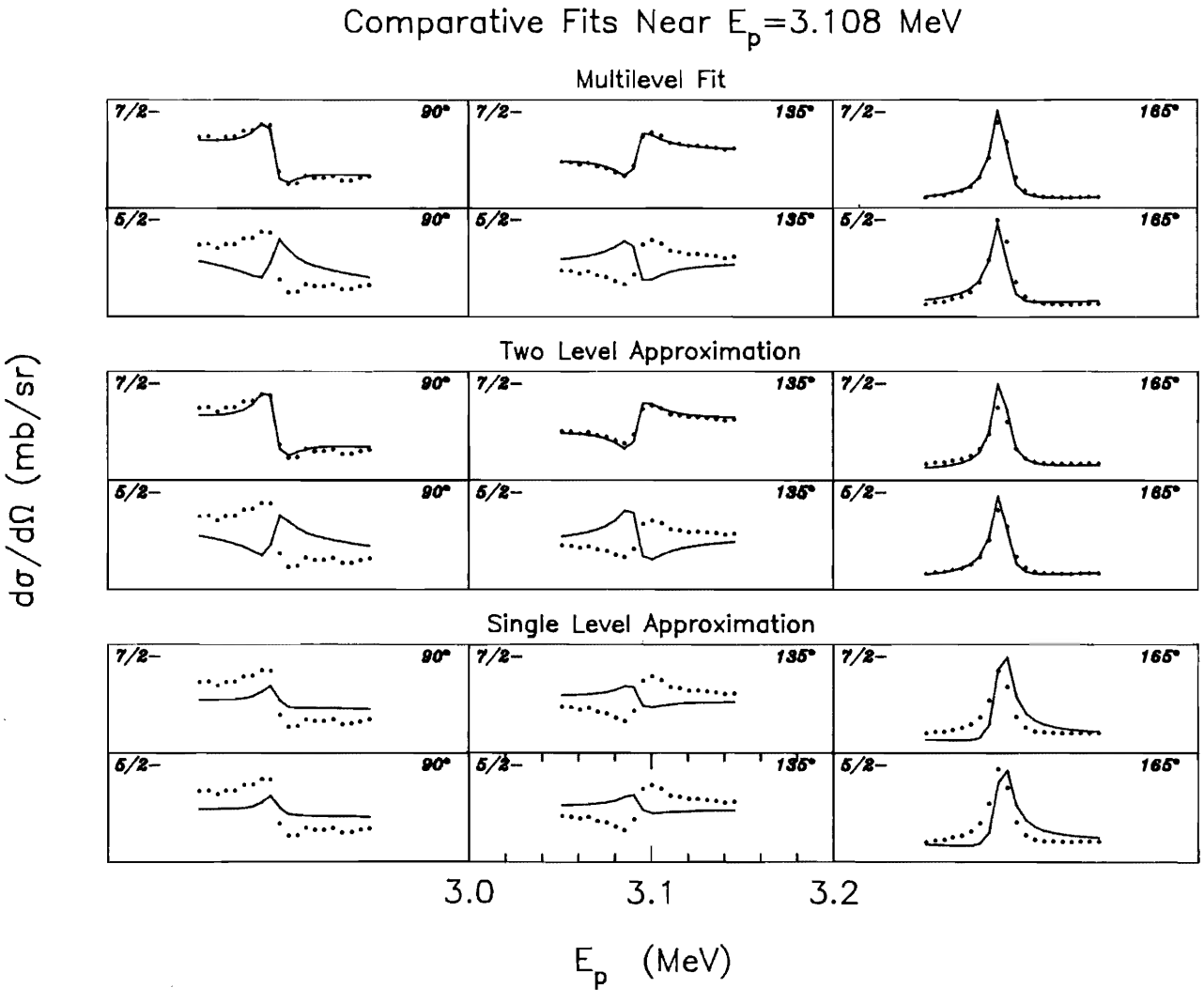
Comparative Fits Near $E_p$=3.108 MeV
Multilevel Fit
Two Level Approximation
Single Level Approximation
7/2-
5/2-
90°
135°
165°
dσ/dΩ (mb/sr)
3.0
3.1
3.2
$E_p$ (MeV)

ratio of 3/2 to 5/2 of 0.90 to 0.10. This agreed with Belote, whose elastic width assignment was 3.9 keV and total width 13.9 keV. The mixing ratio was given as 0.87 to 0.13 for 3/2 to 5/2 with a p-wave formation. This analysis gave an elastic width of $\Gamma_p$=2.8 keV and a total width of $\Gamma$=10.7 keV. The inelastic partial width obtained in this experiment is $\Gamma_p$,(s'=5/2, $\ell$'=1)=7.9 keV. The data and fit are shown in figure 5.6.

6. $E_p$= 3.3394 MeV Resonance

Vorona [Vo59] and Belote [Be61] determined the spin and parity of this resonance to be $J^\pi=3/2^+$. Vorona gave a total width of $\Gamma$=11±1 keV and Belote a total width of 8.4 keV. Vorona had an elastic width of $\Gamma_p$=9.9±1.0 keV and an inelastic width $\Gamma_p$,=1.1±0.3 keV. Belote's values were $\Gamma_p$=5.88 keV and $\Gamma_p$,=2.52 keV. Gearhart [Ge74] performed angular distribution measurements and agreed with the $J^\pi=3/2^+$ assignment.

In this experiment the total width assignment agreed closely with Vorona and was $\Gamma$=10.65 keV. The elastic width matched the data best for $\Gamma_p$=9.50 keV. The analysis of the inelastic scattering data resulted in an assignment value for the inelastic width of $\Gamma_p$,(s'=3/2, $\ell$'=0)= 1.65 keV. A multilevel fit to the elastic and inelastic data is shown in figure 5.4 and figure 5.6, respectively.

7. $E_p$= 3.5679 and $E_p$= 3.7130 MeV Resonances

Vorona [Vo59] and Belote [Be61] determined that elastic scattering alone was insufficient to determine the spin and parity of the $E_p$=3.5679 and $E_p$=3.7130 MeV reso-

Figure 5.6 Multilevel Fit to the $^{28}Si(p,p')^{28}Si^{*}$ Data from $E_p$ = 2.6 MeV to 3.8 MeV.

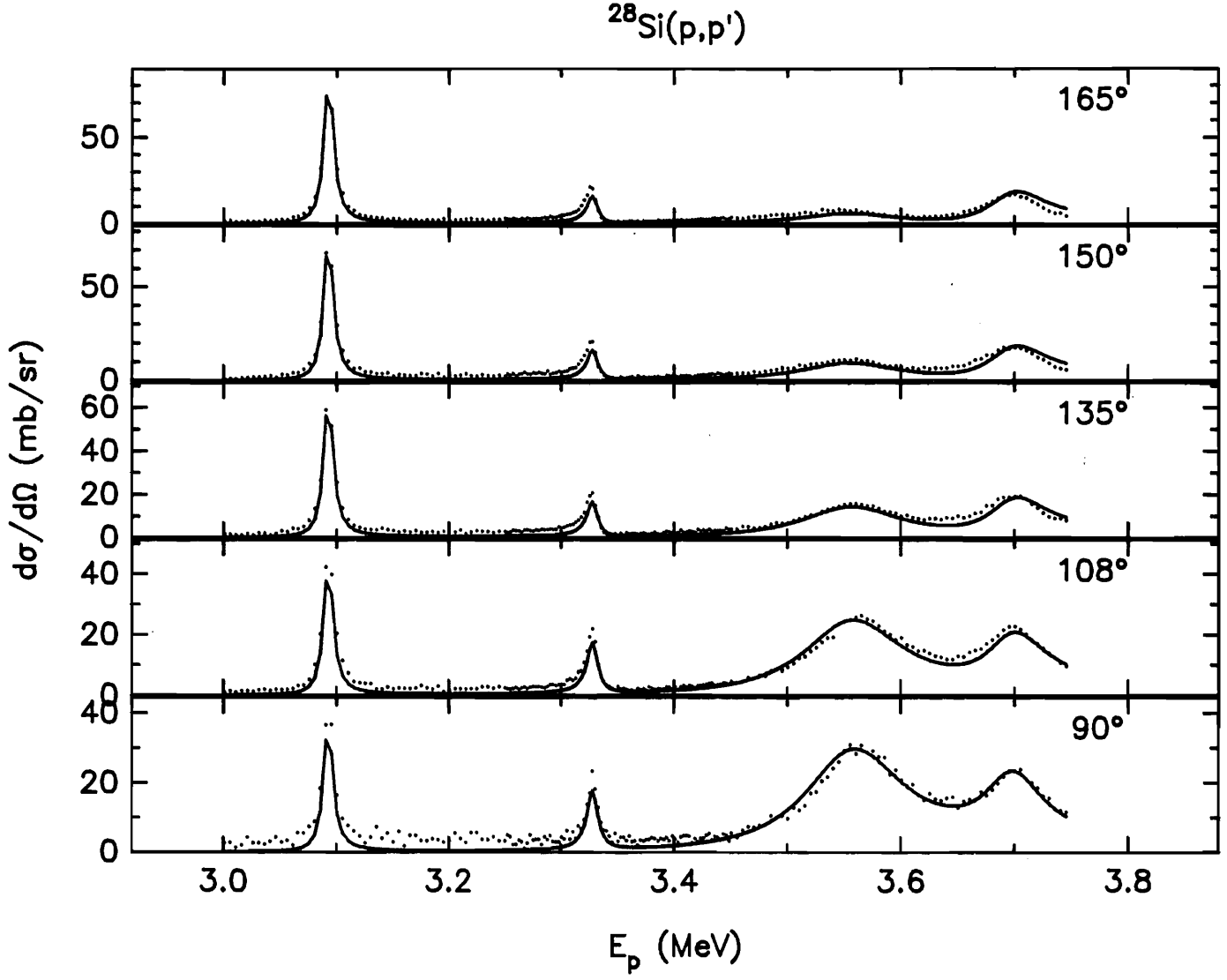
$^{28}$Si(p,p')
165°
150°
135°
108°
90°
dσ/dΩ (mb/sr)
E$_p$ (MeV)
3.0
3.2
3.4
3.6
3.8

nances. From the angular distribution of the inelastically scattered protons Vorona determined that the $E_p$=3.5679 MeV resonance had a spin and parity $J^\pi=3/2^-$. The elastic width for the $E_p$=3.5679 MeV resonance was determined to be $\Gamma_p$=12.5±3.3 keV and the inelastic width $\Gamma_{p'}$=77±14 keV. The ratio of the widths for different channel spins was $\Gamma_{p'}(s'=3/2)/\Gamma_{p'}$= 0.90 and $\Gamma_{p'}(s'=5/2)/\Gamma_{p'}$= 0.10 with a p-wave ($\ell'=1$) decay. Vorona assigned spin and parity $J^\pi=3/2^+$ to the $E_p$=3.7130 MeV level. The elastic width was given as $\Gamma_p$=10.6±4.0 keV and the inelastic width as $\Gamma_{p'}$=60±11 keV.

Belote [Be61] agreed with the assignment for the spin and parity of the $E_p$=3.5679 MeV resonance of $J^\pi=3/2^-$. The elastic width was given as $\Gamma_p$=19.6 keV and the inelastic width $\Gamma_{p'}$=78 keV. The widths associated with the channel spins from the inelastic channel were $\Gamma_{p'}(s'=3/2)/\Gamma_{p'}$=0.88 and $\Gamma_{p'}(s'=5/2)/\Gamma_{p'}$= 0.12 for p-wave ($\ell'=1$) decay, in close agreement with Vorona. However Belote assigned the $E_p$= 3.7130 MeV resonance a spin and parity of $J^\pi=1/2^-$, in disagreement with Vorona. Belote's total width was $\Gamma$=74 keV with the elastic width $\Gamma_p$=18 keV and the inelastic width $\Gamma_{p'}$= 56 keV, thus qualitatively agreeing with Vorona.

Gearhart [Ge74] measured angular correlations on the inelastically scattered protons and associated gamma-rays to determine the spins of the $E_p$=3.5645 and $E_p$=3.700 MeV resonances. He agreed with Vorona and Belote on the spin assignment for the $E_p$=3.5679 MeV resonance. Gearhart concluded that the spin and parity of the $E_p$=3.7130 MeV resonance was $J^\pi=3/2^+$, in agreement with Vorona.

In this experiment the best fit was obtained using spin and parity assignments $J^\pi=3/2^-$ and $J^\pi=3/2^+$ for the $E_p$=3.5679 MeV and $E_p$=3.7130 MeV resonances, respectively. A fit was attempted assigning spin and parity $J^\pi=1/2^-$ to the $E_p$=3.7130 MeV level, following Belote's assignment. This assignment would not even qualitatively fit

the observed data. A multilevel fit to the elastic data and the inelastic data is shown in figure 5.4 and 5.6, respectively.

The $E_p$=3.5679 MeV level has an elastic width of $\Gamma_p$= 24 keV and an inelastic width of $\Gamma_{p'}(s'=3/2, \ell=1)$ = 78 keV. The $E_p$= 3.7130 MeV level has an elastic width of $\Gamma_p$=11 keV and an inelastic width $\Gamma_{p'}$=49.0 keV. The fit indicated $\ell$-mixing with $\Gamma_{p'}(s'=3/2, \ell'=0)/\Gamma_{p'}$=0.92 and $\Gamma_{p'}(s'=3/2, \ell'=2)/\Gamma_{p'}$=0.08. A compilation of previous and present results on these resonances is given in Table 5.2 and a list of resonance parameters determined in this experiment in Table 5.3.

B. Resonances Observed Only in the Gamma-Ray Yield

2. 1.3769 MeV Resonance

The gamma-ray yield was used to locate the $7/2^+$ resonance at 1.3769 MeV. Once the peak was detected and the energy of the resonance found, a very high count elastic yield was taken. In the preliminary run no signal was detected in the elastic channel where a resonance was seen in the gamma-ray channel.

A strength $((2J+1)\Gamma_p\Gamma_\gamma/\Gamma)$ for the resonance was calculated from the gamma-ray yield and a value of 106 meV was obtained. This compares with the value found by Byrski [By74] of 63 ± 13 meV.

Measurements of the lifetime of this state had been made by several investigators; Barnes [Ba73], Monohan [Mo70], and Williams [Wi70]. The values for the lifetimes were respectively 13±5 fs, 15±4 fs, and 13±6 fs, which corresponded to total widths of 50±19, 44±12, and 50±23 meV. With these total widths the usual approxima-

Table 5.2

$^{29}$P Parameter Compilation

| $E_p$(MeV)[ref] | $E_x$(MeV) | $J^\pi$ | $\Gamma$(keV) | $\Gamma_p$(keV) | $\Gamma_{p'}$(keV) |
|---|---|---|---|---|---|
| **1.3769*** | **4.070** | **7/2$^+$** | **<0.002** | **<0.002** | - |
| 1.3802[e] | 4.080 | 7/2$^+$ | < 2 | < 2 | - |
| 1.3830[f] | 4.082 | | < 3 | < 3 | - |
| 1.3810 | 4.081 | 7/2$^+$ | | - | - |
| **1.6494*** | **4.340** | **3/2$^-$** | **45±5** | **45±5** | **-** |
| 1.660[a] | 4.327 | 3/2$^-$ | 55±8 | 55±8 | - |
| 1.652[c] | 4.319 | | 46±2 | 46±2 | - |
| 1.652[e] | 4.343 | | 52±0.8 | 52±0.8 | - |
| 1.652[f] | 4.345 | 3/2$^-$ | 56±6 | | - |
| 1.652[g] | 4.340 | | 44±4 | | |
| 1.652[h] | 4.343 | 3/2$^-$ | | | |
| 1.961[e] | 4.642 | | - | - | - |
| **2.0855*** | **4.761** | **1/2$^+$** | **14±2** | **14±2** | **-** |
| 2.090[a] | 4.742 | 1/2$^+$ | 18±4 | 18±4 | - |
| 2.080[b] | 4.732 | 1/2$^+$ | 18.6 | 18.6 | - |
| 2.080[c] | 4.759 | 1/2$^+$ | | | |
| 2.083[e] | 4.759 | | 15.6±0.6 | 15.6±0.6 | |
| 2.086[f] | 4.761 | | 18±5 | 18±5 | |
| 2.090[g] | 4.760 | 1/2$^+$ | 15±3 | 15±3 | |
| 2.080[h] | 4.760 | 1/2$^+$ | 16±3 | | |
| **2.2866*** | **4.955** | **5/2$^+$** | **.080±.005** | **.080±.005** | **-** |
| 2.2847[e] | 4.954 | 5/2$^+$ | < 2 | < 2 | |
| 2.3020[i] | 4.970 | 5/2$^+$ | < 1 | < 1 | |
| **2.6302*** | **5.288** | **7/2$^+$** | **0.012** | **<0.002** | **0.010** |
| 2.6355[e] | 5.293 | 7/2 | < 2 | < 2 | - |
| 2.6540[i] | 5.300 | | | | 0.00041 |

| $E_p$(MeV)[ref] | $E_x$(MeV) | $J^\pi$ | $\Gamma$(keV) | $\Gamma_p$(keV) | $\Gamma_{p'}$(keV) |
|---|---|---|---|---|---|
| **2.8955*** | **5.544** | **1/2⁻** | **475±50** | **475±50** | **-** |
| 2.8800[a] | 5.549 | 1/2⁻ | 500±100 | 500±100 | - |
| 2.8800[b] | 5.550 | 1/2⁻ | 400±60 | 400±60 | - |
| 2.8800[d] | 5.549 | | 360±10 | 360±10 | - |
| 2.8800[f] | 5.530 | | 425±50 | 425±50 | |
| **3.1024*** | **5.7434** | **7/2⁻** | **11.5±1.8** | **2.8±0.5** | **7.9±1.3** |
| 3.100[a] | 5.739 | 5/2⁻ | 12±1 | 3.7±.8 | 8.3±1 |
| 3.095[b] | 5.734 | 5/2⁻ | 12.9 | 3.9 | 9 |
| 3.100[d] | 5.739 | 5/2 | | | |
| 3.111[f] | 5.751 | | 13.5±3.5 | 4.5±1.5 | 9±2 |
| **3.3394*** | **5.9720** | **3/2⁺** | **10.65±1.5** | **9.5±1.2** | **1.65±.4** |
| 3.337[a] | 5.968 | 3/2⁺ | 11±1 | 9.9±1 | 1.1±.3 |
| 3.334[b] | 5.965 | 3/2⁺ | 8.4 | 6.4 | 2.0 |
| 3.330[d] | 5.961 | 3/2⁺ | | | |
| **3.5679*** | **6.1879** | **3/2⁻** | **99±10** | **24±2.5** | **78±5** |
| 3.571[a] | 6.191 | 3/2⁻ | 90±15 | 12.6±3.3 | 77±14 |
| 3.571[b] | 6.191 | 3/2⁻ | 98. | 20. | 78. |
| 3.570[d] | 6.190 | 3/2 | | | |
| **3.7130*** | **6.2410** | **3/2⁺** | **57±8** | **11±3** | **49±7** |
| 3.710[a] | 6.238 | 3/2⁺ | 70±12 | 10.5±4 | 60±11 |
| 3.710[b] | 6.238 | 1/2⁻ | 74. | 18. | 56. |
| 3.710[d] | 6.238 | 3/2 | | | |

a. Vo59, b. Be61, c. Kl72, d. Ge74, e. By74, f. Ej64, g. Oo61, h. Ba73, i. Ka74
* Present experiment

Table 5.3

Resonance Parameters for $^{28}Si(p,p)^{28}Si$ and $^{28}Si(p,p')^{28}Si^*$

| $E_p$(MeV) | $J^\pi$ | $\ell$' | s' | $\Gamma_p$(keV) | $\gamma_p^2$(keV) | $\Gamma_{p'}$(keV) | $\gamma_{p'}^2$(keV) |
|---|---|---|---|---|---|---|---|
| 1.3769 | $7/2^+$ | 4 | 1/2 | < 0.002 | | | |
| 1.6494 | $3/2^-$ | 1 | 1/2 | 45.5 | 768.7 | | |
| 2.0855 | $1/2^+$ | 0 | 1/2 | 14.0 | 33.9 | | |
| 2.2866 | $5/2^+$ | 2 | 1/2 | 0.080 | 1.84 | | |
| 2.6302 | $7/2^+$ | 4 | 1/2 | < 0.002 | < 4.0 | | |
| | | 2 | 3/2 | | | 0.0010 | 206.1 |
| 2.8955 | $1/2^-$ | 1 | 1/2 | 475. | 856.9 | | |
| 3.1024 | $7/2^-$ | 3 | 1/2 | 2.8 | 129.0 | | |
| | | 1 | 5/2 | | | 7.9 | 592.2 |
| 3.3394 | $3/2^+$ | 2 | 1/2 | 9.5 | 40.3 | | |
| | | 0 | 3/2 | | | 1.65 | 15.6 |
| 3.5679 | $3/2^-$ | 1 | 1/2 | 24. | 24.6 | | |
| | | 1 | 3/2 | | | 78.0 | 32.0 |
| | | 3 | 3/2 | | | 9.0 | 1062 |
| 3.7130 | $3/2^+$ | 2 | 1/2 | 11 | 31.6 | | |
| | | 0 | 3/2 | | | 45.0 | 164.0 |
| | | 2 | 3/2 | | | 4.0 | 253.4 |

tion of $\Gamma_p >> \Gamma_\gamma$ cannot be made.

A calculation of $\Gamma_p$ using these experimental values for the strengths and the values of the total width given by Barnes Ba[73] results in two possible values: $\Gamma_p$=19 meV or $\Gamma_p$=31 meV.

Determining an upper limit for such a weak resonance is governed by the statistical fluctuations in the counting process. These fluctuations can be estimated by $N^{1/2}$, where N is the number of protons detected. In order to determine whether the resonance would be detectable above the noise a Monte Carlo simulation of a $7/2^+$ 1 eV and 2 eV resonance was performed. The results are shown in figure 5.7. At 50,000 and 100,000 counts the signal for a 1 eV resonance would be undetectable. However, a 2 eV resonance would be clearly seen at 165°. At 250,000 counts it is reasonable to expect to see a 1 eV resonance at 165°.

The gamma-ray yield in figure 5.8 shows clearly a resonance near 1.380 MeV. Figure 5.9 shows the elastic yield taken near this energy with a possible signature of a resonance at 165°. A tentative fit with $\Gamma_p$=1 eV is also shown. No signal is observed at the other four angles; this agrees with the simulation for a 1 eV resonance. At approximately 300,000 counts per point the resonance would have been observed if it is 1 eV or larger. It may be assigned an upper limit of less than 2 eV.

### 2. 2.6302 MeV Resonance

Endt [En78] lists two experiments in which the $E_p$=2.6302 MeV resonance was observed [By74] and [Ka75]. Both gave a spin assignment of J=7/2, but no parity assign-

Figure 5.7 Simulation of a $7/2^+$ Resonance Near $E_p$= 1.380 MeV. The simulation provides an indication of whether this resonance would be observed for different total number of counts and for different widths. The resolution is assumed to be 350 eV.

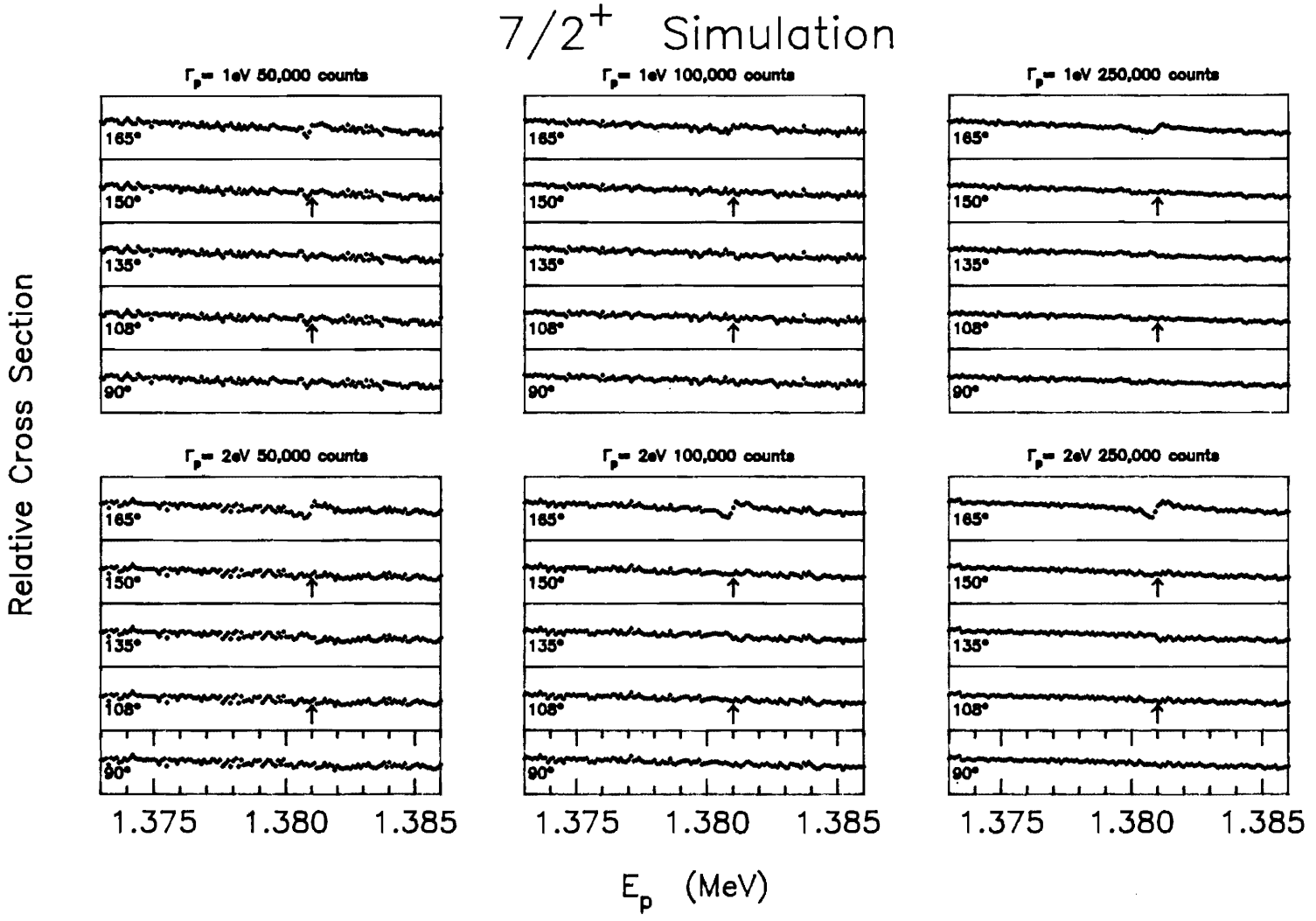
7/2+ Simulation
Γp= 1eV 50,000 counts
Γp= 1eV 100,000 counts
Γp= 1eV 250,000 counts
Γp= 2eV 50,000 counts
Γp= 2eV 100,000 counts
Γp= 2eV 250,000 counts
165°
150°
135°
108°
90°
Relative Cross Section
1.375
1.380
1.385
Ep (MeV)

Figure 5.8 Gamma-ray Yield near $E_p$= 1.3769 MeV.

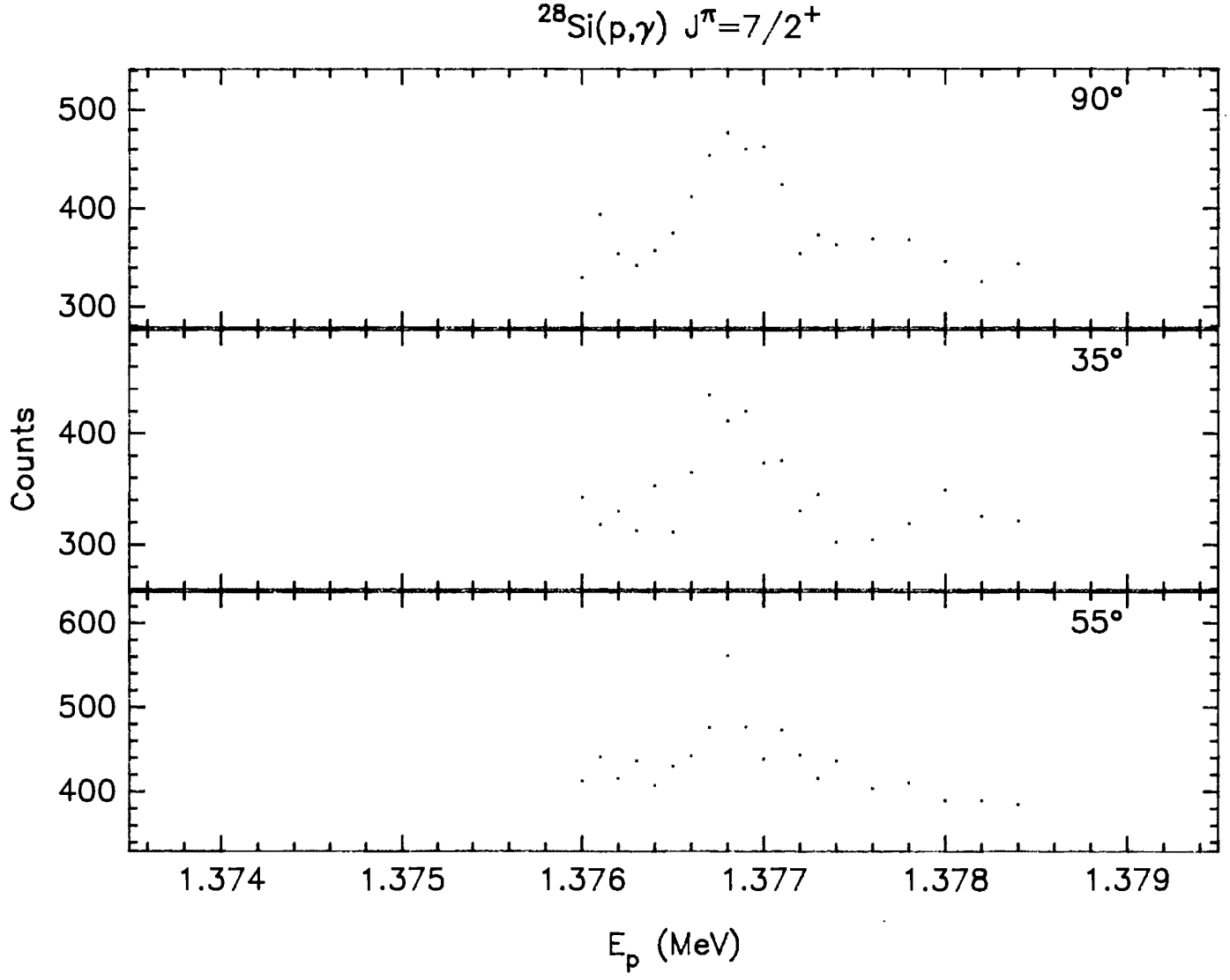
$^{28}$Si(p,γ) $J^{\pi}=7/2^{+}$
90°
35°
55°
Counts
500
400
300
400
300
600
500
400
1.374
1.375
1.376
1.377
1.378
1.379
$E_p$ (MeV)

Figure 5.9 $^{28}$Si(p,p) Data and Fit near $E_p$=1.3769 MeV.

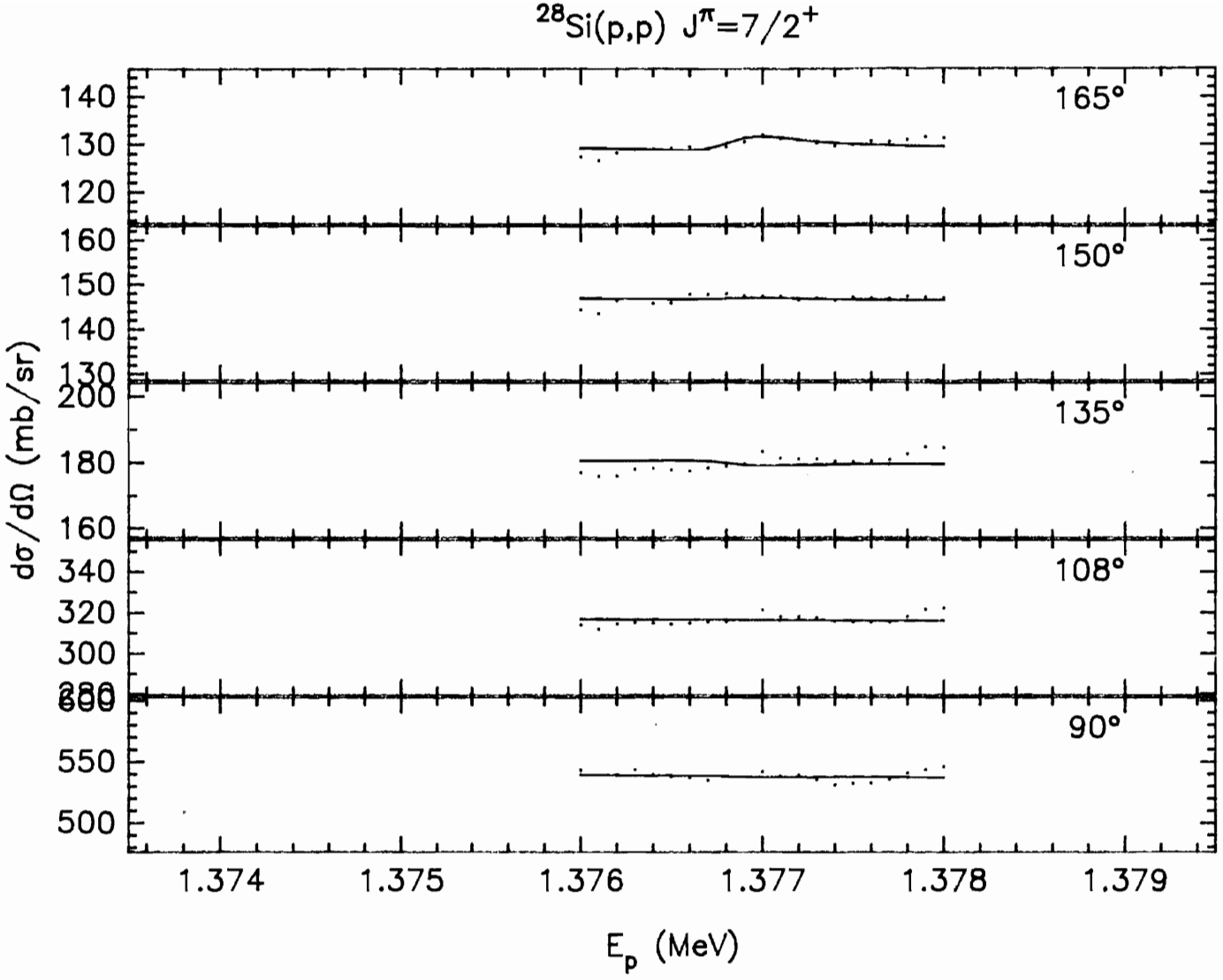
$^{28}$Si(p,p) $J^{\pi}=7/2^{+}$
165°
150°
135°
108°
90°
dσ/dΩ (mb/sr)
140
130
120
160
150
140
130
200
180
160
340
320
300
280
550
500
1.374
1.375
1.376
1.377
1.378
1.379
$E_p$ (MeV)

ment was made. Byrski [By74] places an upper limit on the elastic width of less than 2 keV.

The target was prepared from $SiO_2$ enriched to 99.58% $^{28}Si$. The other isotopes were $^{29}Si$ (0.26%) and $^{30}Si$ (0.16%). Bornmangh [Bo67] and Outlaw [Ou76] list resonances in $^{30}Si(p,\gamma)$ and $^{30}Si(p,p)$ at $E_p$=2.632 and 2.641 MeV with relative strengths of about four to one. Since the capture strength $((2J+1)\Gamma_p\Gamma_\gamma/\Gamma)$ at $E_p$=2.632 MeV is very strong (7.1 eV), the possibility that this resonance in $^{30}Si$ was mistakenly identified as a resonance in $^{29}Si$ had to be considered. According to Hemsky [He73] and Nelson [Ne83a] no resonance was observed in this region for the capture reaction in $^{29}Si$. The energies of the major contributing peaks in the gamma-ray spectrum were studied and compared with the energetics of the decays from the resonance in $^{30}Si(p,\gamma)^{31}P$ to determine if the resonance observed in the gamma-ray yield could be attributed to the $^{30}Si(p,\gamma)$ reaction. For the $E_p$=2.632 MeV resonance Bornmangh [Bo67] assigns a branching ratio of 20% to the ground state, 33% to the first excited state, and 30% to the second excited state. The decay energies from the first and second excited states to the ground state are 1.27 MeV and 2.23 MeV, respectively. If the resonance in the gamma-ray yield is attributed to this level in $^{30}Si(p,\gamma)^{31}P$ then there should be strong peaks in the gamma-ray spectrum at these energies. No peaks at these gamma-ray energies were observed. At resonance two peaks became highly visible in the gamma-ray spectrum, one with an energy of 1.922 MeV and the other with an energy of 1.40 MeV. These lines correspond to the second and first excited states in $^{29}P$.

A Monte-Carlo simulation was performed to examine the effect of a 1 eV and 2 eV $7/2^+$ resonance with 50,000, 100,000, and 250,000 counts; this simulation is shown in figure 5.10. The 1 eV resonance is seen only in the simulation for which 250,000

Figure 5.10 Simulation of a $7/2^+$ Resonance at $E_p$=2.6302 MeV.

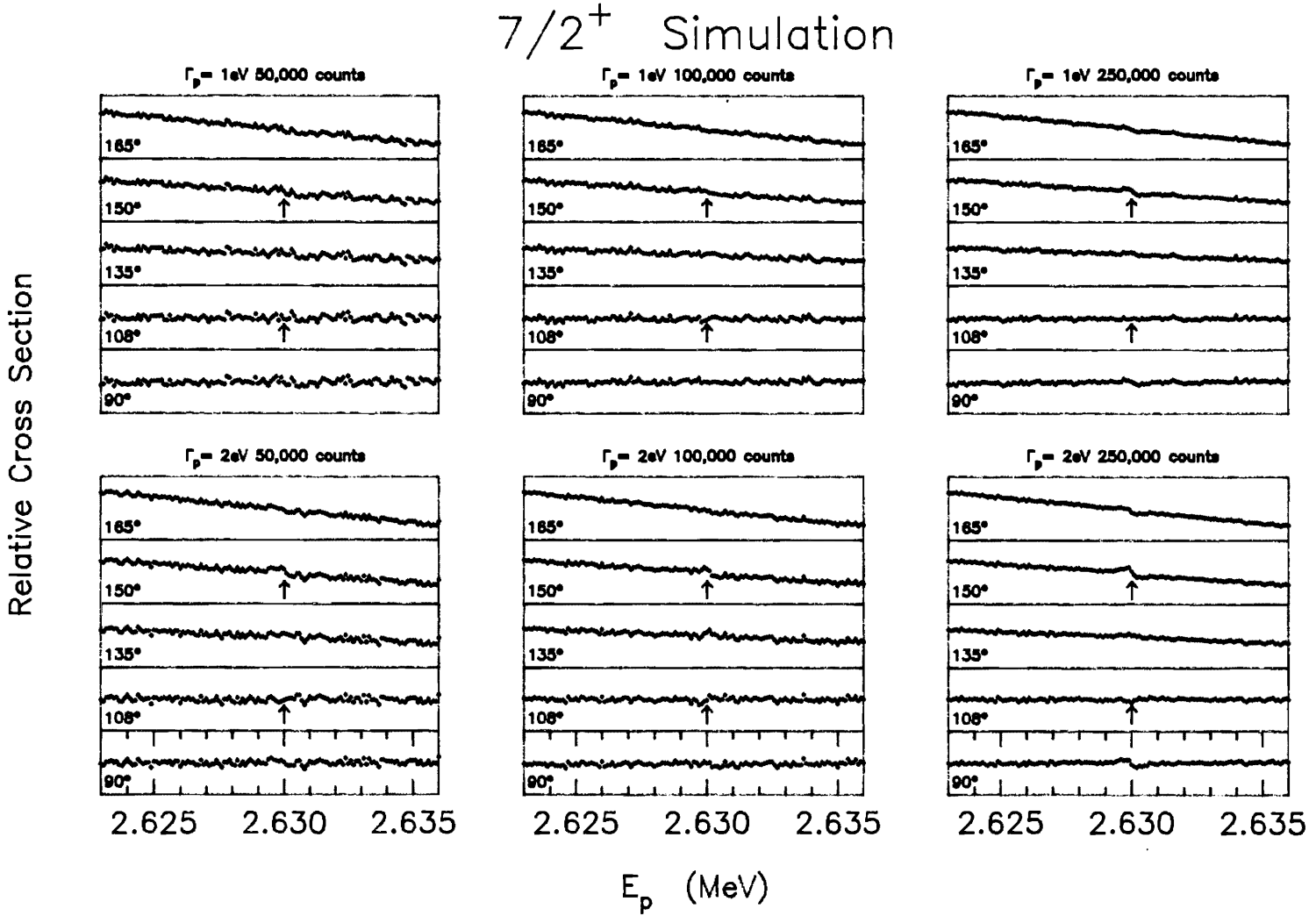
7/2+ Simulation
Γp= 1eV 50,000 counts
Γp= 1eV 100,000 counts
Γp= 1eV 250,000 counts
Γp= 2eV 50,000 counts
Γp= 2eV 100,000 counts
Γp= 2eV 250,000 counts
165°
150°
135°
108°
90°
Relative Cross Section
2.625
2.630
2.635
Ep (MeV)

counts were obtained and then only in the 165° and the 150° yield curves. However, the 2 eV resonance becomes observable at 100,000 counts in the 150°, 135°, and 108° yield curves. The simulation was useful in estimating the amount of beam necessary to observe the resonance if its width were one of these values. These simulations were performed for a resolution of 350 eV.

Figure 5.11 shows the gamma-ray yield for $E_p$=2.629 to 2.631 MeV. The resonance is easily seen in the capture channel. Figures 5.12 and 5.13 show the $^{28}$Si(p,p) and $^{28}$Si(p,p') yields and the corresponding multilevel fit with $J^{\pi}=7/2^{+}$. An elastic width of 2 eV and an inelastic width of 10 eV have been assumed. For this fit the 150°, 135°,and 108° curves match very well. However, for the 165° and 90° yield curves the simulation shows that the resonance is probably buried in the point scatter. The best fit to the $^{28}$Si(p,p') data was obtained using $\Gamma_p$,(s'=3/2, $\ell$=2)=10 eV. An upper limit may be placed on the elastic width of 2 eV.

D. Unobserved Resonance at 1.916 MeV

A search for this resonance was performed with the (p,$\gamma$) reaction. No sign of this resonance was observed. This resonance was reported by Byrski [By74] using a GeLi gamma-ray detector. No other indication of this resonance has been reported.

Figure 5.11 Gamma-ray Yield Curve near $E_p$=2.630 MeV.

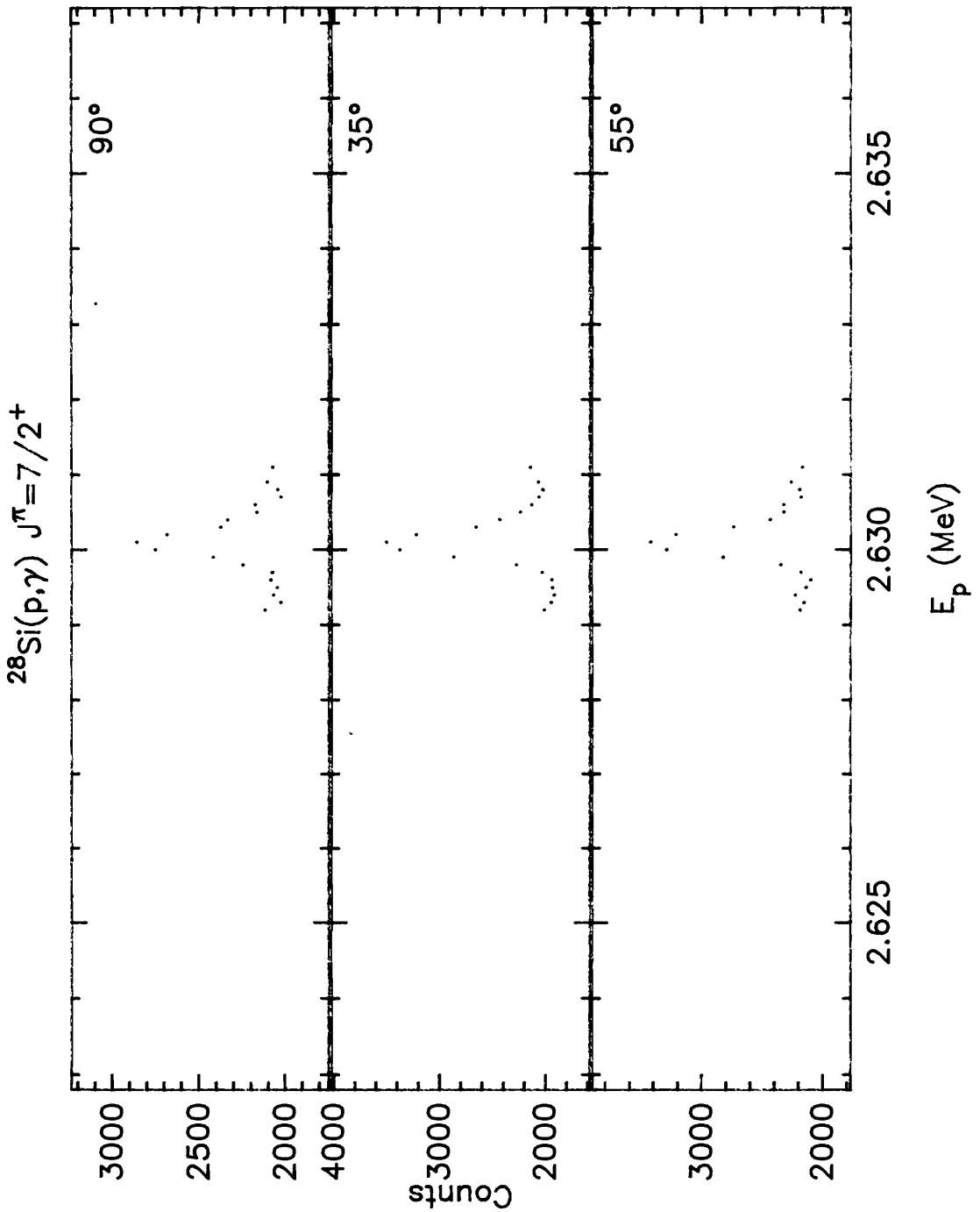
$^{28}Si(p,\gamma)$ $J^{\pi}=7/2^{+}$
90°
35°
55°
Counts
3000
2500
2000
4000
3000
2000
3000
2000
2.625
2.630
2.635
$E_p$ (MeV)

Figure 5.12 Multilevel Fit to the $^{28}$Si(p,p) Data near $E_p$=2.630 MeV, with $J^{\pi}=7/2^{+}$ and $\Gamma_p$=2 eV.

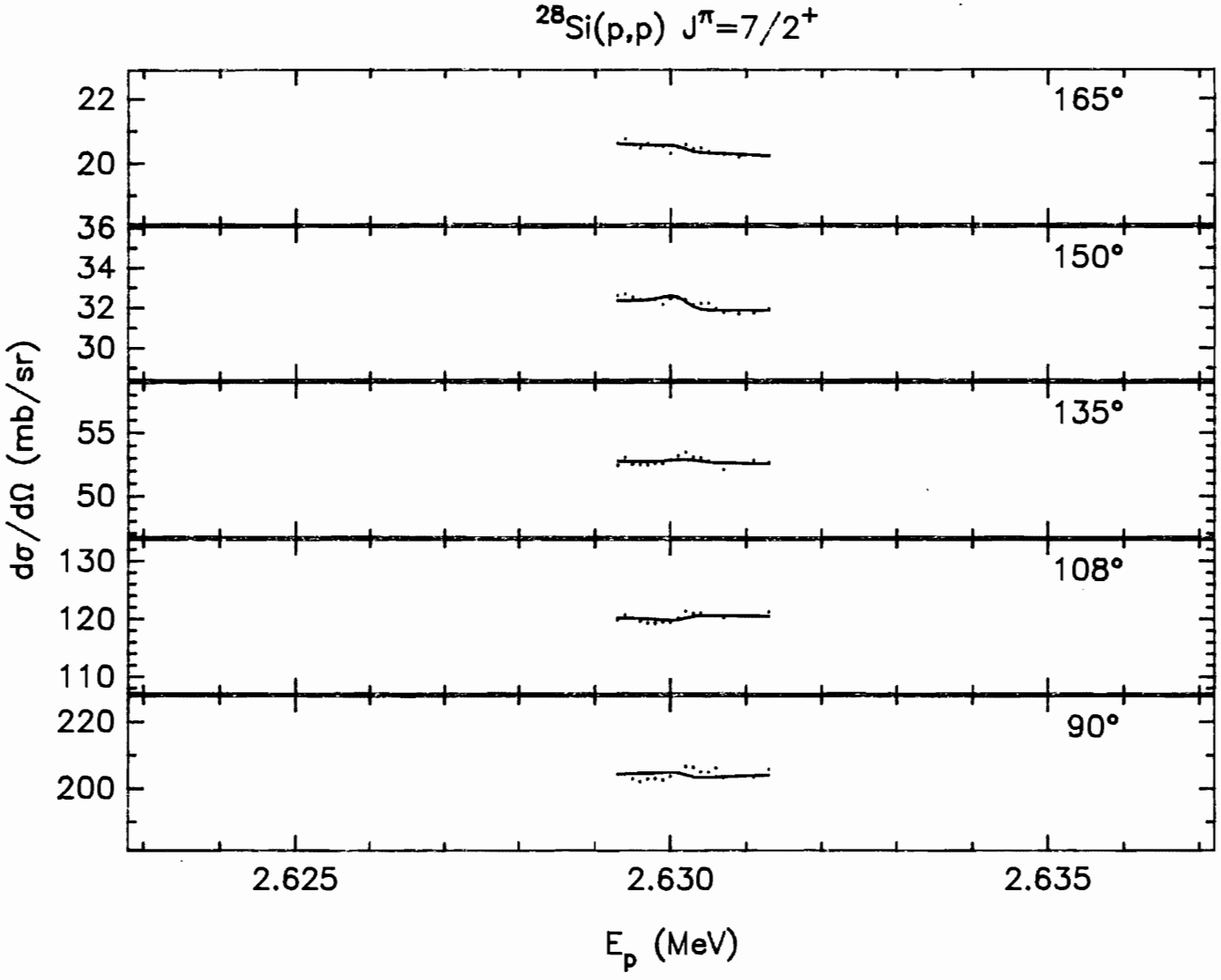
$^{28}$Si(p,p) $J^{\pi}=7/2^{+}$
165°
150°
135°
108°
90°
22
20
36
34
32
30
55
50
130
120
110
220
200
dσ/dΩ (mb/sr)
2.625
2.630
2.635
$E_p$ (MeV)

Figure 5.13 Multilevel Fit to the $^{28}Si(p,p')$ Data near $E_p$=2.630 MeV, with $J^{\pi}=7/2^+$ and $\Gamma_{p'}$=10 eV.

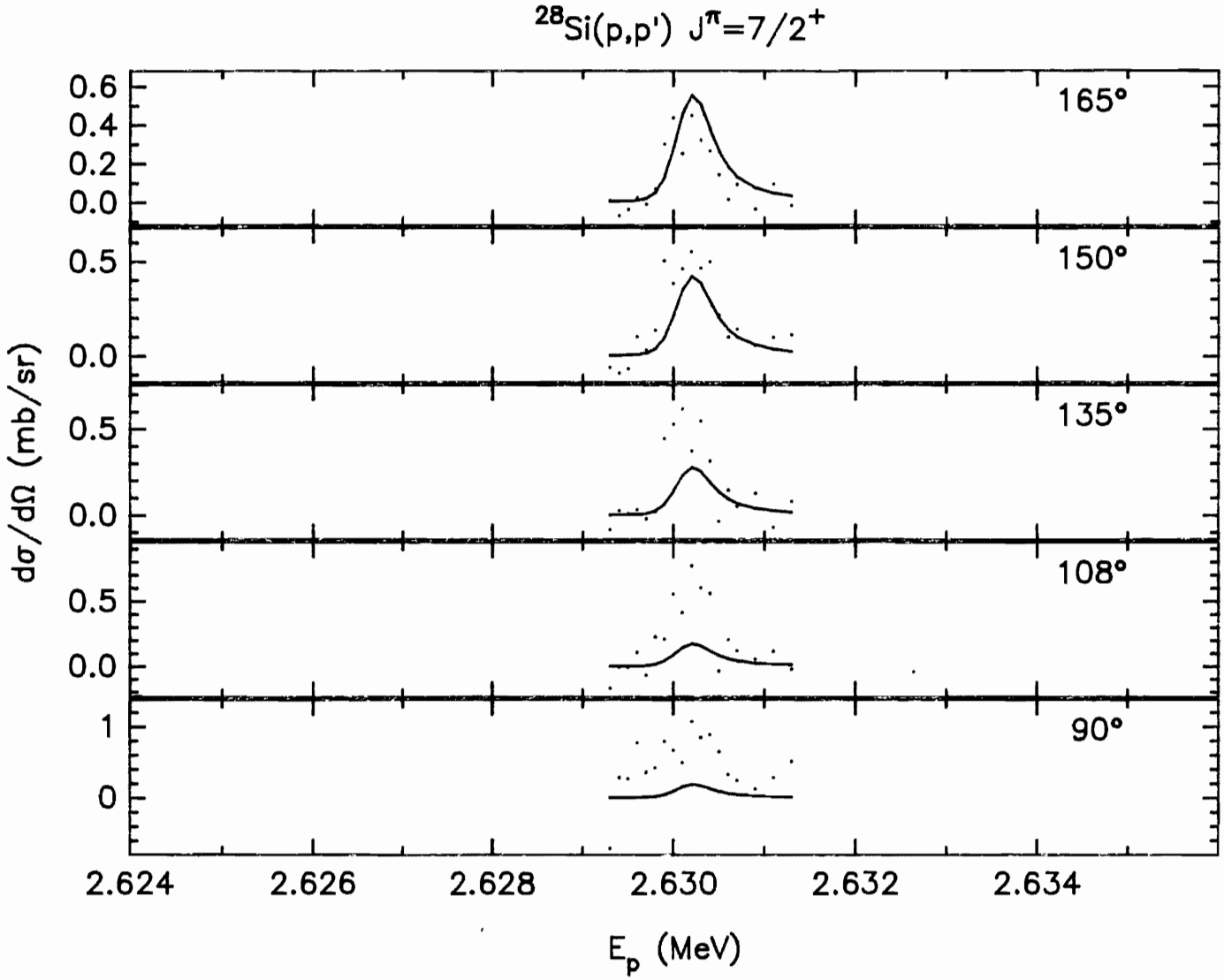
$^{28}$Si(p,p') $J^{\pi}=7/2^{+}$
165°
150°
135°
108°
90°
dσ/dΩ (mb/sr)
0.6
0.4
0.2
0.0
0.5
0.0
0.5
0.0
0.5
0.0
1
0
2.624
2.626
2.628
2.630
2.632
2.634
$E_p$ (MeV)

# CHAPTER IV

# ANALOG STATES

## A. Background

If nuclear forces are charge independent (or approximately so), then corresponding states of different nuclei with the same mass are essentially identical. The members of an isobaric multiplet have common isospin T and are distinguished by their isospin projections $T_3$. The states with $T_3$=T are called "parent" states. The corresponding states in the multiplet with $T_3$=T-1 are called "daughter" states. For proton scattering from a target nucleus of isospin $T_i$, states with $T_i \pm 1/2$ are allowed. The analog states have isospin $T_i$+1/2.

For charge independent forces the energy of the daughter state differs from that of the parent state only due to Coulomb effects. This energy difference is the Coulomb energy of the proton in the daughter minus the neutron-proton mass difference. A diagram of the relationship between these states is shown in figure 6.1. The Coulomb energy difference is

$$\Delta E = B_n + E_p^{cm} - E_x \qquad 6.1$$

$B_n$ is the binding energy of the last neutron in the parent nucleus, $E_p^{cm}$ is the resonance energy in the center-of-mass system, and $E_x$ is the excitation of the parent state in the parent nucleus.

Figure 6.1 Schematic Level Diagram showing Energy Relations between the Parent State and the Analog Resonance.

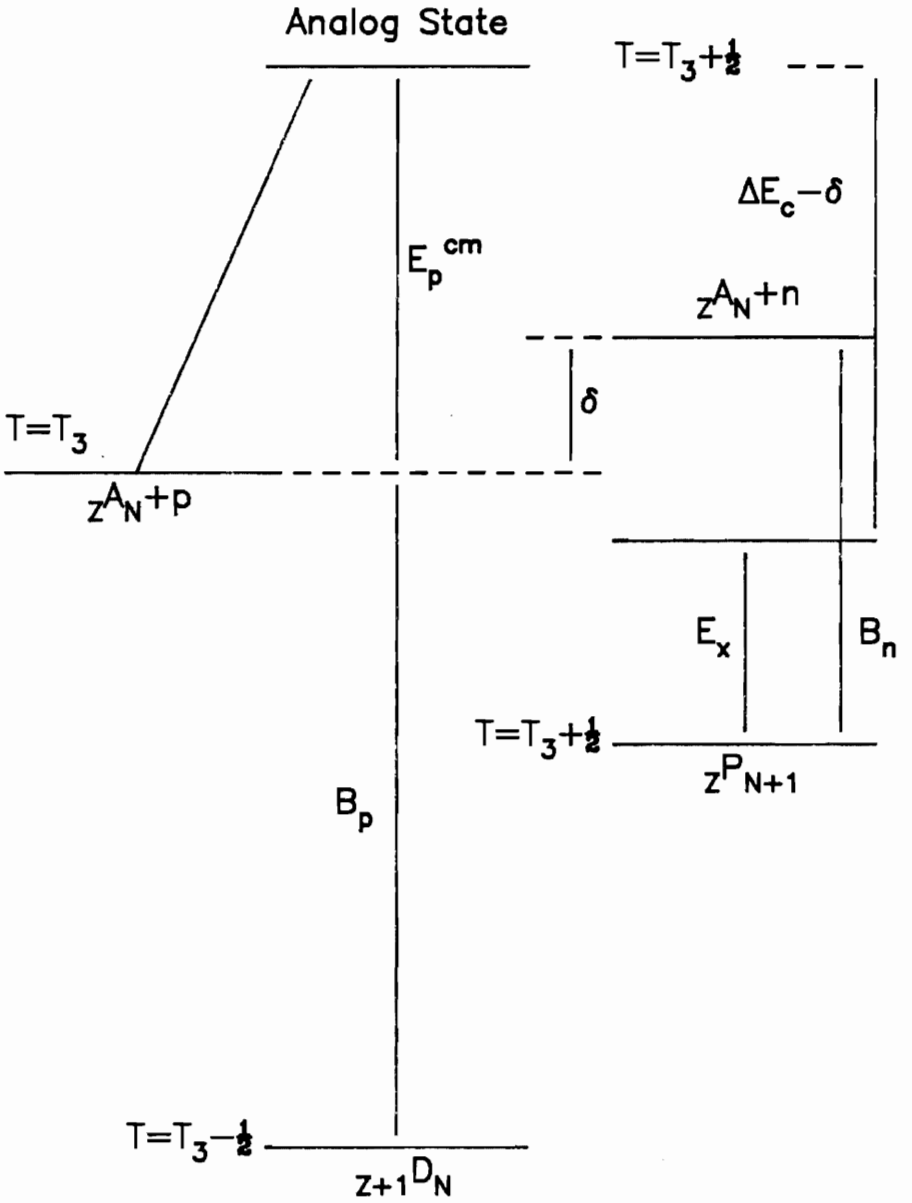
Analog State
$T=T_3+\frac{1}{2}$
$\Delta E_c-\delta$
$E_p^{cm}$
$_ZA_N+n$
$\delta$
$T=T_3$
$_ZA_N+p$
$E_x$
$B_n$
$T=T_3+\frac{1}{2}$
$_ZP_{N+1}$
$B_p$
$T=T_3-\frac{1}{2}$
$_{Z+1}D_N$

To identify analog states, one must know the excitation energies, spins, parities, and spectroscopic factors of the states in the parent nucleus. This information is generally obtained through neutron stripping reactions such as the (d,p) reaction. Information on daughter states can be obtained through proton transfer reactions such as the ($^3$He,d) reaction or through resonances in proton elastic scattering.

Strengths of the parent and analog states are expected to obey the relation

$$S_p = (2T_i + 1)\frac{\Gamma_p}{\Gamma_{sp}} = S_{dp} \qquad 6.2$$

Where $S_p$ is the proton spectroscopic factor, $\Gamma_{sp}$ is the single particle width of the resonance, and $S_{dp}$ is the (d,p) spectroscopic factor. The target isospin is $T_i$.

Proton single particle widths are estimated following Zaidi and Darmodjo [Za67], and Harney [Ha68]. The (ZDH) method is discussed in detail by Harney and Weidenmuller [Ha69]. A Woods-Saxon shape is assumed, and the potential depth for the neutron is varied to obtain the proper excitation energy in the parent. A symmetry potential

$$U_{sym} = \frac{1}{2}(2T_0 + 1)\frac{125}{A} \quad \text{MeV} \qquad 6.3$$

is added to the neutron well depth to simulate the proton potential. The single particle proton width is obtained with these potential well parameters. The variation in single particle widths due to uncertainties in the optical model parameters is estimated to be about 15% by Moses [Mo69].

B. Spectroscopic Factors

Table 6.1 lists the experimental values for the spectroscopic factors for $^{29}$P and $^{29}$Si. The 4.080 MeV resonance in $^{29}$P has been considered the analog of the $E_x$=4.080 MeV bound state in $^{29}$Si. The single particle width calculation indicated a width of $\Gamma_p$= 1.9 eV. McCulloch [Mc84] and Dhuga [Dh86] determined the spectroscopic factor to be 0.06 and 0.04, respectively. This would correspond to a width for the $^{29}$P resonance on the order of meV.

It is clear that the $J^\pi=3/2^-$, $E_x$=4.934 MeV state in $^{29}$Si is the parent of the $J^\pi=3/2^-$, $E_x$=4.343 MeV state in $^{29}$P. The spectroscopic factor obtained in this experiment of 0.48 agrees with that obtained previously. The average spectroscopic factor from Table 6.1 is 0.38±0.09 for the analog state and 0.59±0.15 for the parent state. The $J^\pi=1/2^+$, $E_x$= 4.839 MeV bound state in $^{29}$Si is the parent state of the $J^\pi=1/2^+$, $E_x$= 4.759 MeV resonance in $^{29}$P. The spectroscopic factors agree. The average spectroscopic factor for the parent state in $^{29}$Si is 0.07±0.05 and the spectroscopic factor for the analog state in $^{29}$P is 0.03±0.008. The spectroscopic factor obtained in this experiment is 0.04.

The $J^\pi=5/2^+$, $E_x$= 4.895 state in $^{29}$Si indicates a spectroscopic factor for this state around 1.0. All these values were the result of pickup reactions except for Karban [Ka80] who used neutron stripping from $^3$He and assigned a spectroscopic factor of 0.50. Endt [En78] does not assign a spectroscopic factor $S_n^+$ to this level. The previous assignment for the analog of this state had been the $J^\pi= 5/2^+$, $E_x$= 4.945 MeV resonance. This assignment no longer appears reasonable because of the small spectroscopic factor determined in this experiment of 0.004.

TABLE 6.1

Summary of Experimental Spectroscopic Factors

| $^{29}$P | | | | | | | | | | |
|---|---|---|---|---|---|---|---|---|---|---|
| $E_x$(MeV) | | 4.080 | 4.340 | 4.761 | 4.955 | 5.288 | 5.544 | 5.743 | 5.972 | 6.188 | 6.332 |
| | $J^\pi$ | $7/2^+$ | $3/2^-$ | $1/2^+$ | $5/2^+$ | $7/2^+$ | $1/2^-$ | $7/2^-$ | $3/2^+$ | $3/2^-$ | $3/2^+$ |
| Present Work | $S_p$ | | 0.48 | 0.04 | 0.004 | 0.009 | 0.29 | 0.11 | 0.07 | | 0.02 |
| Dy76 | $^{28}$Si(τ,d) | 0.02 | 0.43 | 0.03 | | | | 0.16 | 0.05 | | 0.04 |
| Le74 | $^{28}$Si(τ,d) | | 0.28 | 0.02 | | | | 0.19 | 0.02 | | 0.02 |
| Ka77 | $^{28}$Si(τ,d) | | 0.33 | | | | | 0.15 | 0.04 | | 0.03 |
| Pe75 | $^{28}$Si(τ,d) | <0.005 | | | | | | | | | |
| $^{29}$Si | | | | | | | | | | | |
| $E_x$ | | 4.080 | 4.934 | 4.839 | 4.895 | 5.285 | 6.381 | 6.191 | 5.949 | | |
| | $J^\pi$ | $7/2^+$ | $3/2^-$ | $1/2^+$ | $5/2^+$ | $7/2^+$ | $1/2^-$ | $7/2^-$ | $3/2^+$ | | $3/2^+$ |
| Pe83 | $^{28}$Si(d,p) | | 0.41 | 0.04 | | | 0.36 | 0.07 | 0.34 | | |
| El72 | $^{28}$Si(d,p) | | 0.55 | 0.02 | | | 0.55 | 0.15 | 0.05 | | |
| Me71 | $^{28}$Si(d,p) | | 0.55 | | | | 0.50 | 0.34 | 0.14 | | |
| Be66 | $^{28}$Si(d,p) | | 0.60 | 0.06 | | | | | | | |
| Ha75 | $^{30}$Si(p,d) | | | 0.14 | 0.92 | | | | | | 0.10 |
| De70 | $^{30}$Si(p,d) | | | 0.10 | 1.0 | | | 0.02 | | | 0.20 |
| Pe70 | $^{30}$Si(p,d) | | | | 1.19 | | | | | | |
| De67 | $^{30}$Si(p,d) | | | | 1.0 | | 0.26 | 0.28 | 0.07 | | |
| Dr80 | $^{28}$Si($^3$He,$^2$He) | | 0.86 | | | | 0.65 | 0.19 | | | |

Table 6.1 cont

| $^{29}$Si | | | | | | | | | | |
|---|---|---|---|---|---|---|---|---|---|---|
| $E_x$(MeV) | | 4.080 | 4.934 | 4.839 | 4.895 | 5.285 | 6.381 | 6.191 | 5.949 | |
| | $J^\pi$ | $7/2^+$ | $3/2^-$ | $1/2^+$ | $5/2^+$ | $7/2^+$ | $1/2^-$ | $7/2^-$ | $3/2^+$ | $3/2^+$ |
| Ka80 | $^{28}$Si($^3$He,pp) | | | | 0.50 | | 0.65 | 0.19 | | |
| Mc84 | $^{28}$Si($^3\vec{\text{He}}$,$^4$He) | 0.06 | | | 0.83 | | | | | |
| Dh86 | $^{27}$Al($^6$Li,$\alpha$) | 0.037 | | | | | | | | |
| Ec84 | $^{28}$Si($^7$Li,$^6$Li) | | | | | | 0.31 | 0.11 | | |
| Fe86 | $^{28}$Si($^{18}$O,$^{17}$O) | | 0.67 | | | | | | | |
| Tr86 | $^{28}$Si($^{28}$Si,$^{27}$Si) | | 0.57 | | | | | | | |

The $J^{\pi}=1/2^{-}$, $E_x=6.381$ MeV state in $^{29}Si$ is assigned the parent of the $J^{\pi}=1/2^{-}$, $E_x=5.527$ MeV resonance in $^{29}P$. The present spectroscopic factor is 0.29, which compares with an average over previous results for the parent level of 0.49±0.14.

The $J^{\pi}=7/2^{-}$, $E_x=6.191$ MeV state in $^{29}Si$ is the parent state of the $J^{\pi}=7/2^{-}$, $E_x=5.739$ MeV state in $^{29}P$. The present spectroscopic factor is 0.11, compared with an average of 0.17±0.1 from previous results. For the parent state the average spectroscopic factor is 0.16±0.10.

The $J^{\pi}=3/2^{+}$, $E_x=5.949$ MeV state in $^{29}Si$ is the parent state of the $J^{\pi}=3/2^{+}$, $E_x=5.972$ MeV resonance in $^{29}P$. The average spectroscopic factor for the parent state is 0.08±0.05 excluding one anomalous value [Pe83], and the spectroscopic factor for the analog is 0.07 which compares with an average over previous results of 0.036±0.2.

No parent state assignment has been made for the $J^{\pi}=3/2$, $E_x=6.191$ MeV state and the $J^{\pi}=3/2^{+}$, $E_x=6.328$ MeV resonance in $^{29}P$. If the $3/2^{+}$ parent state is assumed to be the $J^{\pi}=3/2^{+}$, $E_x=7.190$ MeV state, then the spectroscopic factor for the $J^{\pi}=3/2^{+}$, $E_x=6.328$ MeV resonance in $^{29}P$ is 0.02 with an average of 0.027±0.01 and the average parent state spectroscopic factor is 0.15±.07. However such a large shift for these weak states seems unlikely.

C. Thomas-Ehrman Shifts

If the daughter states were all shifted by the ground state Coulomb displacement energy $\Delta E$ locating analog states would be a simple matter. It would be expected that the spectrum of the daughter would closely resemble the parent. This is not the case. The

relative level spacings may differ by a large amount. Reasons for this shifting was partially explained by Thomas [Th52] and Ehrman [Er51].

Extreme examples of this shifting are apparent in figure 6.2. The $E_x$=4.8390, $J^\pi=1/2^+$ and the $E_x$=4.9336, $J^\pi=3/2^-$ state in $^{29}$Si are assigned as the parents of the $E_x$=4.7590, $J^\pi=1/2^+$ and the $E_x$=4.3430, $J^\pi=3/2^-$ states in $^{29}$P. In going from $^{29}$Si to $^{29}$P the crossing of the energy levels indicates that there is some effect other than the Coulomb displacement. This crossing also occurs going from the $E_x$=5.9490, $J^\pi=3/2^+$ and the $E_x$=6.3870, $J^\pi=1/2^-$ states in $^{29}$Si to the daughter states in $^{29}$P.

In equation 2.6 the actual energy of the resonance is shifted by an amount $\Delta_\lambda$ given by the equation below.

$$\Delta_\lambda = \sum_{c\pm} \gamma_{\lambda c}^2 \left( S_c^\lambda(\rho) - B_c \right) \qquad 6.4$$

The summation is over all open and closed channels as indicated by c±. $S_c^\lambda(\rho)$ is the function defined by equation 2.34.

The parent states are bound and therefore correspond to closed channels. Assuming that the bound states in the parent may be represented by R-Matrix like states there would also be a shifting of the levels in the parent. Explicitly the shift function for the neutron wave function (closed channels) and Coulomb wave function (open channels) is given in 6.5a and 6.5b, respectively.

$$S_{nc-}^\lambda(\rho) = \frac{W'_{0,\ell+1/2}(2\rho_\alpha)}{W_{0,\ell+1/2}(2\rho_\alpha)} = \frac{\frac{d}{d\rho_\alpha}\left( \frac{2\rho_\alpha}{\pi}\sqrt{\frac{\pi}{2\rho_\alpha}} K_{\ell+1/2}(\rho_\alpha) \right)}{\frac{2\rho_\alpha}{\pi}\sqrt{\frac{\pi}{2\rho_\alpha}} K_{\ell+1/2}(\rho_\alpha)} \qquad 6.5a$$

Figure 6.2 Diagram of the Mirror Pair $^{29}$Si and $^{29}$P.

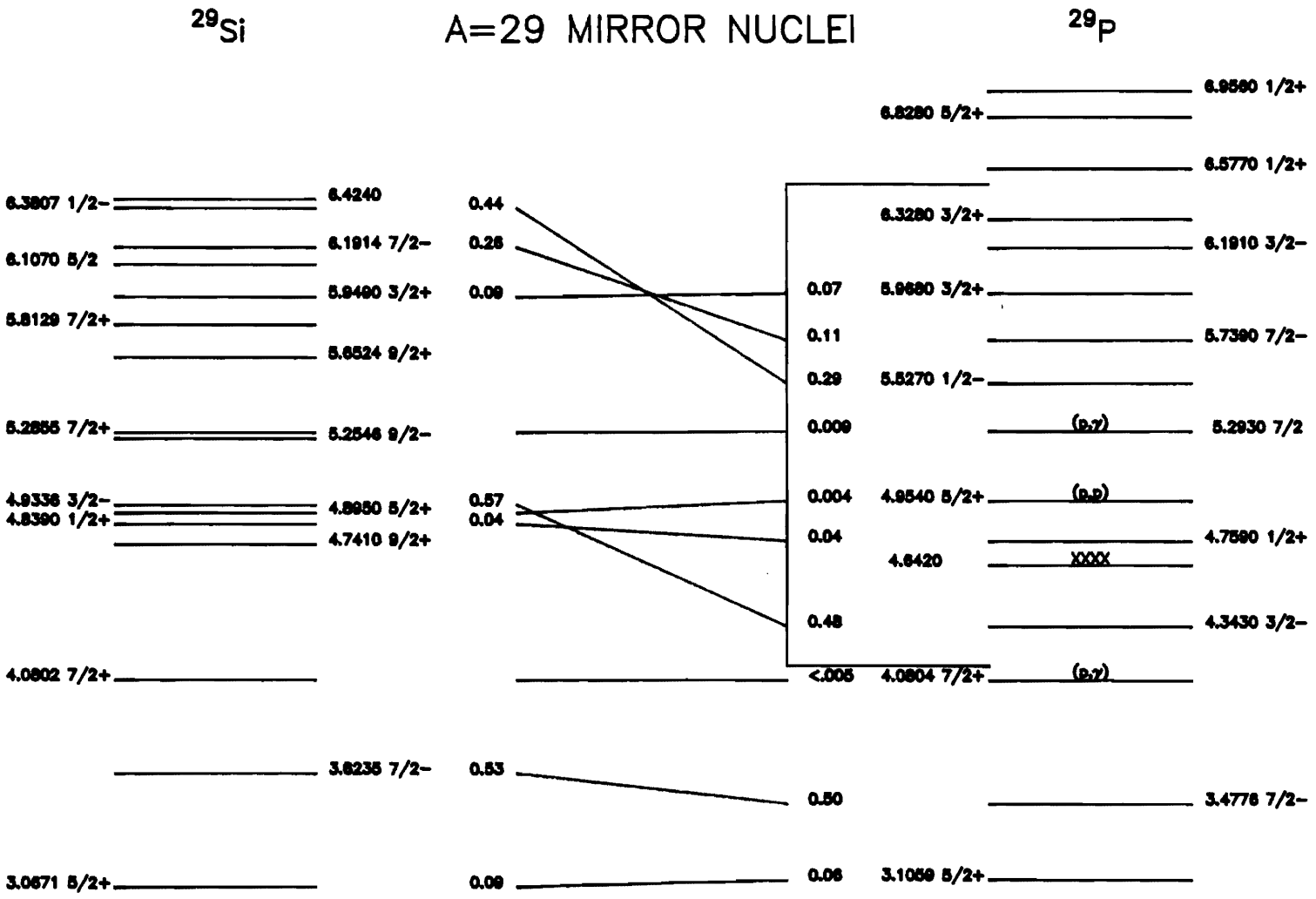
29Si
A=29 MIRROR NUCLEI
29P
6.3807 1/2−
6.4240
6.1914 7/2−
6.1070 5/2
5.9490 3/2+
5.8129 7/2+
5.6524 9/2+
5.2855 7/2+
5.2548 9/2−
4.9338 3/2−
4.8390 1/2+
4.8950 5/2+
4.7410 9/2+
4.0802 7/2+
3.6235 7/2−
3.0671 5/2+
0.44
0.26
0.09
0.57
0.04
0.53
0.09
0.07
0.11
0.29
0.009
0.004
0.04
0.48
<.005
0.50
0.06
6.9560 1/2+
6.8280 5/2+
6.5770 1/2+
6.3280 3/2+
6.1910 3/2−
5.9680 3/2+
5.7390 7/2−
5.5270 1/2−
(p,γ)
5.2930 7/2
4.9540 5/2+
(p,p)
4.7590 1/2+
4.6420
XXXX
4.3430 3/2−
4.0804 7/2+
(p,γ)
3.4778 7/2−
3.1059 5/2+

$$S^{\lambda}_{pc+}(\rho_\alpha) = \frac{F'_\ell(\rho_\alpha)G_\ell(\rho_\alpha) + F_\ell(\rho_\alpha)G'_\ell(\rho_\alpha)}{F_\ell(\rho_\alpha)^2 + G_\ell(\rho_\alpha)^2} \qquad 6.5b$$

Where $W_{\ell+1/2}(2\rho_\alpha)$ is the Whittaker function and $K_{\ell+1/2}(\rho_\alpha)$ is the modified spherical Bessel function of the third kind.

The important quantity is the relative shift. The wavefunctions for the states are assumed equal in the internal region so that the boundary condition of the neutron in a particular channel ($B_{nc}$) and the boundary condition of the proton ($B_{pc}$) in the same channel are assumed equal. This leads to an equation for the relative shift.

$$\Delta_{\lambda n} - \Delta_{\lambda p} = \sum_{c\pm} \gamma^2_{\lambda c}\left[S^{\lambda}_{pc}(\rho^{\lambda}_p) - S^{\lambda}_{nc}(\rho^{\lambda}_n)\right] = \Delta^{\lambda}_{np} \qquad 6.6$$

This is the Thomas-Ehrman shift. The shift results because the Coulomb interaction makes the wave functions in the external region unequal. The amount by which the neutron and proton wave functions differ determines the magnitude of the shift. For example, a large shift is expected between a bound single particle neutron state and an unbound single particle proton state. Each analog state is shifted dirrerently relative to its corresponding parent state and the spectra of the two systems can be quite different.

The energies of the daughter states are shifted higher due to the coulomb interaction and other higher order interactions denoted by $\langle V_\tau \rangle$. Subtracting this energy from the states in the daughter will line up the ground states. If there were no other mechanism for shifting the levels then the spectra should be essentially identical. However, the total shift will be due to the potential displacement and the Thomas-Ehrman shift as

given in equation 6.5 below.

$$E_n - E_p = -\langle V_\tau \rangle + (\Delta_{\lambda n} - \Delta_{\lambda p}) \qquad 6.7$$

Table 6.2 lists the excitation energies of the parent and daughter states, the shift defined by equation 6.6, the reduced width, and the shift in energy. The $J^\pi=5/2^+$, $E_x$=4.8950 MeV level in $^{29}$Si and the $E_x$=4.9540 MeV level in $^{29}$P have previously been assigned as mirror levels. However, the spectroscopic factors contradict this assignment. Figure 6.3 shows the parent nuclear spectrum and the corrected daughter nuclear spectrum.

Table 6.2

Thomas-Ehrman Shifts

| $E_{rn}$ (MeV) | $E_{rp}$ (MeV) | $S_{nc}^{\lambda}(\rho_\alpha) - S_{pc}^{\lambda}(\rho_\alpha)$ | $\gamma_c^2$ (keV) | $\Delta_{pn}$ (keV) |
|---|---|---|---|---|
| 4.080 | 4.080 | -.32 | 225 | -71 |
| 4.934 | 4.343 | -.77 | 769 | -592 |
| 4.839 | 4.761 | -.84 | 34 | -29 |
| 6.381 | 5.544 | -.87 | 857 | -745 |
| 6.191 | 5.743 | -.61 | 129 | -79 |
| | | -.71 | 592 | -420[1] |
| 5.949 | 5.972 | -.84 | 40 | -34 |
| | | -.62 | 16 | -10[1] |

1. Denotes inelastic channel included

Figure 6.3 Diagram of $^{29}$Si and $^{29}$P Mirror Pair with the Daughter States corrected According to the Thomas-Ehrman shift.

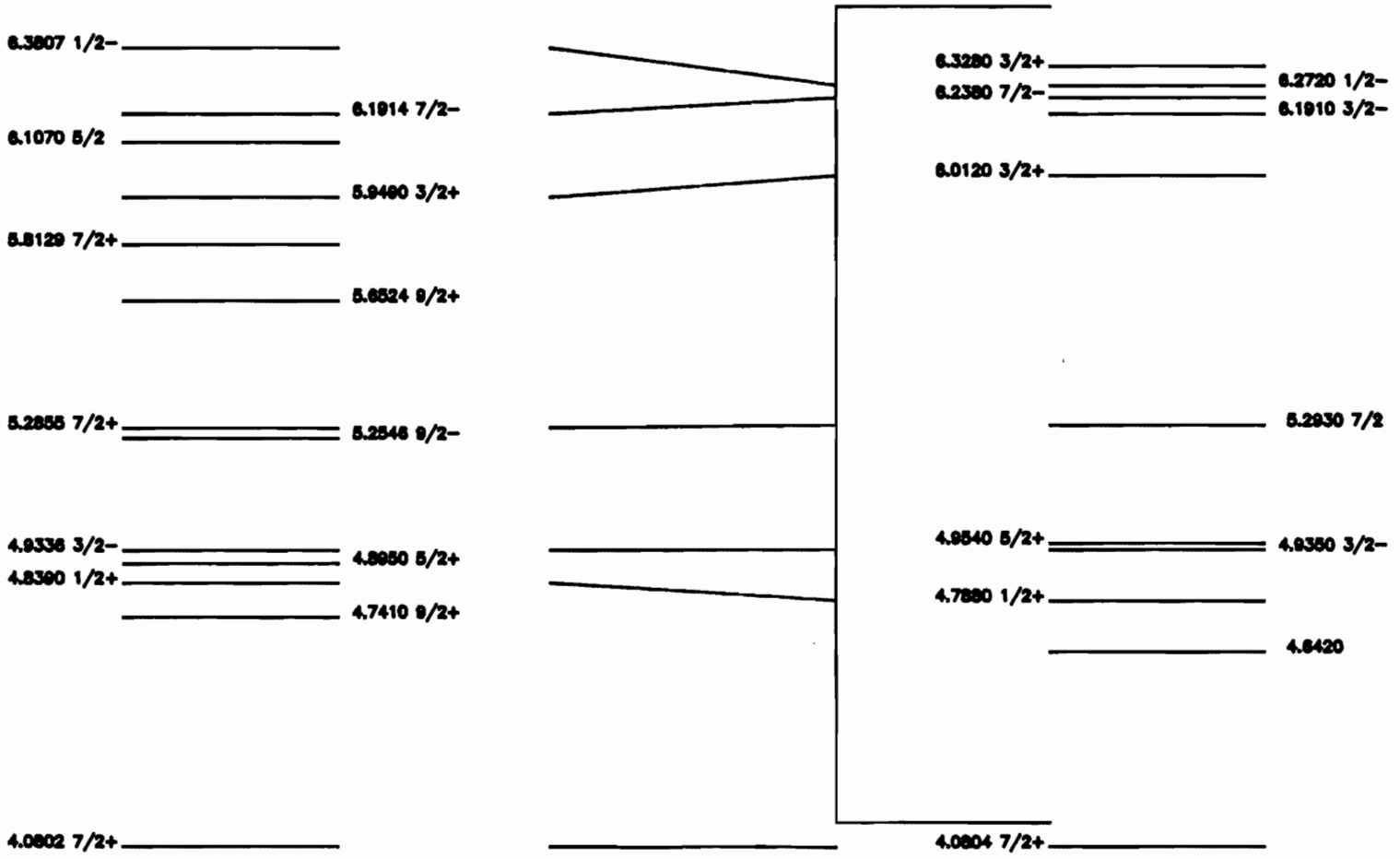
$^{29}$Si CORRECTED A=29 MIRROR NUCLEI $^{29}$P
6.3807 1/2−
6.1914 7/2−
6.1070 5/2
5.9490 3/2+
5.8129 7/2+
5.6524 9/2+
5.2855 7/2+
5.2546 9/2−
4.9336 3/2−
4.8950 5/2+
4.8390 1/2+
4.7410 9/2+
4.0802 7/2+
6.3280 3/2+
6.2720 1/2−
6.2380 7/2−
6.1910 3/2−
6.0120 3/2+
5.2930 7/2
4.9540 5/2+
4.9350 3/2−
4.7880 1/2+
4.6420
4.0804 7/2+

# CHAPTER VI

## SUMMARY

Excitation functions were measured for proton elastic and inelastic scattering on $^{28}$Si. R-Matrix parameters (spins, parities, partial and total widths, and resonance energies) were extracted for 8 levels. Emphasis was placed on determining the properties of levels which had previously only been observed via the capture reaction. For one of these states ($J^{\pi}=5/2^{+}$, $E_x=4.95$ MeV) the elastic scattering data yielded a strong resonance ($\Gamma_p \approx 80$ eV). This demonstrated the advantage of the improved energy resolution.

A gamma-ray yield was taken to locate the small $J^{\pi}=7/2^{+}$ resonances near $E_x=4.080$ MeV and $E_x=5.290$ MeV. Both resonances were located in the gamma-ray yield. An extremely high count excitation curve was measured for proton elastic scattering after the resonance had been located in the gamma-ray yield. For the resonance at $E_x=5.290$ MeV an inelastic excitation curve was also measured. Estimates of the upper limits for the elastic widths for both resonances were set at less than 2 eV, which significantly improved earlier estimates. The latter resonance is clearly observed in the (p,p') excitation curve and has an inelastic width of $\Gamma_{p'}=16$ eV.

The $J^{\pi}=7/2^{-}$ resonance near $E_x=5.740$ MeV had been assigned $J^{\pi}=5/2^{-}$ from the analysis of previous proton elastic and inelastic scattering excitation curves. Prior analyses used a single level approximation; in this region such an approximation is not valid. Detailed calculations indicate that interference with a neighboring level has a significant effect on the resonance shape. The previous $J^{\pi}=5/2^{-}$ assignment is definitely rejected. By chance no previous experiment measured the proton elastic excitation function at

135°, which would have established that the resonance did not have J=5/2. These results indicate that multilevel effects are important even for nuclei with only a few wide levels.

Most of the resonances in $^{29}$P have been identified as mirror states and the spectroscopic factors for the daughter and parent states are in reasonable agreement. However, the $J^{\pi}=5/2^{+}$, $E_x$=4.895 MeV state in $^{29}$Si and the $J^{\pi}=5/2^{+}$, $E_x$=4.954 MeV level in $^{29}$P have previously been assigned as mirror levels. The average spectroscopic factor from pickup reactions assigned to the parent level is approximately 1.0. The spectroscopic factor calculated for the daughter state in $^{29}$P is 0.004. The large discrepancy indicates the assignment of the levels as mirror levels is very doubtful.

For a few of the resonance states no parent states can be uniquely assigned. The relative shifts in the level ordering for the mirror pairs can be explained by the Thomas-Ehrman shifts, which are quite large for some of these (very strong) states.

The experimentally determined spectroscopic factor for the $J^{\pi}=3/2^{+}$, $E_x$=5.968 MeV level in $^{29}$P is 0.07 in agreement with ($\tau$,d) results. It is designated the daughter of the $J^{\pi}=3/2^{+}$, $E_x$=5.968 MeV level in $^{29}$P.

No parent levels can be conclusively assigned to the $J^{\pi}=3/2^{-}$, $E_x$=6.191 MeV and the $J^{\pi}=3/2^{+}$, $E_x$=6.328 MeV levels in $^{29}$P. More information is needed on the spectroscopic factors of the higher energy levels as well as more conclusive determinations of the spin and parity of these levels in $^{29}$Si before a definitive comparison of the mirror pair $^{29}$Si-$^{29}$P can performed.

Based on the present results it appears that even for a well studied nucleus with only a few, mostly broad levels, that the experimental advantages of very good energy resolution and the advantages of multilevel analysis, can lead to significant improvements in the spectroscopy of light nuclei.

# REFERENCES

Ab72 Abramowitz,M., and Stegun, I.A., Handbook of Mathematical Functions, Dover Publications Inc., New York (1972)

Be61 Belote,T.A., Kashy,E., and Risser,J.R., Phys. Rev. **122**, 920 (1961)

Bi52 Biedenharn,L.C., Blatt,J.M., and Rose,M.E., Rev. Mod. Phys. **24**, 249 (1952)

Bo36 Bohr,N., Nat. **137**, 134 (1936)

Bo67 Bommangh,C.H., Meyer,M.A., and Rietman,D., Nucl. Phys. A **99**, 337 (1967)

By74 Byrski,T., Beck,F.A., Engelstein,P., Forterre,N., and Knipper,A., Nucl. Phys. A **223**, 125 (1974)

Co51 Condon,E.U. and Shortley,G.H., The Theory of Atomic Spectra, Cambridge University Press, Cambridge (1951)

Co80 Condon,E.U. and Odabasi,H., Atomic Structure, Cambridge University Press, Cambridge (1980)

Dh86 Dhuga,K.S., Fortune,H.R., Burlein,M., Carchidi,M., Dwyer,M., Gilfoyle,G., and Sweet,J.W., Phys. Rev. C **33**, 1294 (1986)

Dj82 Djaloeis,A., Gopal,S., Bojowald,J., Oelert,W., Tured,P., and Mayer-Boricke,C., Phys. Rev. C **28**, 561 (1982)

Dr80 Van Driel,J., Kamermans,R., De Meijer,R.J., and Dieperink,A.E.L., Nucl. Phys. A **342**, 1 (1980)

Dy76 Dykoski,W.W. and Dehnhard,D., Phys. Rev. C **13**, 80 (1976)

Ec84 Eck,J.S., Kemper,K.W., and Ophel,T.R., Nucl. Phys. A **425**, 141 (1984)

Eh51 Ehrman,J.B., Phys. Rev. **81**, 412 (1951)

En78 Endt,P.M. and Van der Leun,C., Nucl. Phys. A **310**, 1 (1978)

Eg88 Egun,P.M., Brient,C.E., Grimes,S.M., Saraf,S.K., and Satyanarayana,H., Phys. Rev. C **38**, 2495 (1988)

Ej64 Ejiri,H., Ohmura,H., Nakajima,Y., Horie,K., Hashimoto,Y., Eto,K., Matsumoto,S., Nogami,Y., Nucl. Phys. **52**, 561 (1961)

Fe86 Fernandes,M.A.G., Burks,B.L., Horen,D.J., Satchler,G.R., Auble,R.L., Bertrand,F.E., Blankenship,J.L., Ford,J.L.C.,jr., Gross,E.E., Hensley,D.C., Sayer,R.O., Shapira,D. and Sjoreen,T.P., Phys. Rev. C **33**, 1971 (1986)

Ge74 Gearhart,N.L., Housman,H.J., Morgan,J.F., Norton,G.P., and Tsoupas,N., Phys. Rev. C **10**, 1739 (1974)

Go85 Gould,C.R. and Roberson,N.R., IEEE Trans. Nucl. Sci., NS-**32**, 1447 (1985)

Ha75 Haight,R.C., Proctor,I.D., Lutz,H.F., and Bartolini,W., Nucl. Phys. A **241**, 285 (1975)

Ha68 Harney, H.L., Nucl. Phys. A **119**, 591 (1968)

Ha69 Harney,H.L. and Weidenmuller,H.A., Nucl. Phys. A **139**, 241 (1969)

He73 Hemsky,J.W., Ling,S.C., and Wolfe,P.J., Phys. Rev. C **8**, 192 (1973)

Hu54 Huby,R., Proc. Phys. Soc. A **67**, 1103 (1954)

Ka75 Karadzhev,K.V., Mazurov,I.B., Man'ko,V.I., and Nersesyan,A.N., Sov. J. Nucl. Phys. **22**, 460 (1975)

Ka88 Karban,O., Potvin,L., and Turkiewicz,I.M., Nucl. Phys. A **480**, 125 (1988)

Kl72 Klucharev,A.P., Slabospitsky,R.P., Andreev,G.B., Borolev,V.I., Lopatko,I.D., and Lutsik,V.P., Ann. Phys. **71**, 438 (1972)

Ko77 Koyama,K., Nakanishi,N., Takeda,S., Yamada,S., Sakaguchi,H., Nakamura,M., Takeuchi,S., and Ohnuma,H., Phys. Soc. Japan **43**, 755 (1977)

La58 Lane,A.M. and Thomas,R.G., Rev. Mod. Phys. **30**, 324 (1958)

Le74 Leleux,P., Macq,P.C., Meulders,J.P., and Pirart,C., Z. Phys. **271**, 139 (1974)

Ma66 Marion,J.B., Rev. Mod. Phys. **38**, 660 (1966)

Mc84 McCulloch,R.A., Clarke,N.M., Griffits,R.J., Hanspal, J.S., Roman,S., and Barnwell,J.M., Nucl. Phys. A **431**, 344 (1984)

Me75 Meyer,M.A., Venter,I. and Reitman,D., Nucl. Phys. A **250**, 235 (1975)

Mo69 Moses,J.D. A High Resolution Study of Isobaric Analogue Resonances in $^{51}$Mn, $^{53}$Mn, and $^{55}$Mn, Ph.D. Dissertation, Duke University (1969)

Ne83 Nelson,R.O., Proton Resonance Spectroscopy in $^{28}$Si and $^{30}$P PhD. Dissertation, Duke University (1983)

Ne83a Nelson,R.O., Bilpuch,E.G., Westerfeldt,C.R., and Mitchell ,G.E., Phys. Rev. C **27**, 930 (1983)

Oo61 Van Oostrum,K.J., Hazewindus,N., Wapstra,A.H., Olness, J.W., and Parker,J.L., Nucl. Phys. **25**, 409 (1961)

Ou76 Outlaw,D.A., Mitchell,G.E., and Bilpuch,E.G., Nucl. Phys. A **269**, 99 (1976)

Pe75 Peterson,P.J. and Ristinen,R.A., Nucl. Phys. A **246**, 402 (1975)

Pe83 Peterson,R.J., Fields,C.A., Raymond,R.S., Thieke,J.R., and Ullman,J.L., Nucl. Phys. A **408**, 221 (1983)

Pe70 Pellegrini,F., Gentilin,F., Gauzzoni,P., Micheletti,S., and Pignanelli,M., Phys. Rev. C **2**, 1440 (1970)

Sc49 Schiff,L.I., Quantum Mechanics, McGraw-Hill Book Co., Inc., New York (1949) 1$^{st}$ edition

Th52 Thomas,R.G., Phys. Rev. **88**, 1109 (1952)

Tr86 Troutman,W., Bond,P.D., Hanson,O., Levine,M.J., Thorn, C.E., Videbaek,F., and

Christensen,P.R., Phys. Rev. C **34**, 1299 (1986)

Vo59 Vorona,J., Olness,J.W., Haeberli,W., and Lewis,H.W., Phys. Rev. **116**, 1563 (1959)

Vo62 Vogt,E., Rev. Mod. Phys. **34**, 723 (1962)

Wa86 Warthen,B.J., Nuclear Resonance Spectroscopy in $^{40}$Ca, Ph.D. Dissertation, Duke University (1986)

Wa80 Watson,W.A., A High Resolution Study of Proton Resonances in $^{57}$Co, Ph.D. Dissertation, Duke University (1980)

We87 Westerfeldt, C.R., Nelson,R.O., Bilpuch,E.G.,and Mitchell, G.E. The TUNL High Resolution Laboratory and Operating Procedures, Duke University (TUNL) (1987)

Wi47 Wigner, E.P. and Eisenbud, L., Phys. Rev. **72**, 29 (1947)

Wi73 Wilson,W.M., A High Resolution Study of Proton Resonances in $^{41}$Sc, $^{43}$Sc and $^{45}$Sc, Ph.D. Dissertation, Duke University (1973)

Za67 Zaidi,S.A.A. and Darmodjo,S., Phys. Rev. Lett. **19**, 1446 (1967)